Theoretical model of confined thermoviscous flows for artificial cytoplasmic streaming

Weida Liao [1], Elena Erben,[2] Moritz Kreysing,[2,3] and Eric Lauga [1,*]

[1]*Department of Applied Mathematics and Theoretical Physics, University of Cambridge, Wilberforce Road, Cambridge, CB3 0WA, United Kingdom*
[2]*Max Planck Institute of Molecular Cell Biology and Genetics, Pfotenhauerstraße 108, 01307 Dresden, Germany*
[3]*Institute of Biological and Chemical Systems, Karlsruhe Institute of Technology, Hermann-von-Helmholtz-Platz 1, 76344 Eggenstein-Leopoldshafen, Germany*

Recent experiments in cell biology have probed the impact of artificially induced intracellular flows in the spatiotemporal organization of cells and organisms. In these experiments, mild dynamical heating (a few kelvins) via focused infrared light from a laser leads to long-range, thermoviscous flows of the cytoplasm inside a cell. To extend future use of this method in cell biology, popularized as focused-light-induced cytoplasmic streaming (FLUCS), new quantitative models are needed to link the external light forcing to the produced flows and transport. Here, we present a fully analytical, theoretical model describing the fluid flow induced by the dynamical laser stimulus at all length scales (both near the scan path of the laser beam and in the far field) in two-dimensional confinement. We model the effect of the focused light as a small, local temperature change in the fluid, which causes a small change in both the density and the viscosity of the fluid locally. In turn, this results in a locally compressible fluid flow. We analytically solve for the instantaneous flow field induced by the translation of a heat spot of arbitrary time-dependent amplitude along a scan path of arbitrary length. We show that the leading-order instantaneous flow field results from the thermal expansion of the fluid and is independent of the thermal viscosity coefficient. This leading-order velocity field is proportional to the thermal expansion coefficient and the magnitude of the temperature perturbation, with far-field behavior typically dominated by a source or sink flow and proportional to the rate of change of the heat-spot amplitude. In contrast, and in agreement with experimental measurements, the net displacement of a material point due to a full scan of the heat spot is quadratic in the heat-spot amplitude, as it results from the interplay of thermal expansion and thermal viscosity changes. The corresponding average velocity of material points over a scan is a hydrodynamic source dipole in the far field, with direction dependent on the relative importance of thermal expansion and thermal viscosity changes. Our quantitative findings show excellent agreement with recent experimental results and will enable the design of new controlled experiments to establish the physiological role of physical transport processes inside cells.

*e.lauga@damtp.cam.ac.uk

I. INTRODUCTION

Throughout nature, fluid flows are responsible for transport in fundamental processes that sustain life on a wide range of length scales [1]. At the macroscopic scale, ocean circulation [2,3] and coastal flows [4,5] play key roles in determining the climate and shaping ecosystems, while interaction of the wind with plants disperses seeds over long distances and enhances gaseous exchange for photosynthesis [6]. In the human body, both respiratory [7] and blood flows [2,8,9] transport oxygen through networks of tubes. At the length scales of micrometers lies the viscous world of cells, from the cilia-driven flows that determine the left–right asymmetry of developing embryos [10,11] to the flows inside individual cells [12].

A notable example of intracellular fluid flow is known as cytoplasmic streaming. First discovered in the eighteenth century [13], cytoplasmic streaming is the bulk movement or circulation of the water-based viscous fluid, called the cytoplasm, inside a cell. A fluid flow of this type is found in a wide variety of organisms, including plants, algae, animals, and fungi [14,15]. Cytoplasmic streaming has been shown to exhibit a wide range of topologies, including the fountainlike flow inside the pollen tube of a flower (*Lilium longiflorum*) [16], highly symmetrical streaming inside a green algal cell (*Chara corallina*) [17], and swirls and eddies in the oocyte of the fruit fly (*Drosophila*) [18].

Cytoplasmic streaming is driven actively: molecular motors move large cargos, such as vesicles and organelles, along polymeric filaments inside the cell, thereby entraining fluid. The resulting flow of the whole fluid inside the cell induces transport of various substances in the fluid, including proteins, nutrients and organelles, which is important for fundamental processes such as metabolism and cell division [19,20]. This active, advective transport can be especially important in larger cells, with size on the order of a hundred micrometers [21]. Indeed, diffusive transport by itself can be too slow on these larger length scales [19]; this is further hindered by the crowded nature of the cytoplasm, with macromolecules making up 20–30% of the volume [22]. Advective transport due to cytoplasmic streaming has therefore been argued to significantly impact cellular processes and the spatiotemporal organization of cells [21,23].

A number of theoretical and experimental studies have explored the precise role that cytoplasmic streaming plays in these processes [12]. For example, the green alga *Chara corallina* has long, cylindrical cells. Inside these cells, helical flows, which are driven from the cell boundary by the motion of myosin motors along actin filament tracks, have been measured experimentally [17]. Probing the consequences of this rotational streaming theoretically, hydrodynamic models have suggested that the helical flow enhances mixing [24] and mass flux across the cell boundary [25]. For animal cells, numerical simulations have demonstrated that cytoplasmic flows could result in robust positioning of organelles. In these simulations, the flows in the *Caenorhabditis elegans* embryo were driven by motors moving along microtubules [26], whereas in mouse oocytes the cytoplasmic flows were driven by the motion of actin filaments near the boundary [27]. Despite the contrasting molecular driving mechanisms, both led to a fountainlike flow pattern that could transport organelles to their required positions [12].

From an experimental standpoint, there are two significant, closely related challenges in establishing the biological function of intracellular flows. The first is to create flows inside cells reminiscent of naturally occurring cytoplasmic streaming but driven artificially, without risking unwanted side effects that may be associated with genetic or chemical perturbations. The second, closely linked challenge lies in perturbing existing flows inside cells, so that the consequences for cellular processes may be observed. Such a perturbative technique is arguably necessary to advance understanding of the physiology of intracellular flows, beyond correlation and towards causal relationships [28].

To investigate in detail the causes and consequences of intracellular flows, the authors of Ref. [28] recently demonstrated the use of thermoviscous flows [29,30] inside cells and developing embryos to generate and perturb cytoplasmic flows and transport, popularizing this approach in cell biology and terming it focused-light-induced cytoplasmic streaming (FLUCS). Using focused infrared light

from a laser, localized in a small region of the cell, a thermoviscous flow is induced globally inside the cell, due to heating of the fluid. The laser beam produces a heat spot in the fluid and translates along a short scan path repeatedly, at a frequency of around 2 kHz; the repeated scanning then results in net transport of substances in the fluid, which, near the scan path, is typically in the opposite direction to the laser motion. To produce net transport at physiological speeds, the temperature changes required are only a few kelvins, avoiding damage to the cell. Furthermore, this net transport, while strongest near the scan path, extends throughout the cell, sharing the long-ranged nature of cytoplasmic streaming. This noninvasive technique enables the study of flows and transport inside cells in cellular organization and processes.

Focusing on cell biology applications, the same group used FLUCS to show how fundamental processes in cell development are driven by intracellular flows [28]. For example, at the onset of development, the *C. elegans* zygote becomes polarized, before asymmetric cell division into two differently sized daughter cells. The concentration of a particular protein (PAR2) determines which end of the zygote becomes the smaller germ cell and which becomes the larger somatic cell, thereby defining the body axis. Flows of physiological magnitude and duration, created using FLUCS, were shown to be sufficient to localise these proteins [28]. This demonstrates the biological significance of physical transport processes inside cells, as well as the potential of FLUCS for new experiments to reveal the precise role of intracellular fluid flows [31].

The FLUCS technique has also enabled experimental perturbations to developmental processes [28,32,33]. Guided by numerical simulations, FLUCS was used to redistribute PAR2 within the *C. elegans* zygote, remarkably leading to the inversion of its body axis [28]. The authors of Ref. [32] controlled oocyte growth in *C. elegans* by artificially changing the volume of cells via FLUCS. A combination of FLUCS, genetics, and pharmacological intervention revealed the material properties of centrosomes in *C. elegans* embryos during development and their molecular basis [33]. Beyond biology, thermoviscous flow and transport have been used together with closed-loop feedback control to achieve high-precision positioning of micrometer-sized particles [34] and high-sensitivity force measurements [35].

From a hydrodynamic perspective, the flows and net transport generated in the FLUCS experiments can be explained in terms of the combined thermal expansion and thermal viscosity changes in the fluid caused by the laser, as first demonstrated in earlier works [29,30,36]. These studies dealt with Newtonian viscous fluid characterized by temperature-dependent density and viscosity. This may serve as a simplified model for cytoplasm [28], the complex rheology of which has been the subject of many studies [19,37,38]. For a traveling temperature wave, it was shown both mathematically and experimentally that thermal viscosity changes combined with flow driven by thermal expansion induced net transport of tracers along the scan path in a thin-film geometry [29]. A subsequent study instead examined localized heating by a laser, producing a heat spot that translates along a scan path repeatedly [30]; this is the relevant technique used in later biological (FLUCS) experiments inside cells [28]. With a combination of theory, numerical simulation, and experiments, this demonstrated that the localized heating also results in net transport of tracers, in a thin film of viscous fluid between two parallel plates [30]. The theory presented in Ref. [30] focused on net transport of tracers on and parallel to the scan path itself, for a heat spot of constant amplitude translating along an infinitely long scan path.

In the experiments of Refs. [28,30,34], both the instantaneous thermoviscous flow and the net transport induced by the laser heating are not localized to the scan path but instead extend throughout space, as is the case for natural cytoplasmic streaming. A recent experimental study quantified how the average speed of tracers varies spatially, finding an inverse square law far from the scan path, in controlled microfluidic experiments on viscous fluid (glycerol-water solution) between two parallel plates [34]. For the purposes of modeling, this setup also has the advantage of separating the physical consequences of FLUCS from the biological effects. Furthermore, in the experiments of Refs. [28,30,34], the scan path has finite length and the amplitude of the heat spot varies with time. Numerical simulations, for FLUCS inside an ellipsoid representing a cell [28], suggest that
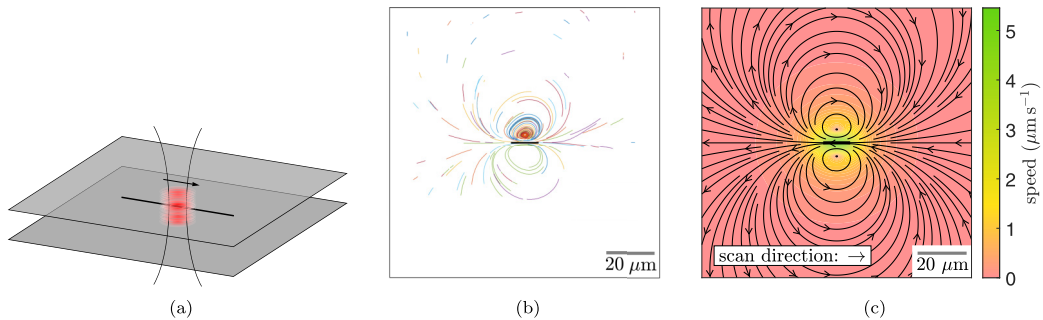
FIG. 1. (a) Sketch of setup; a laser focused on a fluid confined between two parallel plates creates a heat spot (red), which translates along a scan path and induces fluid flow. (b) Experimentally found trajectories of tracer beads in the fluid, due to repeated scanning of the heat spot, viewed from above, adapted with permission from Fig. 2(d) of Ref. [34] (The Optical Society). (c) Theoretical time-averaged trajectories of tracers in the fluid as derived in this study (colours indicate the average speed of tracers), with parameters corresponding to experiments in panel (b).

these two factors are crucial for understanding how the net transport of tracers in the fluid varies spatially in practical applications of FLUCS.

In our work, summarized in Fig. 1 and directly motivated by the controlled experiments in Ref. [34], we present an analytical, theoretical model of the flow driven in viscous fluid confined between two parallel plates by the focused light, with a scan path of arbitrary length and a fully general, time-dependent heat-spot amplitude. We first solve analytically for the instantaneous fluid flow field induced by the heat spot during a scan period, valid in the entire spatial domain (i.e., from the near to the far field), before analyzing the trajectories of tracers in the fluid during one scan period and the net displacement of tracers due to a full scan of the heat spot. The theory quantitatively and rigorously predicts how this net transport of tracers, induced by the repeated scanning, varies throughout space, in agreement with data from recent microfluidic experiments [34]. Our modeling elucidates the fundamental physics of intracellular transport by FLUCS. Our results will be useful for designing new FLUCS experiments to establish the physiological role of physical transport processes inside cells. Our analytical descriptions will also enable the generation of more precise flow fields at even lower temperature impact on living cells, as well as the training of mathematical models (e.g., machine-learning) to use flow fields for enhanced micromanipulations.

This article is organized as follows. In Sec. II, we solve analytically for the instantaneous flow field induced by a translating heat spot between two parallel plates, in the limit of small temperature change in the fluid. We demonstrate mathematically that thermal expansion drives the flow. The instantaneous flow at leading order is linear in the heat-spot amplitude and is purely due to thermal expansion, independent of thermal viscosity changes, in agreement with earlier work [29,36]. Our analytical solution for the instantaneous fluid velocity field shows that for a finite scan path (as in experiments), the time-dependence of the heat-spot amplitude is key, with the rate of change of the heat-spot amplitude setting the strength of the far-field source flow. In the far field, this source flow typically dominates over the source dipole associated with the translation of the heat spot. We next solve for higher-order contributions to the instantaneous flow field, quadratic in the heat-spot amplitude and including the first effect of thermal viscosity changes. These higher-order terms are crucial for quantifying the net transport of tracers over many scan periods resulting from the instantaneous flow; the higher-order terms arise from the amplification of the leading-order flow by the heat spot and, in the experiments of Ref. [34], are predominantly due to thermal viscosity changes. Building on the analytical leading-order instantaneous flow field, in Sec. III, we next solve analytically for the leading-order trajectory of an individual material point or tracer during one scan of the heat spot along a scan path. We then demonstrate for a general heat spot that the net displacement of
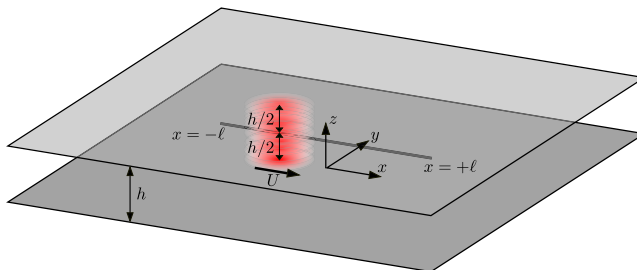
FIG. 2. Setup of our theoretical model. A heat spot of characteristic radius a translates at speed U in the x direction, along a scan path along $y = 0$ from $x = -\ell$ to $x = +\ell$, causing inertialess fluid flow between the two no-slip boundaries at $z = 0$ and $z = h$.

material points after a full scan period occurs at higher order. Motivated by this, we show in Sec. IV that the leading-order net displacement of a material point due to a scan is quadratic in the heat-spot amplitude, in quantitative agreement with experiments [28,30], and is due to the combined impact of temperature on both the density and the viscosity of the fluid, in agreement with earlier theory [29]. We then visualize the trajectories of material points due to repeated scanning of the heat spot along a finite scan path. We characterize the average velocity of tracers (average Lagrangian velocity) over a scan period, finding that this is a hydrodynamic source dipole in the far field, in contrast with the slower-decaying far-field instantaneous fluid flow. Finally, in Sec. V, we quantitatively compare the results from our theoretical model with the microfluidic experiments in Ref. [34], which measured the trajectories and average speed of tracers due to repeated scanning of a heat spot. We conclude with a discussion of the predictions and limitations of our modeling approach, and in Sec. VI, we summarize our work and propose possible further applications of our model.

II. THEORETICAL MODEL FOR INSTANTANEOUS FLOW

A. Setup

In this first section, we introduce our theoretical model for the microfluidic experiments conducted in Ref. [34] as a simplified, controlled version of experiments in biological cells [28]. The setup is illustrated in Fig. 2 and a simplified view from above is given in Fig. 3, including a sketch
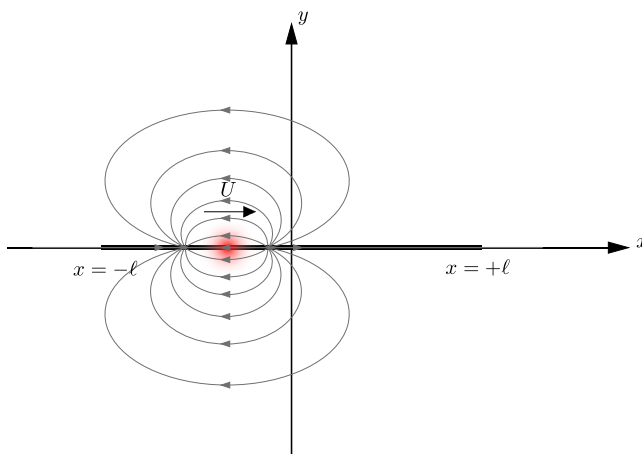

FIG. 3. View from above of translating heat spot in Fig. 2, with schematic instantaneous flow streamlines.

of possible instantaneous flow streamlines. We consider fluid confined between parallel no-slip surfaces at $z = 0$ and $z = h$ (Hele-Shaw geometry). A heat spot of characteristic radius a translates at constant speed U along a scan path. The scan path is a line segment from $x = -\ell$ to $x = +\ell$ along $y = 0$. At time t, the center of the heat spot is thus at $(x = Ut, y = 0, z = h/2)$, for $-\ell/U \leqslant t \leqslant \ell/U$ (i.e., during one scan). Initially, we focus on the fluid flow induced instantaneously by the heat spot. We will examine in Sec. III the motion of tracers or material points, with any initial position, due to the instantaneous flow during one scan period and then in Sec. IV the net displacement of tracers resulting from a full scan of the heat spot. This will allow us to understand the trajectories and average velocity of tracers due to repeated scanning as in experiments (Sec. V), i.e., where the heat spot travels from $x = -\ell$ to $x = +\ell$, then disappears and immediately reappears at $x = -\ell$, and repeats the process [30,34]; the distinction between the instantaneous velocity field and the time-averaged velocity of tracers is crucial for quantitatively reproducing experimental results.

We may write the temperature field $T(x, y, z, t)$ of the fluid as

$$T(x, y, z, t) = T_0 + \Delta T(x, y, z, t), \tag{1}$$

where T_0 is a constant reference temperature and $\Delta T(x, y, z, t)$ is the temperature change of the fluid due to the heat spot. Below, we will prescribe this temperature field and discuss the conditions under which this is a good approximation. We model the effect of the temperature change on the fluid as follows. Through thermal expansion (i.e., volume changes), an increase in the temperature of the fluid locally decreases the density ρ of the fluid (true for most fluids). Since biological applications require small temperature changes, we may model this with a standard linear relationship

$$\rho = \rho_0(1 - \alpha \Delta T), \tag{2}$$

where ρ_0 is the density of the fluid at the reference temperature T_0 and we introduce the thermal expansion coefficient α. A small, local increase in temperature also locally decreases the shear viscosity (i.e., dynamic viscosity) η of the fluid, modeled as

$$\eta = \eta_0(1 - \beta \Delta T), \tag{3}$$

where η_0 is the shear viscosity of the fluid at the reference temperature T_0 and we introduce the thermal viscosity coefficient β. For typical fluids, the coefficients α and β are both usually positive [39]. In this paper, we only consider small temperature changes, such that the relative density and viscosity changes are small, i.e., $|\alpha \Delta T|, |\beta \Delta T| \ll 1$. This is the relevant limit both for the microfluidic experiments of Ref. [34] (Sec. V) and for focused-light-induced cytoplasmic streaming in biological experiments, to avoid unwanted side effects of temperature changes inside cells.

Due to these effects, the heat spot induces a fluid flow, which we will solve for. First, mass conservation is given by

$$\frac{\partial \rho}{\partial t} + \nabla \cdot (\rho \mathbf{u}) = 0, \tag{4}$$

where $\mathbf{u} \equiv (u, v, w)$ is the velocity field.

Next, the Cauchy momentum equation is given by

$$\rho \frac{D\mathbf{u}}{Dt} = \nabla \cdot \mathbf{\Pi} + \rho \mathbf{g}, \tag{5}$$

where $\mathbf{g}$ is the gravitational acceleration and the stress tensor $\mathbf{\Pi}$, under the Newtonian hypothesis, is given by

$$\mathbf{\Pi} = -p\mathbf{1} + \kappa(\nabla \cdot \mathbf{u})\mathbf{1} + 2\eta\left\{\frac{1}{2}[\nabla \mathbf{u} + (\nabla \mathbf{u})^{\mathrm{T}}] - \frac{1}{3}\mathbf{1}(\nabla \cdot \mathbf{u})\right\}. \tag{6}$$

Here, p is the pressure field, $\mathbf{1}$ is the identity tensor, and κ is the bulk viscosity. While the shear viscosity η relates the stress to the linear deformation rate, the bulk viscosity κ relates the stress to the volumetric deformation rate [40] and can be important for compressible flows. We also note that the bulk viscosity κ, like the shear viscosity η, is in general a function of temperature [40,41].

Now, to make analytical progress, we use the lubrication limit, as in earlier work [29,30]. That is, we assume that the vertical separation of the plates h is much smaller than the characteristic length scale over which the flow varies in the horizontal directions x and y, given by the characteristic heat-spot diameter $2a$. It follows that the timescale for diffusion of heat in the z direction is much smaller than that in the x and y directions. The laser beam intensity in experiments also decays much faster in the horizontal directions than it varies in the z direction. Thus, as a simplifying assumption, we take the temperature of the fluid to be independent of z, so that we model the temperature change caused by the laser as $\Delta T = \Delta T(x, y, t)$.

With these two assumptions, $h \ll 2a$ and $\frac{\partial \Delta T}{\partial z} = 0$, we may use a scaling argument similar to that for the classical, incompressible case [42] to simplify the momentum equation. We include the detailed derivation in Appendix A. We find that in the lubrication limit, the momentum equations become

$$-\frac{\partial p}{\partial x} + \eta \frac{\partial^2 u}{\partial z^2} = 0, \tag{7}$$

$$-\frac{\partial p}{\partial y} + \eta \frac{\partial^2 v}{\partial z^2} = 0, \tag{8}$$

$$\frac{\partial p}{\partial z} = 0, \tag{9}$$

the same as the standard momentum equations for incompressible lubrication flow. We observe that the bulk viscosity no longer appears in these equations; from now on, for brevity, we thus refer to the shear viscosity η simply as the viscosity.

A few comments on the assumptions made here are in order. First, we note that in Sec. V D we return to the validity of the lubrication limit in terms of the length scales in the experiments of Ref. [34] (which quantified the spatial variation of average tracer speed); in Sec. V C, we also verify *a posteriori* that the inertial terms may indeed be neglected via a scaling argument. Second, we remark that we have not included gravity in the equations above. The primary focus of our article is the flow driven by thermal expansion. With gravity, the density differences result in a horizontal gradient in hydrostatic pressure, typically driving gravity currents [43]. However, in Sec. V C, we demonstrate with a scaling argument that the ratio of the resulting gravity current to the thermal-expansion-driven flow is small for the experimental parameter values [36].

To close the system of equations, we have the following boundary conditions. The velocity field is assumed to not be singular at the center of the heat spot. At the rigid, stationary parallel plates $z = 0$ and $z = h$, the velocity field obeys the no-slip boundary condition. The velocity is also taken to decay in the far field (unbounded fluid assumed), for a temperature change that decays in the far field.

In this article, we derive various equations and results that hold for a general temperature profile $\Delta T(x, y, t)$. To illustrate these and to provide an explicit analytical solution for the flow, we will also impose in some of our results a Gaussian temperature profile for the heat spot given by

$$\Delta T(x, y, t) = \Delta T_0 A(t) \exp\{-[(x - Ut)^2 + y^2]/2a^2\}, \tag{10}$$

where ΔT_0 is the characteristic temperature change (a constant chosen to be positive) and $A(t)$ is the dimensionless amplitude of the heat spot, a function of time and kept arbitrary in our theoretical work. The temperature profile in Eq. (10) applies during one scan of the heat spot along the scan path. For a heat spot, we assume that the amplitude $A(t)$ is positive, $A(t) \geqslant 0$.

The time-dependence of the heat-spot amplitude is a key ingredient in our theory, generalizing previous theoretical modeling [30] that had a constant heat-spot amplitude and an infinitely long scan path. In experiments, the scan path is finite. This is captured by the amplitude function, which must therefore be time-dependent: by definition, the amplitude is zero at each end of the scan path, i.e., we always assume that $A(\pm\ell/U) = 0$. Furthermore, numerical work [28] for a different

geometry (fluid inside an ellipsoid) found that time-variation of the heat-spot amplitude is necessary to reproduce experimentally observed net transport.

The Gaussian spatial dependence of the temperature profile ΔT in Eq. (10) is motivated by measurements of the temperature field in experiments [30], which showed that this is a good approximation provided that the translation of the laser beam is slow compared with the thermal equilibration of the fluid. In Sec. V D, we discuss the validity of this assumption for the experiments in Ref. [34], using a scaling argument for the advection-diffusion equation for heat. For experiments in cell biology, a noninvasive technique that does not damage the cells is desirable. The highly localized nature of the temperature perturbation in Eq. (10), with small characteristic size compared with the cell, is therefore advantageous. We will show rigorously that this exponentially decaying heating results in both strong net transport near the scan path and slowly decaying flows in the far field, with algebraic instead of exponential scaling with distance.

We emphasize that while we have introduced here a Gaussian temperature field, many of the results in this article hold for any temperature profile $\Delta T(x, y, t)$. This generality is important because in experiments the heat spot can lose the circular symmetry assumed in Eq. (10) if its speed of translation is too high; it may become elongated because of the thermal equilibration time of cooling the fluid [28,30].

B. Two-dimensional flow equations

With the setup detailed in Sec. II A, we now reduce the problem to two dimensions, following standard lubrication theory arguments as in Ref. [29]. We may directly integrate the lubrication momentum equations, Eqs. (7)–(9), and use the no-slip boundary conditions. The parabolic profile for the horizontal velocity field $\mathbf{u}_H \equiv (u, v) \equiv \mathbf{u}_H(x, y, z, t)$ is then given by

$$\mathbf{u}_H = -\frac{\nabla_H p}{2\eta} z(h - z), \tag{11}$$

where the horizontal gradient is $\nabla_H \equiv (\partial/\partial x, \partial/\partial y)$.

We define the z average as

$$\overline{(.)} = \frac{1}{h} \int_0^h (.) \, dz, \tag{12}$$

so that the two-dimensional (2D), z-averaged, horizontal velocity field $\overline{\mathbf{u}}_H(x, y, t)$ is given by

$$\overline{\mathbf{u}}_H = -\frac{h^2}{12\eta} \nabla_H p. \tag{13}$$

We note for later comparison with experimental data in Sec. V that this differs from the velocity in the midplane, $z = h/2$, by a factor of $2/3$; in other words, we have

$$\mathbf{u}_H|_{z=h/2} = -\frac{h^2}{8\eta} \nabla_H p = \frac{3}{2}\overline{\mathbf{u}}_H. \tag{14}$$

We also compute the z average of the mass conservation equation, Eq. (4). Combining this with the no-penetration boundary conditions on the parallel plates $z = 0$ and $z = h$, we find

$$\frac{\partial \rho}{\partial t} + \nabla_H \cdot (\rho \overline{\mathbf{u}}_H) = 0. \tag{15}$$

We note that since we allow arbitrary time-variation of the heat-spot amplitude in our theory, the solution for the flow is not in general steady in the frame of the translating heat spot. Hence, throughout this article, we work in the laboratory frame, in which the scan path is fixed and the fluid is at rest at infinity.

To simplify notation, from now on, we will only discuss two spatial dimensions (x, y) and the corresponding two-dimensional, z-averaged, horizontal velocity field $\overline{\mathbf{u}}_H$. Thus, in what follows, we

drop the bar and subscript H from this velocity field and call it **u**. Similarly, we now write ∇ instead of ∇_H for the horizontal gradient.

C. Dimensionless problem statement

We now nondimensionalize the key equations of the problem, Eqs. (2), (3), (10), (13), and (15). We use the following characteristic scales: the heat-spot speed U for velocity, the characteristic heat-spot radius a for length, a/U for time, the viscous lubrication stress scale $12\eta_0 aU/h^2$ for pressure (including the factor of 12 for mathematical convenience), the characteristic temperature change ΔT_0 for temperature, and the reference values ρ_0 for density and η_0 for viscosity. For simplicity, we keep the same variables (**u**, x, y, ℓ, ∇, t, p, α, β, ΔT, ρ, and η) to denote their dimensionless equivalents.

Then, to summarize the dimensionless problem, the two-dimensional velocity field is determined by the pressure as

$$\mathbf{u} = -\frac{1}{\eta}\nabla p, \tag{16}$$

and the mass conservation equation is given by

$$\frac{\partial \rho}{\partial t} + \nabla \cdot (\rho \mathbf{u}) = 0. \tag{17}$$

We will derive results for a general prescribed temperature change $\Delta T(x, y, t)$ and also solve these equations explicitly with a Gaussian temperature profile (with arbitrary time-dependent amplitude) given by

$$\Delta T(x, y, t) = A(t)\exp\{-[(x - t)^2 + y^2]/2\}, \tag{18}$$

during one scan. The temperature change determines the density ρ and viscosity η of the fluid via the equations

$$\rho = 1 - \alpha\Delta T, \tag{19}$$

$$\eta = 1 - \beta\Delta T, \tag{20}$$

respectively. The boundary conditions for the two-dimensional problem are that the velocity field is assumed to not be singular at the center of the heat spot and the fluid velocity is taken to decay at infinity.

Since the pressure field determines the velocity field, we may also derive a single equation for the pressure p by substituting Eq. (16) into Eq. (17) to give

$$\frac{\partial \rho}{\partial t} - \nabla \cdot \left(\frac{\rho}{\eta}\nabla p\right) = 0. \tag{21}$$

Using Eqs. (19) and (20) to write this in terms of the general temperature field ΔT gives

$$\nabla \cdot \left(\frac{1 - \alpha\Delta T}{1 - \beta\Delta T}\nabla p\right) = -\alpha\frac{\partial\Delta T}{\partial t}. \tag{22}$$

The pressure boundary conditions are inherited from the velocity boundary conditions, so that the pressure gradient ∇p is assumed not to be singular at the center of the heat spot and the pressure gradient tends to zero at infinity. (Note that the pressure itself does not necessarily decay at infinity; for example, the pressure associated with a source flow grows logarithmically at infinity.)

D. Perturbation expansion

To make analytical progress in solving Eq. (22), we use a similar approach to that in Ref. [29]. We consider the limit of small thermal expansion coefficient ($\alpha \ll 1$) and small thermal viscosity

coefficient ($\beta \ll 1$), where we recall that these are dimensionless parameters, small because the characteristic temperature perturbation ΔT_0 in experiments is sufficiently small. We pose a perturbation expansion in both of these parameters for the pressure p, given by

$$p = \sum_{(m,n)=(0,0)}^{(\infty,\infty)} \alpha^m \beta^n p_{m,n}$$

$$\equiv p_{0,0} + \alpha p_{1,0} + \beta p_{0,1} + \alpha^2 p_{2,0} + \alpha\beta p_{1,1} + \beta^2 p_{0,2} + \text{cubic and higher-order terms}, \quad (23)$$

as $\alpha, \beta \to 0$. In other words, the pressure at order $\alpha^m \beta^n$ is $p_{m,n}$. We solve below for the pressure order by order. This systematic approach allows us to understand the roles of thermal expansion and thermal viscosity changes in the flows induced.

We may then obtain the corresponding fluid velocity field by expanding Eq. (16) for small α and β and collecting the terms as

$$\mathbf{u} = -\left[\sum_{k=0}^{\infty} (\beta\Delta T)^k\right] \sum_{(m,n)=(0,0)}^{(\infty,\infty)} \alpha^m \beta^n \nabla p_{m,n}$$

$$\equiv \sum_{(m,n)=(0,0)}^{(\infty,\infty)} \alpha^m \beta^n \mathbf{u}_{m,n}$$

$$\equiv \mathbf{u}_{0,0} + \alpha\mathbf{u}_{1,0} + \beta\mathbf{u}_{0,1} + \alpha^2\mathbf{u}_{2,0} + \alpha\beta\mathbf{u}_{1,1} + \beta^2\mathbf{u}_{0,2} + \text{cubic and higher-order terms}. \quad (24)$$

We see that the velocity field $\mathbf{u}_{m,n}$ at order $\alpha^m \beta^n$ depends explicitly on the pressure fields $p_{m,n'}$ with $0 \leqslant n' \leqslant n$, i.e., at lower or equal order in β.

We now expand Eq. (22) for the pressure p, using Eq. (23), to find

$$\nabla \cdot \left\{ (1 - \alpha\Delta T)\left[\sum_{k=0}^{\infty} (\beta\Delta T)^k\right] \sum_{(m,n)=(0,0)}^{(\infty,\infty)} \alpha^m \beta^n \nabla p_{m,n} \right\} = -\alpha \frac{\partial \Delta T}{\partial t}. \quad (25)$$

We emphasize that this equation for pressure holds for any temperature profile ΔT and note that the forcing for this equation occurs at order α. We therefore anticipate that both the leading-order pressure and the leading-order flow it drives occur also at order α.

We finally observe that for any temperature profile ΔT, the velocity field $\mathbf{u}_{m,0}$ at order α^m is a potential flow (i.e., irrotational) for all m, given by

$$\mathbf{u}_{m,0} = -\nabla p_{m,0}. \quad (26)$$

In other words, as remarked in Ref. [29], if the viscosity is constant, then the pressure acts as a velocity potential.

E. Solution at order β^n

We now solve Eq. (25) order by order. We note that since this is a series of Poisson equations for pressure with Neumann boundary conditions, the solution for the flow at each order is unique. First we consider order β^n in Eq. (25) for all $n \geqslant 0$, i.e., orders 1, β, β^2, and so on. We can show by induction that the pressure $p_{0,n}$ at all these orders is zero, so that the corresponding velocity field $\mathbf{u}_{0,n}$ at each of these orders is also zero, for any prescribed temperature profile ΔT that decays at infinity. We include the proof in Appendix B.

Hence, the leading-order instantaneous flow occurs at order α and is purely due to local volume changes of the fluid upon heating. Furthermore, there is no flow at order β or order β^2. Therefore, in our perturbation expansion, the first effect of thermal viscosity changes occurs at order $\alpha\beta$.

In the microfluidic experiments of Ref. [34] that we discuss in Sec. V, the thermal viscosity coefficient β is much larger than the thermal expansion coefficient α for the fluid used

(glycerol-water solution), so that the flow at order $\alpha\beta$ is larger than that at order α^2. However, for a general fluid, the coefficients α and β may be closer in magnitude [39], so that the flow at order α^2 could potentially be as important as the flow at order $\alpha\beta$. Therefore, in this section, we include the solution for the instantaneous flow up to quadratic order. Both quadratic terms (order $\alpha\beta$ and order α^2) are crucial for understanding the trajectories of material points over many scans, as we will find that the leading-order instantaneous flow (order α) in fact gives rise to zero net displacement of material points after one full scan of the heat spot, at order α.

In summary, the perturbation expansion for the velocity field $\mathbf{u}$ simplifies to

$$\mathbf{u} = \alpha\mathbf{u}_{1,0} + \alpha^2\mathbf{u}_{2,0} + \alpha\beta\mathbf{u}_{1,1} + \text{cubic and higher-order terms.} \tag{27}$$

Since there is no flow at order β^n, all terms in this updated perturbation expansion include the thermal expansion coefficient α. Physically, this means that the instantaneous flow is driven by thermal expansion. Thermal expansion can produce flow without thermal viscosity changes, but thermal viscosity changes can only lead to flow through interaction with thermal expansion.

F. Solution at order α

We now solve for the leading-order instantaneous flow induced by the translating heat spot with arbitrary time-dependent amplitude. This occurs at order α, matching the forcing of the mass conservation equation by the temperature changes; in other words, this flow is associated purely with thermal expansion.

We begin by deriving the result that for a heat spot of arbitrary shape, the instantaneous fluid velocity field at order α is the time-derivative of a function proportional to the amplitude $A(t)$ of the heat spot. This is important for understanding the net displacement of material points after a full scan period in Sec. III. We next discuss the physical mechanism for the flow induced by a general heat spot. Then we specialize to a Gaussian heat spot and obtain an explicit analytical formula for the leading-order flow field $\mathbf{u}_{1,0}$ at order α, given by Eqs. (46)–(48). To visualize this key result, we plot the streamlines of the two separate contributions to the flow in Figs. 6 and 8; we then illustrate the full velocity field during one scan in Figs. 10 and 11.

1. General heat spot

At order α, the equation for the pressure [Eq. (25)] reads

$$\nabla^2 p_{1,0} = -\frac{\partial \Delta T}{\partial t}, \tag{28}$$

and holds for any temperature profile ΔT; this is the fully linearized, leading-order problem. We observe that the forcing in Eq. (28) is a time-derivative. If we find a function $F(x, y, t)$ such that

$$\nabla^2 F = -\Delta T, \tag{29}$$

then $p_{1,0} = \partial F/\partial t$ is a solution of Eq. (28).

We now assume that the temperature profile $\Delta T(x, y, t)$ during a scan is set by some arbitrary shape function $\Theta(x - t, y)$, steady in the frame moving with the heat spot, multiplied by the (arbitrary) time-dependent amplitude function $A(t)$, i.e.,

$$\Delta T(x, y, t) = A(t)\Theta(x - t, y). \tag{30}$$

The amplitude function $A(t)$ is taken to be positive if ΔT is a heat spot and negative if ΔT is a cool spot. The shape function $\Theta(x - t, y)$ has the interpretation of a heat spot with constant amplitude that translates at unit speed in the positive x direction. For example, the Gaussian heat spot in Eq. (18) corresponds to shape function $\Theta(x, y) = \exp[-(x^2 + y^2)/2]$; in general, the shape function need not have circular symmetry.

To solve Eq. (29), with the general heat spot in Eq. (30), we pose the ansatz

$$F(x, y, t) = A(t)p_{1,0}^{(S)}(x - t, y), \tag{31}$$

where we will see later that $p_{1,0}^{(S)}(x-t,y)$ is the pressure field associated with the time-variation of the amplitude of the heat spot, as the heat spot switches on or off gradually (S stands for "switch" in the superscript). The pressure field $p_{1,0}^{(S)}(x-t,y)$ satisfies the Poisson equation

$$\nabla^2 p_{1,0}^{(S)}(x-t,y) = -\Theta(x-t,y). \tag{32}$$

For any given shape function Θ, we can solve Eq. (32) for $p_{1,0}^{(S)}(x-t,y)$ (nonsingular at the center of the heat spot and with decaying gradient at infinity). We then deduce that the full pressure field $p_{1,0}$ at order α is given by

$$p_{1,0}(x,y,t) = \frac{\partial}{\partial t}\big[A(t)p_{1,0}^{(S)}(x-t,y)\big] \equiv A'(t)p_{1,0}^{(S)}(x-t,y) + A(t)p_{1,0}^{(T)}(x-t,y), \tag{33}$$

where prime $(')$ denotes differentiation with respect to the argument (here, time t) and we define the pressure field $p_{1,0}^{(T)}(x-t,y)$ as

$$p_{1,0}^{(T)}(x-t,y) \equiv \frac{\partial}{\partial t}p_{1,0}^{(S)}(x-t,y). \tag{34}$$

We will see later that the pressure field $p_{1,0}^{(T)}(x-t,y)$ is associated with translation of the heat spot (T stands for "translate" in the superscript).

In Eq. (33), we have decomposed the pressure field at order α into two contributions. The corresponding velocity field is given by

$$\mathbf{u}_{1,0}(x,y,t) = -\frac{\partial}{\partial t}\boldsymbol{\nabla}\big[A(t)p_{1,0}^{(S)}(x-t,y)\big]$$

$$= \frac{\partial}{\partial t}\big[A(t)\mathbf{u}_{1,0}^{(S)}(x-t,y)\big] \equiv A'(t)\mathbf{u}_{1,0}^{(S)}(x-t,y) + A(t)\mathbf{u}_{1,0}^{(T)}(x-t,y), \tag{35}$$

where the two separate velocity fields $\mathbf{u}_{1,0}^{(S)}$ (associated with the switching-on of the heat spot) and $\mathbf{u}_{1,0}^{(T)}$ (associated with the translation of the heat spot) are given by

$$\mathbf{u}_{1,0}^{(S)} = -\boldsymbol{\nabla}p_{1,0}^{(S)}, \tag{36}$$

$$\mathbf{u}_{1,0}^{(T)} = -\boldsymbol{\nabla}p_{1,0}^{(T)}. \tag{37}$$

Importantly, we observe that this velocity field $\mathbf{u}_{1,0}$ is the time-derivative of a function proportional to $A(t)$. We will see in Sec. III D that this implies that the net displacement at order α of a material point due to one full scan of the heat spot is precisely zero; for this reason, to understand the time-averaged trajectories of tracers seen in experiments [34] due to repeated scanning of the heat spot, we solve for higher-order contributions to the instantaneous flow field in Secs. II G and II H.

2. Physical mechanism for general heat spot

Although we have not yet fully solved explicitly for the leading-order instantaneous flow (at order α) induced by a heat spot, it is already possible to gain physical understanding from the general results of Sec. II F 1, in terms of thermal expansion.

We start by interpreting physically the two terms contributing to the general velocity field $\mathbf{u}_{1,0}$ at order α in Eq. (35). In experimental temperature-field measurements [28], the heat spot appears to switch on gradually at the start of the scan path, i.e., the amplitude of the temperature perturbation increases; similarly the temperature perturbation appears to switch off gradually at the end of the scan path. In those experiments, the reason for this was reduced efficiency of the laser deflector for large angles; however, more generally, for any finite scan path, the amplitude of the heat spot must increase from zero at the start of the scan path and decrease to zero at the end, i.e., the amplitude must vary with time.

The first contribution to the velocity field, $A'(t)\mathbf{u}_{1,0}^{(S)}(x-t,y)$, is proportional to the rate of change of the heat-spot amplitude. Thus, the velocity field $\mathbf{u}_{1,0}^{(S)}(x-t,y)$ is associated with the switching-on
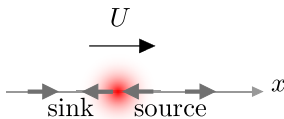
FIG. 4. Cartoon of the physical mechanism for the instantaneous flow field contribution $\mathbf{u}_{1,0}^{(T)}$ associated with translation of the heat spot (i.e., temperature perturbation) at order α, based on the case of a constant-amplitude heat spot in Ref. [30]. The heat-spot shape (shown in red), which is specified by the function $\Theta(x - t, y)$ in our mathematical model, translates in the positive x direction. At the front of the heat spot, the heat spot is arriving, so the temperature is locally increasing, $\partial\Theta/\partial t > 0$, producing a hydrodynamic source. At the back, the heat spot is leaving, so instead $\partial\Theta/\partial t < 0$, resulting in a sink.

of the heat spot. In more detail, Eq. (32) states that the divergence of the flow contribution $\mathbf{u}_{1,0}^{(S)}$ is given by the shape of the heat spot Θ, a heat source. Physically, the heat spot causes a local increase in the volume of the fluid as it switches on, i.e., thermal expansion. Mass is conserved, so there must be a fluid flux outwards from the heat spot. We therefore expect the instantaneous flow $\mathbf{u}_{1,0}^{(S)}$ to be a (2D) source flow in the far field, decaying spatially as $1/r$, where r is the distance from the center of the heat spot.

Note that experimental measurements show that the average speed of tracers over many scans of the heat spot instead decays as $1/r^2$ in the far field [34]. It is therefore important to distinguish between the instantaneous fluid velocity field induced by the heat spot during one scan (which we focus on in this section) and the time-averaged velocity of tracers (or material points) in the fluid. We emphasize that existing experimental data [28,30,34] deal with the average velocity of tracers over many scans, not with the instantaneous fluid flow.

The second contribution to the velocity field, $A(t)\mathbf{u}_{1,0}^{(T)}(x - t, y)$, is instead proportional to the amplitude itself of the heat spot; it is nonzero even if the heat spot has constant amplitude. We explain here why the flow $\mathbf{u}_{1,0}^{(T)}$ is associated with the translation of the heat spot, adapting for this term the physical mechanism from Ref. [30]. The velocity field $\mathbf{u}_{1,0}^{(T)}$ satisfies the equation

$$\nabla \cdot \mathbf{u}_{1,0}^{(T)}(x - t, y) = \frac{\partial}{\partial t}\Theta(x - t, y), \tag{38}$$

where we recall that the heat-spot shape Θ has the interpretation of a heat spot of constant amplitude. We illustrate the physical mechanism in Fig. 4. At the front of the heat spot, the forcing $\partial\Theta/\partial t$ is positive, a source term, because the translating heat spot is arriving, i.e., the fluid is heating up locally. At the back of the heat spot, the forcing $\partial\Theta/\partial t$ is negative, a sink term, because the heat spot is leaving, i.e., the fluid is cooling down locally. Therefore, based on this mechanism, we expect the velocity field $\mathbf{u}_{1,0}^{(T)}$ to be a hydrodynamic source dipole in the far field, decaying as $1/r^2$.

The physical mechanism presented here, for the full flow $\mathbf{u}_{1,0}$, builds on that presented in earlier work [30] that focused on a constant-amplitude heat spot that translates along an infinite scan path. For that case, from the mechanism in Ref. [30], the source at the front and sink at the back suggest that the far-field, leading-order instantaneous flow is a source dipole, decaying as $1/r^2$. This is reflected in the translation contribution in our theory. However, for a general, time-varying heat-spot amplitude, there is an important difference between the prediction by our theory and by the constant-amplitude mechanism. Our theory predicts that the time-variation of the amplitude generically produces the far field of the full leading-order instantaneous flow, decaying as $1/r$, instead of the $1/r^2$ scaling purely due to heat-spot translation for the special, constant-amplitude case. We show these results explicitly for a Gaussian heat spot in Sec. II F 4, confirming the far-field behavior in Sec. II F 6.

We note that the physical mechanism for the leading-order instantaneous flow does not rely on thermal viscosity changes, which are quantified by the thermal viscosity coefficient β; this reflects the fact that thermal expansion alone is responsible for the leading-order flow.
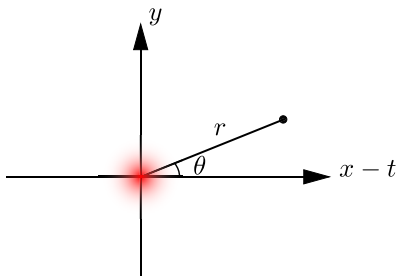
FIG. 5. Polar coordinates with origin coinciding with the center of the heat spot at time t.

Finally, we observe that the velocity field $\mathbf{u}_{1,0}$, given by Eq. (35), is linear in the heat-spot amplitude $A(t)$. To provide physical interpretation of this mathematical symmetry, we consider the case of localized cooling instead of heating. This could potentially be achieved in future experiments by uniformly heating a large domain except a localized spot, the "cool" spot (in a relative sense). From our theory, if we have a cool spot $[A(t) \leqslant 0]$ instead of a heat spot, then the instantaneous flow at order α is reversed. This is consistent with the mechanism described above.

3. Pressure field

We discussed above the physical mechanism for the leading-order instantaneous flow induced by a general heat spot. To confirm this intuition mathematically, we now focus on the specific Gaussian heat spot in Eq. (18), i.e., Eq. (30) with shape function $\Theta(x, y) = \exp[-(x^2 + y^2)/2]$, and solve Eq. (28) explicitly for the pressure $p_{1,0}$ at order α. The Gaussian heat spot has circular symmetry, so we introduce plane polar coordinates (r, θ) with origin at the center of the heat spot at time t (Fig. 5), given by

$$x - t = r \cos \theta, \tag{39}$$

$$y = r \sin \theta. \tag{40}$$

As explained in Sec. II F 1, we first solve Eq. (32) for the pressure field $p_{1,0}^{(S)}$ associated with the time-variation of the amplitude of the heat spot. Since the forcing has circular symmetry, we choose an ansatz with the same symmetry, $p_{1,0}^{(S)} = p_{1,0}^{(S)}(r)$. The Poisson equation then simplifies to the ordinary differential equation

$$\frac{1}{r} \frac{\partial}{\partial r} \left(r \frac{\partial p_{1,0}^{(S)}}{\partial r} \right) = -\exp(-r^2/2). \tag{41}$$

We integrate this, imposing the boundary condition that the solution is nonsingular at the center of the heat spot. This gives the pressure $p_{1,0}^{(S)}$ as

$$p_{1,0}^{(S)}(r) = -\tfrac{1}{2} \mathrm{E}_1(r^2/2) - \ln r, \tag{42}$$

where the exponential integral E_1 is defined as

$$\mathrm{E}_1(z) \equiv \int_z^\infty \frac{\exp(-s)}{s} \, ds. \tag{43}$$

From Eq. (33), the full pressure field $p_{1,0}$ at order α is thus given by

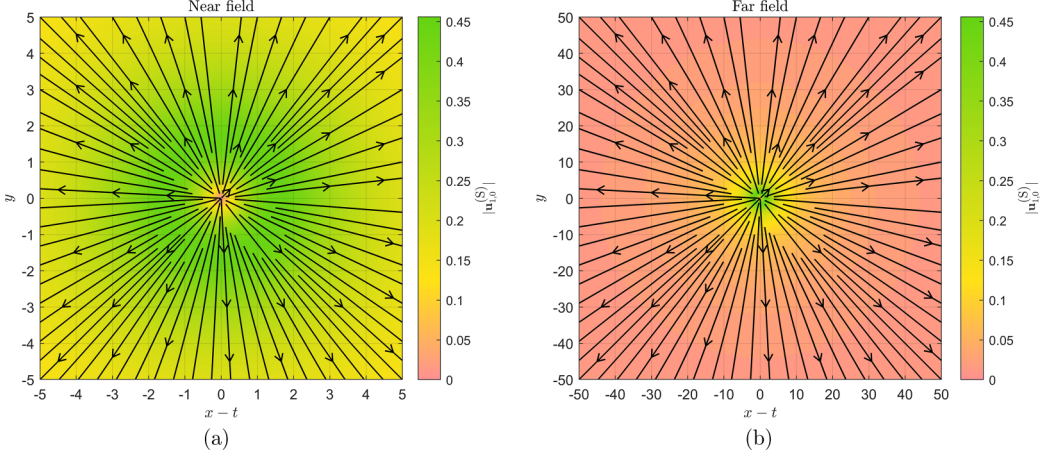$$p_{1,0}(x, y, t) = A'(t) p_{1,0}^{(S)}(x - t, y) + A(t) p_{1,0}^{(T)}(x - t, y), \tag{44}$$

FIG. 6. Streamlines for the flow field $\mathbf{u}_{1,0}^{(S)}(x-t, y)$ [as in Eq. (35) for the instantaneous flow at order α] associated with the time-variation of the heat-spot amplitude. (a) Streamlines for $-5 \leqslant x - t, y \leqslant 5$, close to the heat spot (near field), with magnitude of the velocity field $|\mathbf{u}_{1,0}^{(S)}|$ indicated by color. (b) Streamlines for $-50 \leqslant x - t, y \leqslant 50$ to illustrate far-field behavior.

where the pressure $p_{1,0}^{(T)}(x - t, y)$ is given by

$$p_{1,0}^{(T)}(x - t, y) = \frac{(x - t)[1 - \exp(-r^2/2)]}{r^2}.$$

(45)

4. Velocity field: $\mathbf{u}_{1,0}^{(S)}$ term associated with time-variation of heat-spot amplitude

The corresponding full instantaneous velocity field at order α [repeating Eq. (35) for convenience] is given by

$$\mathbf{u}_{1,0}(x, y, t) = \frac{\partial}{\partial t}\left[A(t)\mathbf{u}_{1,0}^{(S)}(x - t, y)\right] \equiv A'(t)\mathbf{u}_{1,0}^{(S)}(x - t, y) + A(t)\mathbf{u}_{1,0}^{(T)}(x - t, y),$$

(46)

where, from Eqs. (36) and (37), the two contributing, irrotational velocity fields are given by

$$\mathbf{u}_{1,0}^{(S)}(x - t, y) = \frac{(x - t)[1 - \exp(-r^2/2)]}{r^2}\mathbf{e}_x + \frac{y[1 - \exp(-r^2/2)]}{r^2}\mathbf{e}_y \equiv \frac{1 - \exp(-r^2/2)}{r}\mathbf{e}_r, \quad (47)$$

$$\mathbf{u}_{1,0}^{(T)}(x - t, y) = -\mathbf{e}_x\left\{\frac{1}{r^2} - \frac{2(x - t)^2}{r^4} + \left[-\frac{1}{r^2} + \frac{2(x - t)^2}{r^4} + \frac{(x - t)^2}{r^2}\right]\exp(-r^2/2)\right\}$$

$$- \mathbf{e}_y\left\{-\frac{2(x - t)y}{r^4} + \left[\frac{2(x - t)y}{r^4} + \frac{(x - t)y}{r^2}\right]\exp(-r^2/2)\right\}.$$

(48)

In the above, $\mathbf{e}_x$ and $\mathbf{e}_y$ are unit vectors in the x and y directions, respectively; $\mathbf{e}_r \equiv \frac{x-t}{r}\mathbf{e}_x + \frac{y}{r}\mathbf{e}_y$ is the radial unit vector (from the center of the heat spot). This is a linear superposition of two separate flows, as interpreted physically in Sec. II F 2: $A'(t)\mathbf{u}_{1,0}^{(S)}(x - t, y)$ associated with the time-variation of the amplitude of the heat spot ("switching on" and "switching off") and $A(t)\mathbf{u}_{1,0}^{(T)}(x - t, y)$ associated with the translation of the heat spot. We now examine the flow fields $\mathbf{u}_{1,0}^{(S)}$ and $\mathbf{u}_{1,0}^{(T)}$. We illustrate the flow field $\mathbf{u}_{1,0}^{(S)}$ in Fig. 6, with the near field in Fig. 6(a) and the far field in Fig. 6(b). (Recall that the length scales are in units of a, the characteristic radius of the Gaussian temperature profile.) The flow is purely radial, inheriting the symmetry of the heat spot. Its magnitude, illustrated on a log–log
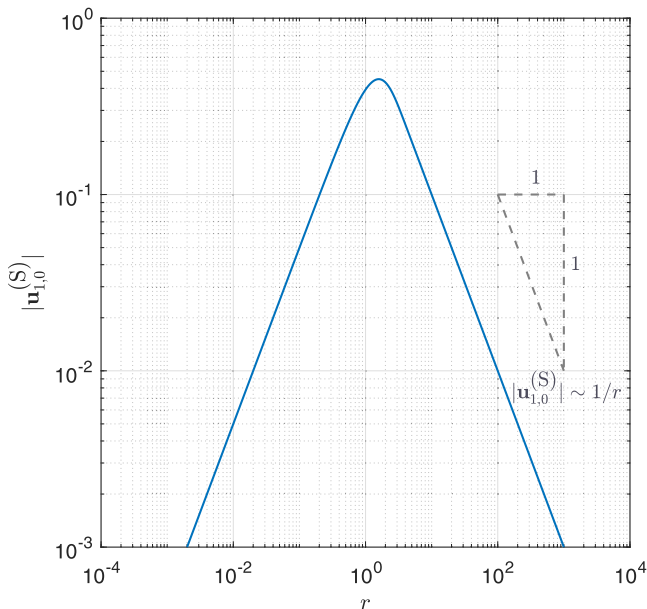
FIG. 7. Magnitude of the flow field at order α associated with the time-variation of the heat-spot amplitude, $|\mathbf{u}_{1,0}^{(S)}|$ [Eq. (49)], against the radial distance r to the center of the heat spot, plotted on a log–log scale. The flow is a regularized source: it is zero at the center of the heat spot, while its far-field behavior is given by $|\mathbf{u}_{1,0}^{(S)}| \sim 1/r$.

scale in Fig. 7, is given by

$$\left|\mathbf{u}_{1,0}^{(S)}\right| = \frac{1 - \exp(-r^2/2)}{r}. \tag{49}$$

At the center of the heat spot, this is zero, so we have a regularized version of the flow due to a point source. In the far field, we have

$$\mathbf{u}_{1,0}^{(S)}(x-t, y) \sim \frac{(x-t)}{r^2}\mathbf{e}_x + \frac{y}{r^2}\mathbf{e}_y \equiv \frac{1}{r}\mathbf{e}_r. \tag{50}$$

This is a source flow, centered on the heat spot, as we expect from the physical mechanism (Sec. II F 2). The magnitude of this flow correspondingly decays as $|\mathbf{u}_{1,0}^{(S)}| \sim 1/r$.

5. Velocity field: $\mathbf{u}_{1,0}^{(T)}$ term associated with translation of the heat spot

We illustrate in Fig. 8 the flow field $\mathbf{u}_{1,0}^{(T)}$ associated with translation of the heat spot, with a plot of the streamlines in the near field in Fig. 8(a) and the far field in Fig. 8(b). The magnitude, $|\mathbf{u}_{1,0}^{(T)}|$, is given by

$$\left|\mathbf{u}_{1,0}^{(T)}\right| = \frac{1}{r^2}\{[(1+r^2)\exp(-r^2/2) - 1]^2 + r^2\exp(-r^2)[2\exp(r^2/2) - (2+r^2)]\sin^2\theta\}^{1/2}, \tag{51}$$

which is an increasing function of $\sin^2\theta$ at any fixed radius r. The magnitude $|\mathbf{u}_{1,0}^{(T)}|$ is visualized in Fig. 9, a log–log plot of the speed $|\mathbf{u}_{1,0}^{(T)}|$ against the radius r, along radial lines $\theta = 0$, $\pi/8$, $\pi/4$, $3\pi/8$, and $\pi/2$.

These plots support the physical mechanism for this flow, $\mathbf{u}_{1,0}^{(T)}$, proposed in Sec. II F 2. We see in Fig. 8(a) a source on the right, where the heat spot is arriving so that the fluid is heating up, and a sink on the left, where the heat spot is leaving so that the fluid is cooling down. In agreement with this mechanism, we have shown mathematically that the far field of the flow $\mathbf{u}_{1,0}^{(T)}(x-t, y)$ is a
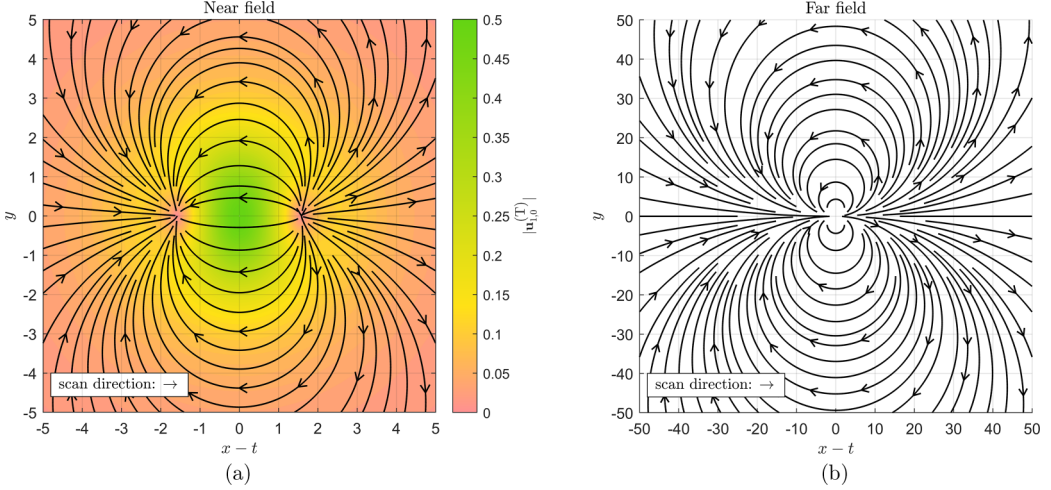
FIG. 8. Streamlines for the velocity field $\mathbf{u}_{1,0}^{(T)}(x - t, y)$ [as in Eq. (35) for the instantaneous flow at order α] associated with translation of the heat spot in the positive x direction (scan direction). (a) Streamlines for $-5 \leqslant x - t, y \leqslant 5$, close to the heat spot (near field), with magnitude of the velocity field $|\mathbf{u}_{1,0}^{(T)}|$ indicated by color. (b) Streamlines for $-50 \leqslant x - t, y \leqslant 50$ to illustrate far-field behavior.

hydrodynamic source dipole, given by

$$\mathbf{u}_{1,0}^{(T)}(x - t, y) \sim -\left\{ \mathbf{e}_x \left[\frac{1}{r^2} - \frac{2(x - t)^2}{r^4} \right] + \mathbf{e}_y \left[-\frac{2(x - t)y}{r^4} \right] \right\}, \tag{52}$$

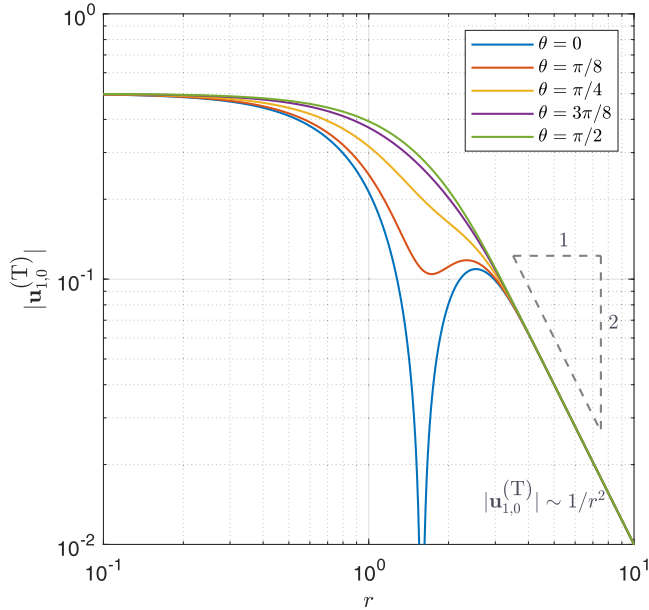with magnitude decaying as $|\mathbf{u}_{1,0}^{(T)}| \sim 1/r^2$.

FIG. 9. Magnitude of the flow field at order α associated with translation of the heat spot, $|\mathbf{u}_{1,0}^{(T)}|$ [Eq. (51)], against the radial distance r to the center of the heat spot, plotted on a log–log scale, for $\theta = 0, \pi/8, \pi/4, 3\pi/8,$ and $\pi/2$. The far-field behavior is given by $|\mathbf{u}_{1,0}^{(T)}| \sim 1/r^2$.

6. Far-field behaviour

As a reminder, the full instantaneous velocity field $\mathbf{u}_{1,0}$ at order α is a linear superposition [given by Eq. (46) for general amplitude function $A(t)$] of the flows $\mathbf{u}_{1,0}^{(S)}$ [Eq. (47)] and $\mathbf{u}_{1,0}^{(T)}$ [Eq. (48)]. We have seen that the far field of $\mathbf{u}_{1,0}^{(S)}$ is a source flow [Eq. (50)], which decays as $1/r$, and the far field of $\mathbf{u}_{1,0}^{(T)}$ is a source dipole [Eq. (52)], which decays as $1/r^2$. Therefore, provided $A'(t) \neq 0$, the far field of the full instantaneous flow $\mathbf{u}_{1,0}$ at order α is given by

$$\mathbf{u}_{1,0}(x, y, t) \sim \frac{A'(t)}{r} \mathbf{e}_r, \tag{53}$$

i.e., a source flow, proportional to the rate of change of the amplitude of the heat spot and decaying spatially as $1/r$. This dominates over the contribution due to the translation of the heat spot, thus illustrating the importance of the time-dependence of the heat-spot amplitude in our model. For example, this is the relevant behavior for the case of a sinusoidal amplitude function, which we will illustrate later in this section.

At times t such that the heat-spot amplitude function is stationary with respect to time [i.e., at a local maximum or minimum, $A'(t) = 0$], the far-field behavior of the instantaneous flow $\mathbf{u}_{1,0}$ is instead given by

$$\mathbf{u}_{1,0}(x, y, t) \sim -A(t) \left\{ \mathbf{e}_x \left[\frac{1}{r^2} - \frac{2(x-t)^2}{r^4} \right] + \mathbf{e}_y \left[-\frac{2(x-t)y}{r^4} \right] \right\}, \tag{54}$$

which is a hydrodynamic source dipole, proportional to the amplitude of the heat spot, and decaying spatially as $1/r^2$ (thus slower than the previous case). This is relevant if, for example, the amplitude of the heat spot remains constant at some maximum value for most of the scan period (when the heat spot is away from the ends of the scan path where it switches on and off) or alternatively, as in previous theoretical modeling [30], the heat-spot amplitude is identically a constant and the scan path is infinitely long.

7. Full velocity field

In our work so far, we have allowed the amplitude function $A(t)$ to be fully general. To visualize the full instantaneous velocity field $\mathbf{u}_{1,0}(x, y, t)$ at order α at a given time t [Eqs. (46)–(48)] in this section, we need to choose a particular amplitude function $A(t)$. Following Ref. [28], we choose a sinusoidal amplitude function $A(t)$ given by

$$A(t) = \cos^2\left(\frac{\pi t}{2t_0}\right), \tag{55}$$

valid for $-t_0 \leqslant t \leqslant t_0$, where $t_0 = \ell$ is half the scan period in dimensionless terms. For this amplitude function [Eq. (55)] and for $t_0 = 1.375$ (to match experiments [34]), we plot the instantaneous streamlines of the velocity field $\mathbf{u}_{1,0}$ at order α in Fig. 10 over the course of the first half of a scan period. The center of the heat spot is indicated with a red dot. The streamlines for the second half of the scan period may be obtained by symmetry.

As expected, near the start of the scan period (e.g., panels for $t = -1.375$ and $t = -0.275$), when the amplitude of the heat spot is small and increasing, the instantaneous flow is dominated by the contribution $A'(t)\mathbf{u}_{1,0}^{(S)}(x - t, y)$, associated with the time-variation of the amplitude of the heat spot. The heat spot is switching on, giving a source flow.

At the instant $t = 0$ (halfway through the scan period) when the amplitude of the heat spot reaches its maximum value, there is no switching-on contribution to the flow. The instantaneous flow is then simply given by the contribution $A(t)\mathbf{u}_{1,0}^{(T)}(x - t, y)$, associated with the translation of the heat spot, with a source at the front and a sink at the back.

For the sinusoidal amplitude function chosen in Eq. (55), the characteristic timescale over which the heat spot switches on and off is the same as the scan period, as in the experiments and numerical simulations of Ref. [28]. Except at $t = -t_0$, $t = 0$, and $t = t_0$, the rate of change of the amplitude
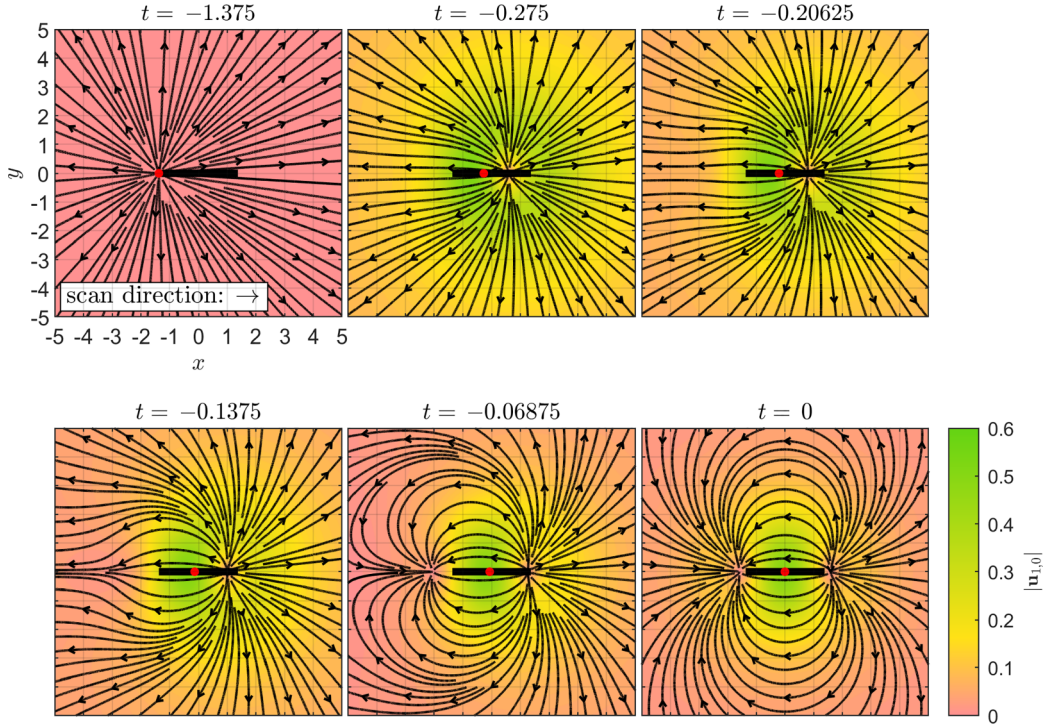
FIG. 10. Snapshots of the streamlines of the instantaneous fluid velocity field $\mathbf{u}_{1,0}$ at order α, i.e., leading order, over the course of half a scan period, $-t_0 \leqslant t \leqslant 0$, with $t_0 = 1.375$ and sinusoidal amplitude function given by Eq. (55). The heat spot translates in the positive x direction. The center of the heat spot is indicated with a red dot, while the scan path is shown as a thick black line segment.

is nonzero. For this sinusoidal amplitude function, we therefore predict that the instantaneous flow field is generically dominated by a source or sink flow in the far field, decaying as $1/r$, not by a hydrodynamic source dipole (decaying as $1/r^2$).

Clearly, alternative amplitude functions are possible. In other applications of thermoviscous flows, the heat spot may instead switch on quickly, then translate at constant amplitude for most of the scan period, before switching off quickly. An example of such a "trapezoidal" amplitude function is given by

$$A(t) = \begin{cases} \frac{1}{t_s}(t + t_0), & \text{if } -t_0 \leqslant t \leqslant -t_0 + t_s, \\ 1, & \text{if } -t_0 + t_s \leqslant t \leqslant t_0 - t_s, \\ -\frac{1}{t_s}(t - t_0), & \text{if } t_0 - t_s \leqslant t \leqslant t_0, \end{cases} \quad (56)$$

where t_s is the "switching-on" time, over which the amplitude changes from 0 to 1 or vice versa. The limit of $t_s \to 0$ corresponds to a heat spot that remains approximately stationary while it switches on quickly at the start of the scan path, then translates at constant amplitude to the end of the scan path, where it switches off. For this amplitude function, we illustrate the instantaneous streamlines of the fluid velocity $\mathbf{u}_{1,0}$ at order α during the first half of a scan period in Fig. 11 (for the case $t_s = 0.4$). In this case, the instantaneous flow field is a source dipole in the far field for most of the scan period. We remark that even though the amplitude is constant for most of the scan period, the fact that the heat spot switches on and off at the ends of the scan path is crucial for explaining the resulting net displacement of tracers.
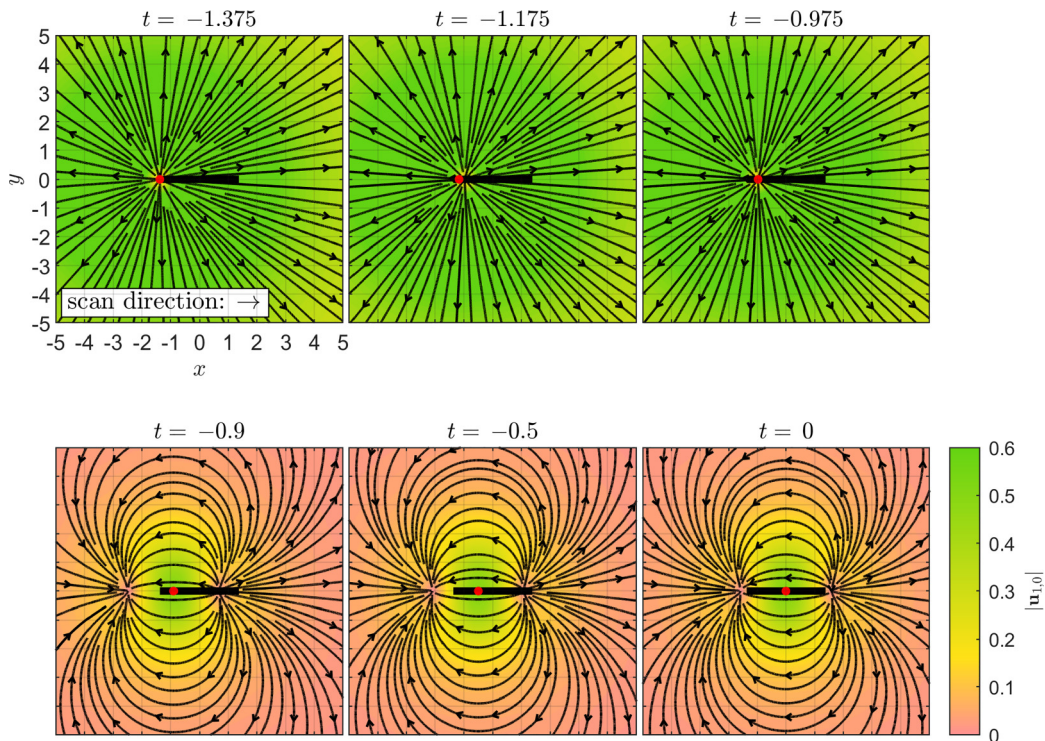
FIG. 11. Same as Fig. 10 but with a trapezoidal heat-spot amplitude function instead of sinusoidal, illustrating the case where the switching-on and switching-off of the heat spot are rapid and the amplitude is constant for most of the scan period. Snapshots of the streamlines of the instantaneous fluid velocity field $\mathbf{u}_{1,0}$ at order α, i.e., leading order, over the course of half a scan period, $-t_0 \leqslant t \leqslant 0$, with $t_0 = 1.375$ and trapezoidal amplitude function given by Eq. (56) with switching-on time $t_s = 0.4$. The heat spot translates in the positive x direction. The center of the heat spot is indicated with a red dot, while the scan path is shown as a thick black line segment.

G. Solution at order $\alpha\beta$

In Sec. II F, we solved for the leading-order instantaneous flow (order α), for a heat spot of arbitrary amplitude and Gaussian shape. We now proceed to the quadratic terms in the perturbation expansion for the flow field [Eq. (24)], as these give rise to the leading-order net displacement of tracers (Sec. IV), as in experiments.

As discussed in Sec. II E, order $\alpha\beta$ provides the first effect of thermal viscosity changes, since the flow at order β and order β^2 is zero. Furthermore, for the particular fluid (glycerol-water solution) in experiments in Ref. [34] that we compare our theory with in Sec. V, the thermal viscosity coefficient β is much larger than the thermal expansion coefficient α. Hence, we begin in this section with order $\alpha\beta$; we study the flow at order α^2 (which could be important for other liquids) in the next section. The key result in Eqs. (81) and (82) is an explicit, analytical formula for the instantaneous flow at order $\alpha\beta$ induced by the heat spot; we plot the streamlines in Fig. 12 and explain the physical mechanism for the flow in Sec. II G 6.

1. General heat spot

The Poisson equation for the pressure at order $\alpha\beta$, from Eq. (25), is given by

$$\nabla^2 p_{1,1} = -\nabla \cdot (\Delta T \, \nabla p_{1,0}) = \nabla \cdot (\Delta T \, \mathbf{u}_{1,0}), \tag{57}$$

where we have used the result that the pressure at order β is zero to simplify the equation and we have used Eq. (16) at order α to write the forcing in terms of the velocity field at order α. The result in Eq. (57) holds for any temperature profile $\Delta T(x, y, t)$ and states that the flow at order $\alpha\beta$ is incompressible.

As in Sec. II F 1, we now consider the general heat spot given by Eq. (30) and reproduced below for convenience,

$$\Delta T(x, y, t) = A(t)\Theta(x - t, y), \tag{58}$$

where $A(t)$ is the amplitude function and $\Theta(x - t, y)$ is the shape function, steady in the frame translating with the heat spot. Recall that at order α we decomposed the velocity field $\mathbf{u}_{1,0}$ [Eq. (35)] into two contributions, due to the time-variation of the heat-spot amplitude and due to the translation of the heat spot. Since Eq. (57) is linear in the pressure $p_{1,1}$ at order $\alpha\beta$, we can similarly decompose $p_{1,1}$ as

$$p_{1,1}(x, y, t) = A(t)A'(t)p_{1,1}^{(S)}(x - t, y) + A(t)^2 p_{1,1}^{(T)}(x - t, y), \tag{59}$$

where the two contributing pressure fields $p_{1,1}^{(S)}(x - t, y)$ and $p_{1,1}^{(T)}(x - t, y)$ satisfy the Poisson equations

$$\nabla^2 p_{1,1}^{(S)}(x - t, y) = \nabla \cdot \left[\Theta(x - t, y)\mathbf{u}_{1,0}^{(S)}(x - t, y)\right], \tag{60}$$

$$\nabla^2 p_{1,1}^{(T)}(x - t, y) = \nabla \cdot \left[\Theta(x - t, y)\mathbf{u}_{1,0}^{(T)}(x - t, y)\right], \tag{61}$$

respectively. The velocity field at order $\alpha\beta$, using Eq. (16), is given by

$$\mathbf{u}_{1,1} = -\nabla p_{1,1} + \Delta T \, \mathbf{u}_{1,0}, \tag{62}$$

which can be decomposed as

$$\mathbf{u}_{1,1}(x, y, t) = A(t)A'(t)\mathbf{u}_{1,1}^{(S)}(x - t, y) + A(t)^2\mathbf{u}_{1,1}^{(T)}(x - t, y), \tag{63}$$

where

$$\mathbf{u}_{1,1}^{(S)}(x - t, y) = -\nabla p_{1,1}^{(S)}(x - t, y) + \Theta(x - t, y)\mathbf{u}_{1,0}^{(S)}(x - t, y), \tag{64}$$

$$\mathbf{u}_{1,1}^{(T)}(x - t, y) = -\nabla p_{1,1}^{(T)}(x - t, y) + \Theta(x - t, y)\mathbf{u}_{1,0}^{(T)}(x - t, y). \tag{65}$$

2. Pressure field $p_{1,1}^{(S)}$, velocity field $\mathbf{u}_{1,1}^{(S)}$, and physical mechanism associated with time-variation of heat-spot amplitude for heat spot with circular symmetry

We now specialize to the case of a heat spot with circular symmetry, $\Theta(x - t, y) = \Theta(r)$. In this section, we solve Eq. (60) for the pressure $p_{1,1}^{(S)}$ at order $\alpha\beta$ associated with the time-variation of the heat-spot amplitude and then deduce that the corresponding velocity field $\mathbf{u}_{1,1}^{(S)}$ is zero.

For a heat spot with circular symmetry, both the forcing and the boundary conditions for the Poisson equation for the pressure field $p_{1,0}^{(S)}$ at order α [Eq. (32)] have circular symmetry, so that the solution $p_{1,0}^{(S)}$ and hence the velocity field $\mathbf{u}_{1,0}^{(S)}$ inherit the same symmetry. Consequently, at order $\alpha\beta$, the forcing in Eq. (60) has circular symmetry, which is inherited by the solution for the pressure, $p_{1,1}^{(S)} = p_{1,1}^{(S)}(r)$. The Poisson equation [Eq. (60)] is therefore an ordinary differential equation in r given by

$$\frac{1}{r}\frac{\partial}{\partial r}\left(r\frac{\partial p_{1,1}^{(S)}}{\partial r}\right) = -\frac{1}{r}\frac{\partial}{\partial r}\left(r\Theta\frac{\partial p_{1,0}^{(S)}}{\partial r}\right). \tag{66}$$

Integrating this, we find

$$\frac{\partial p_{1,1}^{(S)}}{\partial r} = -\Theta\frac{\partial p_{1,0}^{(S)}}{\partial r}, \tag{67}$$

where we have set the constant of integration to be zero because the velocity is not singular at the center of the heat spot. We note that in vector form, this is simply

$$\nabla p_{1,1}^{(S)} = \Theta \mathbf{u}_{1,0}^{(S)}. \tag{68}$$

Integrating again gives the pressure field $p_{1,1}^{(S)}$ at order $\alpha\beta$ associated with the time-variation of the amplitude of the heat spot as

$$p_{1,1}^{(S)}(r) = \int_r^\infty \Theta(\tilde{r}) \frac{\partial p_{1,0}^{(S)}(\tilde{r})}{\partial \tilde{r}} \, d\tilde{r}, \tag{69}$$

where we have chosen the constant of integration such that this pressure decays at infinity.

From this and Eq. (64), we deduce that the corresponding velocity field $\mathbf{u}_{1,1}^{(S)}$ at order $\alpha\beta$ associated with the time-variation of the heat-spot amplitude is given by

$$\mathbf{u}_{1,1}^{(S)} = \mathbf{0}. \tag{70}$$

With this result, we may now simplify Eq. (63) to find

$$\mathbf{u}_{1,1}(x, y, t) = A(t)^2 \mathbf{u}_{1,1}^{(T)}(x - t, y). \tag{71}$$

In other words, the flow at order $\alpha\beta$ is proportional to the flow associated with the translation of the heat spot; the rate of change of the amplitude $A'(t)$ does not feature in this expression. This holds for any heat spot with circular symmetry (the relevant case for sufficiently slow scanning).

We can now generalize and explain physically this result that for any heat spot with circular symmetry, there is no "switching-on" contribution to the velocity field at order $\alpha\beta$. Specifically, under the same assumption of a heat spot with circular symmetry, we show that the rate of change of the heat-spot amplitude $A'(t)$ in fact only contributes to the flow at orders α^m for $m \geq 0$; the flow associated with the switching-on of the heat spot originates solely from thermal expansion. Any flows due to the coupling of thermal expansion and thermal viscosity changes are therefore independent of the rate of change of the heat-spot amplitude; instead, they depend on the instantaneous value of the heat-spot amplitude itself.

Substituting the relationship between density and temperature [Eq. (19)] into mass conservation [Eq. (17)], we find

$$-\alpha\left[A'(t)\Theta(r) - \frac{A(t)\Theta'(r)(x - t)}{r}\right] + \nabla \cdot [\rho(r, t)\mathbf{u}] = 0, \tag{72}$$

where prime $(')$ indicates differentiation with respect to the argument. We introduce the velocity field $\mathbf{u}^{(S)}$ associated with the switching-on of the heat spot, which satisfies

$$-\alpha A'(t)\Theta(r) + \nabla \cdot [\rho(r, t)\mathbf{u}^{(S)}] = 0, \tag{73}$$

with the boundary conditions that $\mathbf{u}^{(S)}$ is nonsingular at the center of the heat spot and decays at infinity. In other words, by linearity, any contributions to the full velocity field $\mathbf{u}$ that involve the rate of change of the amplitude, $A'(t)$, are contained in the switching-on velocity.

At this stage, we note the circular symmetry of the problem and expect that the solution inherits this. With an ansatz of $\mathbf{u}^{(S)} = u^{(S)}(r, t)\mathbf{e}_r$, the equation becomes

$$-\alpha A'(t)\Theta(r) + \frac{1}{r}\frac{\partial}{\partial r}[r\rho(r, t)u^{(S)}(r, t)] = 0. \tag{74}$$

Integrating Eq. (74) and using the boundary conditions, we find the switching-on velocity field as

$$\mathbf{u}^{(S)}(r, t) = \frac{\alpha A'(t)}{r\rho(r, t)} \int_0^r \tilde{r}\Theta(\tilde{r}) \, d\tilde{r} \, \mathbf{e}_r. \tag{75}$$

This is linear in the rate of change of the heat-spot amplitude $A'(t)$.

Importantly, this depends only on the thermal expansion coefficient α, not the thermal viscosity coefficient β. This is because to obtain the flow $\mathbf{u}^{(S)}$ here, we have not needed to use the momentum equations. The circular symmetry of the temperature profile results in circular symmetry of the density and viscosity fields. This allows us to find the flow $\mathbf{u}^{(S)}$ purely from mass conservation; the

flow obtained in this way also solves the momentum equations, together with a pressure field $p^{(S)}$ that has circular symmetry too.

In addition to this, note that the solution $\mathbf{u}^{(S)}$ is valid for all α and β; it does not rely on the limit $\alpha, \beta \ll 1$. To enable comparison with our results from perturbation expansions, we expand $\mathbf{u}^{(S)}$ for small α to give

$$\mathbf{u}^{(S)} = \frac{\alpha A'(t)}{r} \sum_{k=0}^{\infty} [\alpha A(t) \Theta(r)]^k \int_0^r \tilde{r} \Theta(\tilde{r}) \, d\tilde{r} \, \mathbf{e}_r \equiv \alpha A'(t) \mathbf{u}_{1,0}^{(S)} + \alpha^2 A'(t) A(t) \mathbf{u}_{2,0}^{(S)} + O(\alpha^3), \quad (76)$$

where we have included the factors of $A(t)$ and $A'(t)$ so that the notation is consistent with that introduced previously. In particular, at order α we obtain

$$\mathbf{u}_{1,0}^{(S)} = \frac{1}{r} \int_0^r \tilde{r} \Theta(\tilde{r}) \, d\tilde{r} \, \mathbf{e}_r, \quad (77)$$

and at order α^2 we find

$$\mathbf{u}_{2,0}^{(S)} = \frac{\Theta(r)}{r} \int_0^r \tilde{r} \Theta(\tilde{r}) \, d\tilde{r} \, \mathbf{e}_r. \quad (78)$$

For the Gaussian temperature profile $\Theta(r) = \exp(-r^2/2)$, this recovers the result in Eq. (47) for order α and agrees with the result in Eq. (96) when we consider order α^2 in Sec. II H.

3. Pressure field

Building on our results for more general temperature profiles, we now focus on the specific Gaussian temperature profile in Eq. (18). From Eq. (71) for the flow $\mathbf{u}_{1,1}$ at order $\alpha\beta$, we only need to find the velocity field $\mathbf{u}_{1,1}^{(T)}$, associated with the translation of the heat spot. To do this, we solve in this section Eq. (61) for the corresponding pressure field $p_{1,1}^{(T)}$.

Substituting Eq. (48) into Eq. (61), the Poisson equation becomes, in polar coordinates,

$$\frac{1}{r} \frac{\partial}{\partial r} \left(r \frac{\partial p_{1,1}^{(T)}}{\partial r} \right) + \frac{1}{r^2} \frac{\partial^2 p_{1,1}^{(T)}}{\partial \theta^2} = \cos\theta \left[2r \exp(-r^2) - \frac{\exp(-r^2/2)}{r} + \frac{\exp(-r^2)}{r} \right]. \quad (79)$$

This may be solved, for example, by separation of variables and reduction of order. The pressure $p_{1,1}^{(T)}$ at order $\alpha\beta$ associated with translation of the heat spot is then given by

$$p_{1,1}^{(T)}(x-t, y) = (x-t) \left[-\frac{1}{4r^2} - \frac{1}{2r^2} \exp(-r^2/2) + \frac{3}{4r^2} \exp(-r^2) + \frac{1}{4} E_1(r^2/2) - \frac{1}{4} E_1(r^2) \right], \quad (80)$$

where we recall that E_1 is the exponential integral [defined in Eq. (43)].

4. Velocity field

From Eqs. (65), (80), and (48), we deduce that the velocity field $\mathbf{u}_{1,1}^{(T)}$ associated with the translation of the heat spot is given by

$$\mathbf{u}_{1,1}^{(T)}(x-t, y) = \mathbf{e}_x \left\{ \frac{1}{4r^2} - \frac{(x-t)^2}{2r^4} + \left[-\frac{1}{2r^2} + \frac{(x-t)^2}{r^4} \right] \exp(-r^2/2) \right.$$

$$+ \left[\frac{1}{4r^2} - \frac{(x-t)^2}{2r^4} \right] \exp(-r^2) - \frac{1}{4} E_1(r^2/2) + \frac{1}{4} E_1(r^2) \right\}$$

$$+ \mathbf{e}_y \left[-\frac{(x-t)y}{2r^4} + \frac{(x-t)y}{r^4} \exp(-r^2/2) - \frac{(x-t)y}{2r^4} \exp(-r^2) \right]. \quad (81)$$

The full instantaneous flow $\mathbf{u}_{1,1}$ at order $\alpha\beta$ is then given by Eq. (71), reproduced here for convenience,

$$\mathbf{u}_{1,1}(x, y, t) = A(t)^2 \mathbf{u}_{1,1}^{(T)}(x-t, y). \quad (82)$$
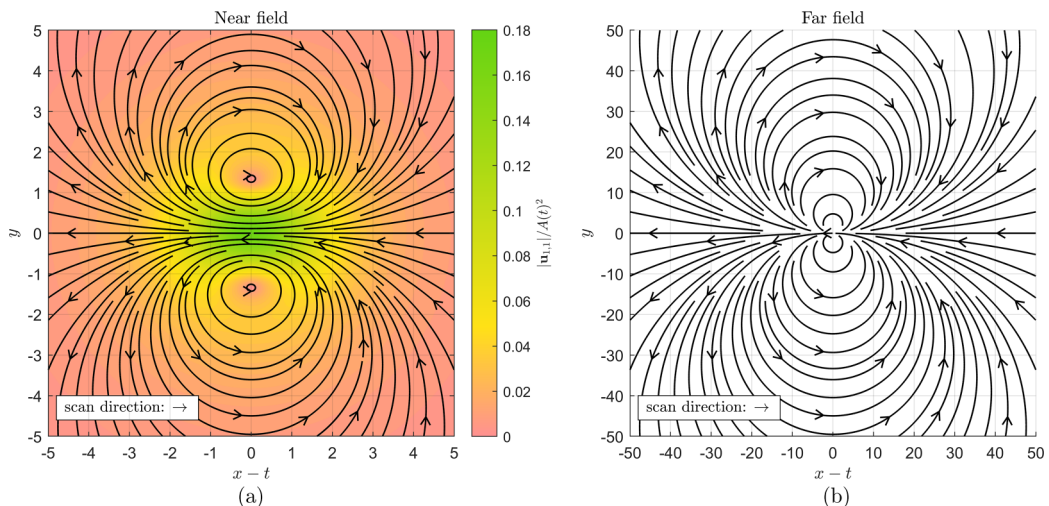
FIG. 12. Streamlines for the flow $\mathbf{u}_{1,1}$ at order $\alpha\beta$, which includes the first effect of viscosity variation with temperature. The heat spot translates in the positive x direction (scan direction). (a) Streamlines for $-5 \leqslant x - t, y \leqslant 5$, close to the heat spot (near field). The magnitude of the velocity field divided by the square of the amplitude, $|\mathbf{u}_{1,1}|/A(t)^2 = |\mathbf{u}_{1,1}^{(\mathrm{T})}|$, is indicated by color. (b) Streamlines for $-50 \leqslant x - t, y \leqslant 50$ to illustrate far-field behavior.

We plot the streamlines of the flow $\mathbf{u}_{1,1}$ at order $\alpha\beta$ in Fig. 12. To quantify the spatial variation, we plot on a log–log scale the scaled magnitude $|\mathbf{u}_{1,1}|/A(t)^2 = |\mathbf{u}_{1,1}^{(\mathrm{T})}|$ as a function of the radius r, at fixed angles $\theta = 0, \pi/8, \pi/4, 3\pi/8$, and $\pi/2$, in Fig. 13. This magnitude is given by

$$\frac{|\mathbf{u}_{1,1}|}{A(t)^2} = \left|\mathbf{u}_{1,1}^{(\mathrm{T})}\right| = \frac{1}{4r^2}\{[1 - 2\exp(-r^2/2) + \exp(-r^2) - r^2\mathrm{E}_1(r^2/2) + r^2\mathrm{E}_1(r^2)]^2$$

$$+ 4r^2[1 - \exp(-r^2/2)]^2[\mathrm{E}_1(r^2/2) - \mathrm{E}_1(r^2)]\cos^2\theta\}^{1/2}, \qquad (83)$$

which decreases as the angle θ increases from 0 to $\pi/2$.

Some properties of this instantaneous flow will be important when we compare our theory with experiments in Sec. V. First, the flow at order $\alpha\beta$ is quadratic in the amplitude, in contrast with the instantaneous flow at order α, which is instead linear in the heat-spot amplitude. Second, unlike at order α, this flow is incompressible. There are no sources or sinks in the flow. The streamlines instead form closed loops with leftward velocities on the x axis (i.e., in the opposite direction to the translation of the heat spot) and rightward velocities far from the x axis.

5. Far-field behaviour

In the far field, the instantaneous flow $\mathbf{u}_{1,1}$ at order $\alpha\beta$ is a source dipole, given by

$$\mathbf{u}_{1,1} \sim \frac{1}{4}A(t)^2\left\{\mathbf{e}_x\left[\frac{1}{r^2} - \frac{2(x-t)^2}{r^4}\right] + \mathbf{e}_y\left[-\frac{2(x-t)y}{r^4}\right]\right\}, \qquad (84)$$

with magnitude decaying as $|\mathbf{u}_{1,1}| \sim A(t)^2/4r^2$.

The $1/r^2$ decay of this flow at order $\alpha\beta$ is faster than the $1/r$ decay of the source flow that typically [for $A'(t) \neq 0$] dominates the far field of the instantaneous flow at leading order, i.e., order α. However, in Secs. III–V, we show that the leading-order average velocity of tracers inherits key features from the instantaneous flow at order $\alpha\beta$.
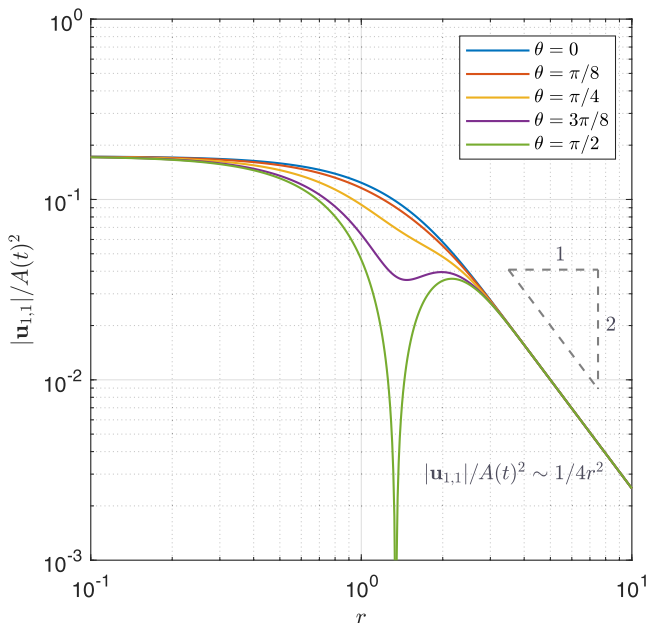
FIG. 13. Scaled magnitude of the order-$\alpha\beta$ velocity field, $|\mathbf{u}_{1,1}|/A(t)^2 = |\mathbf{u}_{1,1}^{(\mathrm{T})}|$ [Eq. (83)], against the radial distance r to the center of the heat spot, plotted on a log–log scale, for $\theta = 0$, $\pi/8$, $\pi/4$, $3\pi/8$, and $\pi/2$. The far-field behavior is given by $|\mathbf{u}_{1,1}|/A(t)^2 \sim 1/4r^2$.

6. Physical mechanism

We now propose an explanation for the physical mechanism behind our analytical result for the instantaneous flow field $\mathbf{u}_{1,1}$ at order $\alpha\beta$, i.e., for the first effect of thermal viscosity changes. As a reminder, we have already considered the contribution $A'(t)A(t)\mathbf{u}_{1,1}^{(\mathrm{S})}$, associated with the time-variation of the heat-spot amplitude at order $\alpha\beta$, in Sec. II G 2. We found that this contribution is in fact zero, $\mathbf{u}_{1,1}^{(\mathrm{S})} = \mathbf{0}$, and justified this physically: for a heat spot with circular symmetry, switching on produces a flow purely due to thermal expansion and mass conservation, independent of viscosity. The flow $\mathbf{u}_{1,1}$ is therefore proportional to the contribution $\mathbf{u}_{1,1}^{(\mathrm{T})}$ associated with the translation of the heat spot [Eq. (71)]. Recall from Eq. (65) that the velocity field $\mathbf{u}_{1,1}^{(\mathrm{T})}$ is the sum of two terms, a potential flow, $-\nabla p_{1,1}^{(\mathrm{T})}$, and the velocity field at order α associated with the translation of the heat spot, modulated by the heat-spot shape, $\Theta\mathbf{u}_{1,0}^{(\mathrm{T})}$. The streamlines for these two separate flows are plotted in Fig. 14, with $-\nabla p_{1,1}^{(\mathrm{T})}$ in Fig. 14(a) and $\Theta\mathbf{u}_{1,0}^{(\mathrm{T})}$ in Fig. 14(b). We can interpret the physical origin of each contribution to the flow field $\mathbf{u}_{1,1}^{(\mathrm{T})}$ and how they give rise to the hydrodynamic source dipole in the far field of $\mathbf{u}_{1,1}^{(\mathrm{T})}$, the direction of circulation of fluid flow, and finally the quadratic scaling of the full flow $\mathbf{u}_{1,1}$ at order $\alpha\beta$ with the heat-spot amplitude. We illustrate in Fig. 15 the interaction of thermal viscosity changes with thermal expansion. We may summarize the physical mechanism for the flow at order $\alpha\beta$ briefly as follows. The heat spot amplifies the leading-order flow (order α) associated with the translation of the heat spot. However, to enforce incompressibility of the full flow at order $\alpha\beta$, a second flow must be added to this, which compensates for the compressibility of the amplification effect.

In more detail, first, we focus on the modified leading-order flow term, $\Theta\mathbf{u}_{1,0}^{(\mathrm{T})}$ [Fig. 14(b)]. We build on previous work [29,30] that focused on flow on the x axis. First, recall from Sec. II F the physical mechanism behind the leading-order flow (order α) associated with translation of the heat spot, which arises purely due to thermal expansion. This is illustrated in Fig. 4. Considering flow on
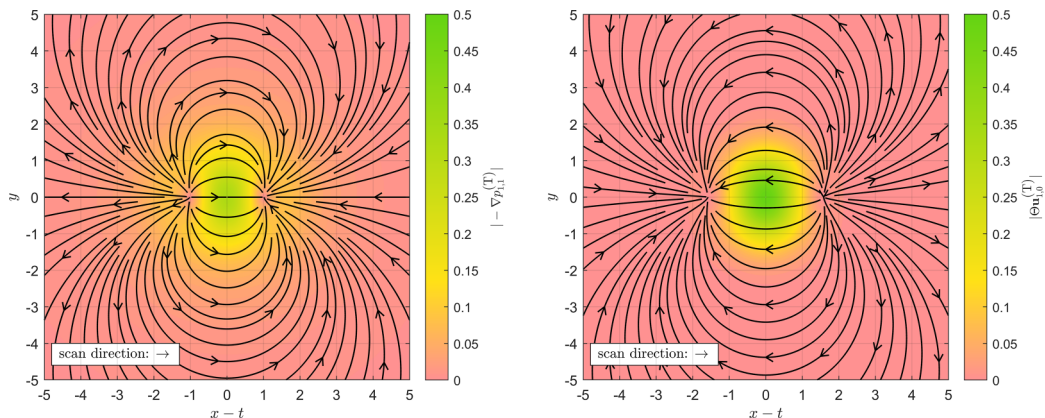
FIG. 14. Streamlines for the two terms that make up the velocity field $\mathbf{u}_{1,1}^{(T)} = -\nabla p_{1,1}^{(T)} + \Theta\mathbf{u}_{1,0}^{(T)}$ at order $\alpha\beta$, associated with the translation of the heat spot in the positive x direction (scan direction). The magnitude of each velocity field is indicated by color. (a) Streamlines of the potential flow $-\nabla p_{1,1}^{(T)}(x-t, y)$ for $-5 \leqslant x - t, y \leqslant 5$. The potential flow decays algebraically in the far field, whereas the flow $\Theta\mathbf{u}_{1,0}^{(T)}$ decays exponentially, so the potential flow dominates the far field of the flow $\mathbf{u}_{1,1}^{(T)}$ at order $\alpha\beta$. (b) Streamlines of the flow at leading order associated with translation of the heat spot, modulated by the heat-spot shape, $\Theta(x-t, y)\mathbf{u}_{1,0}^{(T)}(x-t, y)$, for $-5 \leqslant x - t, y \leqslant 5$. The envelope Θ suppresses the magnitude away from the heat spot exponentially. The contribution of the flow $\Theta\mathbf{u}_{1,0}^{(T)}$ to the velocity field $\mathbf{u}_{1,1}^{(T)}$ at order $\alpha\beta$ is thus mostly confined to the near field. In the near field, the flow $\Theta\mathbf{u}_{1,0}^{(T)}$ has larger magnitude than the potential flow $-\nabla p_{1,1}^{(T)}$, producing the leftward flow seen in the near field of the flow $\mathbf{u}_{1,1}^{(T)}$.
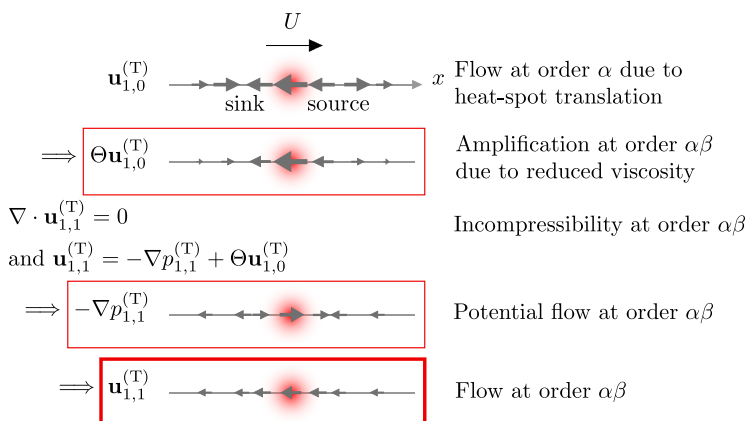

FIG. 15. Schematic explanation of the physical mechanism for the flow $\mathbf{u}_{1,1}^{(T)}$ at order $\alpha\beta$, the leading-order effect of viscosity variation, on the x axis. We begin with the flow $\mathbf{u}_{1,0}^{(T)}$ associated with the translation of the heat spot at leading order (i.e., order α), explained in the cartoon in Fig. 4. Then, we consider the first effect of thermal viscosity changes, at order $\alpha\beta$. Viscosity decreases locally due to heating. Intuitively, this amplifies the leading-order flow in the heat spot (compared with if the viscosity were instead its reference value), producing the compressible contribution $\Theta\mathbf{u}_{1,0}^{(T)}$ to the order-$\alpha\beta$ flow. However, the order-$\alpha\beta$ flow is incompressible, which is enforced by the pressure $p_{1,1}^{(T)}$ associated with heat-spot translation at order $\alpha\beta$. This adds a potential flow $-\nabla p_{1,1}^{(T)}$; mathematically, this arises from the parallel-plates geometry. The flow $\mathbf{u}_{1,1}^{(T)}$ at order $\alpha\beta$ is the combination of these two effects, amplification and incompressibility.

the x axis for a heat spot translating rightwards, there is a source on the right, due to heating as the heat spot arrives, and a sink on the left, due to cooling as the heat spot leaves. Thus, the flow near the heat spot is leftwards, i.e., from the source to the sink, and the flow on the x axis outside these two stagnation points is rightwards. This flow at order α does not take into account any thermal viscosity changes; it treats the viscosity as constant at its reference value.

We can now use this flow $\mathbf{u}_{1,0}^{(\mathrm{T})}$ to explain the contribution $\Theta\mathbf{u}_{1,0}^{(\mathrm{T})}$ to the flow $\mathbf{u}_{1,1}^{(\mathrm{T})}$. Heating decreases the viscosity of the fluid locally [Eq. (20)] from the reference value and is quantified by the heat-spot shape function $\Theta(x - t, y)$ [Eq. (30)]. Therefore, a given pressure gradient is able to drive a larger flow [Eq. (16)]; in other words, the reduced viscosity locally amplifies the leading-order flow $\mathbf{u}_{1,0}^{(\mathrm{T})}$ associated with heat-spot translation (at order α). This amplification is the leading-order effect of thermal viscosity changes, captured by the thermal viscosity coefficient β and occurring at order $\alpha\beta$. From our theory, this amplification correction at order $\alpha\beta$ is given by $\Theta\mathbf{u}_{1,0}^{(\mathrm{T})}$, which is highly localized to the heat spot due to its exponential decay, inherited from the localized temperature perturbation. It is therefore mainly the flow near the heat spot, which is leftward, that is amplified, instead of the rightward flow further away, where the temperature and viscosity perturbations are exponentially small.

However, the term $\Theta\mathbf{u}_{1,0}^{(\mathrm{T})}$ explained above cannot be the full velocity field $\mathbf{u}_{1,1}^{(\mathrm{T})}$ associated with heat-spot translation at order $\alpha\beta$. This is because the amplification correction flow $\Theta\mathbf{u}_{1,0}^{(\mathrm{T})}$ is compressible; the streamlines in Fig. 14(b) clearly show a source on the right and a sink on the left. In contrast, the total flow $\mathbf{u}_{1,1}^{(\mathrm{T})}$ at order $\alpha\beta$ is incompressible. We found analytically that the flow $\mathbf{u}_{1,1}^{(\mathrm{T})}$ is leftwards everywhere on the x axis (Fig. 12), whereas the amplification correction flow $\Theta\mathbf{u}_{1,0}^{(\mathrm{T})}$ is only leftwards in the near field, inherited from $\mathbf{u}_{1,0}^{(\mathrm{T})}$. These two physical features of $\Theta\mathbf{u}_{1,0}^{(\mathrm{T})}$ indicate that there must be another contribution to the flow $\mathbf{u}_{1,1}^{(\mathrm{T})}$ at order $\alpha\beta$. This is the potential flow $-\boldsymbol{\nabla} p_{1,1}^{(\mathrm{T})}$, which arises mathematically from the parallel-plates geometry.

This potential flow $-\boldsymbol{\nabla} p_{1,1}^{(\mathrm{T})}$ [Fig. 14(a)] enforces the incompressibility of the velocity field $\mathbf{u}_{1,1}^{(\mathrm{T})}$ at order $\alpha\beta$. The divergence of the potential flow therefore must exactly cancel that of the amplification correction flow $\Theta\mathbf{u}_{1,0}^{(\mathrm{T})}$, which is expressed mathematically as

$$\boldsymbol{\nabla} \cdot \left(-\boldsymbol{\nabla} p_{1,1}^{(\mathrm{T})} \right) = -\boldsymbol{\nabla} \cdot \left(\Theta\mathbf{u}_{1,0}^{(\mathrm{T})} \right). \tag{85}$$

This is simply the Poisson equation we solved for the pressure field earlier [Eq. (61)]. We plot the left-hand side, $\boldsymbol{\nabla} \cdot (-\boldsymbol{\nabla} p_{1,1}^{(\mathrm{T})})$, in Fig. 16(b). Red indicates a source [$\boldsymbol{\nabla} \cdot (-\boldsymbol{\nabla} p_{1,1}^{(\mathrm{T})}) > 0$]; blue indicates a sink [$\boldsymbol{\nabla} \cdot (-\boldsymbol{\nabla} p_{1,1}^{(\mathrm{T})}) < 0$]. We see a source on the left, to compensate for the sink on the left in the amplification correction flow $\Theta\mathbf{u}_{1,0}^{(\mathrm{T})}$, and a sink on the right, to compensate for the source in $\Theta\mathbf{u}_{1,0}^{(\mathrm{T})}$. Away from these red and blue regions in the near field in Fig. 16(b), the divergence is exponentially small due to decay of the temperature profile. For comparison, we also plot the equivalent at order α, $\boldsymbol{\nabla} \cdot (-\boldsymbol{\nabla} p_{1,0}^{(\mathrm{T})})$, in Fig. 16(a).

At order $\alpha\beta$, the source on the left and sink on the right give rise to the far field of the potential flow $-\boldsymbol{\nabla} p_{1,1}^{(\mathrm{T})}$, a hydrodynamic source dipole, which decays algebraically. This is also precisely the far field of the full velocity field $\mathbf{u}_{1,1}^{(\mathrm{T})}$ at order $\alpha\beta$ due to heat-spot translation, because the amplification contribution $\Theta\mathbf{u}_{1,0}^{(\mathrm{T})}$ decays exponentially.

We return now to the incompressible velocity field $\mathbf{u}_{1,1}^{(\mathrm{T})} = -\boldsymbol{\nabla} p_{1,1}^{(\mathrm{T})} + \Theta\mathbf{u}_{1,0}^{(\mathrm{T})}$ at order $\alpha\beta$, shown in Fig. 12. Near the heat spot (translating rightwards), the leftward flow $\Theta\mathbf{u}_{1,0}^{(\mathrm{T})}$ due to the amplification effect dominates. In the far field, the hydrodynamic source dipole from the potential flow $-\boldsymbol{\nabla} p_{1,1}^{(\mathrm{T})}$ dominates. Together, these contributions give rise to a circulatory flow on each side of the x axis. We revisit this explanation in Sec. IV when we consider the net displacement of material points due to the scanning of the heat spot.
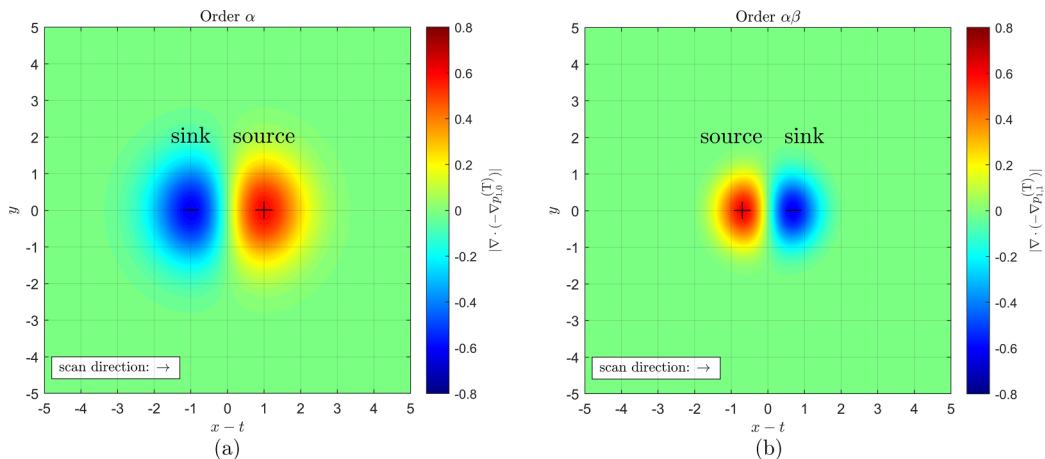
FIG. 16. Divergence of potential flow fields $-\nabla p_{1,0}^{(T)}$ at order α (left) and $-\nabla p_{1,1}^{(T)}$ at order $\alpha\beta$ (right) associated with translation of the heat spot in the positive x direction (scan direction). Red indicates a source (positive divergence); blue indicates a sink (negative divergence); green indicates that the magnitude of the divergence is small. (a) Filled contour plot for $\nabla \cdot (-\nabla p_{1,0}^{(T)})$. (b) Filled contour plot for $\nabla \cdot (-\nabla p_{1,1}^{(T)})$.

Finally, we note that one may adapt the physical explanation of the flow $\mathbf{u}_{1,1}(x, y, t) = A(t)^2 \mathbf{u}_{1,1}^{(T)}(x - t, y)$ at order $\alpha\beta$ to the case of a cool spot $[A(t) \mapsto -A(t)]$; the flow is the same as for a heat spot, consistent with the quadratic scaling with heat-spot amplitude.

H. Solution at order α^2

Having computed the leading-order instantaneous flow (order α in Sec. II F) and the leading-order effect of thermal viscosity changes (order $\alpha\beta$ in Sec. II G), we now turn our attention to order α^2, i.e., the other quadratic order. Previous work [30] has focused on the interaction between thermal expansion and thermal viscosity changes at order $\alpha\beta$, and neglected flow at order α^2. However, for some fluids, the thermal expansion coefficient α and thermal viscosity coefficient β may be of comparable magnitude [39]; hence, the flow at order α^2 could be of comparable magnitude to that at order $\alpha\beta$. In this section, to complete our understanding of quadratic effects for an arbitrary fluid, we therefore solve for the instantaneous flow at order α^2. The analytical formula for this is given by Eqs. (98)–(100). The streamlines of the two separate contributions to the flow at order α^2 are plotted in Figs. 17 and 18, while in Sec. II H 6, we provide a physical explanation for the flow.

1. General heat spot

The Poisson equation for pressure at order α^2 [from Eq. (25)] is given by

$$\nabla^2 p_{2,0} = \nabla \cdot (\Delta T \, \nabla p_{1,0}) = -\nabla \cdot (\Delta T \, \mathbf{u}_{1,0}), \tag{86}$$

where we recall that ΔT is the temperature profile (general) and $\mathbf{u}_{1,0}$ is the instantaneous flow at order α. Importantly, this Poisson equation is almost identical to the equation at order $\alpha\beta$, Eq. (57), differing only by a factor of -1. By linearity, the solution for the pressure $p_{2,0}$ at order α^2 is therefore given by

$$p_{2,0}(x, y, t) = -p_{1,1}(x, y, t). \tag{87}$$

For a general heat spot as in Eq. (30), we decompose this as

$$p_{2,0}(x, y, t) = A(t)A'(t)p_{2,0}^{(S)}(x - t, y) + A(t)^2 p_{2,0}^{(T)}(x - t, y), \tag{88}$$

just as in Eq. (59). The pressure field $p_{2,0}^{(S)}$ is associated with the time-variation of the amplitude of the heat spot ("switching on"). The pressure field $p_{2,0}^{(T)}$ is associated with the translation of the heat spot. By Eq. (87), we can relate these pressures at order α^2 to those at order $\alpha\beta$ as

$$p_{2,0}^{(S)}(x - t, y) = -p_{1,1}^{(S)}(x - t, y), \tag{89}$$

$$p_{2,0}^{(T)}(x - t, y) = -p_{1,1}^{(T)}(x - t, y). \tag{90}$$

The velocity field at order α^2, from Eq. (24), is a potential flow given by

$$\mathbf{u}_{2,0} = -\boldsymbol{\nabla} p_{2,0}. \tag{91}$$

We decompose this as

$$\mathbf{u}_{2,0}(x, y, t) = A(t)A'(t)\mathbf{u}_{2,0}^{(S)}(x - t, y) + A(t)^2 \mathbf{u}_{2,0}^{(T)}(x - t, y), \tag{92}$$

where

$$\mathbf{u}_{2,0}^{(S)}(x - t, y) = -\boldsymbol{\nabla} p_{2,0}^{(S)}(x - t, y), \tag{93}$$

$$\mathbf{u}_{2,0}^{(T)}(x - t, y) = -\boldsymbol{\nabla} p_{2,0}^{(T)}(x - t, y). \tag{94}$$

While the pressure fields at order α^2 and order $\alpha\beta$ differ only by a factor of -1, the velocity fields will be qualitatively different in structure. This is because the instantaneous flow at order α^2 is purely a potential flow and is compressible, whereas the flow at order $\alpha\beta$ instead has two separate contributions (a potential flow and the heat-spot-modulated leading-order flow) and is incompressible.

2. Pressure field $p_{2,0}^{(S)}$, velocity field $\mathbf{u}_{2,0}^{(S)}$, and physical mechanism associated with time-variation of heat-spot amplitude for heat spot with circular symmetry

As in Sec. II G 2 for order $\alpha\beta$, we now specialize to a heat spot with circular symmetry, i.e., with shape function $\Theta(x - t, y) = \Theta(r)$. By Eqs. (89) and (69), the pressure field $p_{2,0}^{(S)}$ at order α^2 associated with the time-variation of the heat-spot amplitude is given by

$$p_{2,0}^{(S)}(r) = -\int_r^\infty \Theta(\tilde{r}) \frac{\partial p_{1,0}^{(S)}(\tilde{r})}{\partial \tilde{r}} \, d\tilde{r}. \tag{95}$$

In agreement with results in Sec. II G 2, the corresponding velocity field, from Eqs. (93) and (68), is given by

$$\mathbf{u}_{2,0}^{(S)}(r) = \Theta(r)\mathbf{u}_{1,0}^{(S)}(r). \tag{96}$$

This is the sourcelike flow $\mathbf{u}_{1,0}^{(S)}(r)$ at leading order, modulated by the heat-spot shape. The flow $A(t)A'(t)\mathbf{u}_{2,0}^{(S)}$ at order α^2 therefore locally amplifies the leading-order sourcelike flow associated with an increasing heat-spot amplitude, $A'(t)\mathbf{u}_{1,0}^{(S)}$. Physically, heating decreases the density of the fluid locally from its reference value, so that the flow speed must increase to compensate for this, to satisfy mass conservation.

3. Pressure field

We now build on our general results and write down the pressure field for the case of the Gaussian temperature profile in Eq. (18). This is possible because, as we saw in the previous sections, much of the mathematics is shared with Sec. II G.
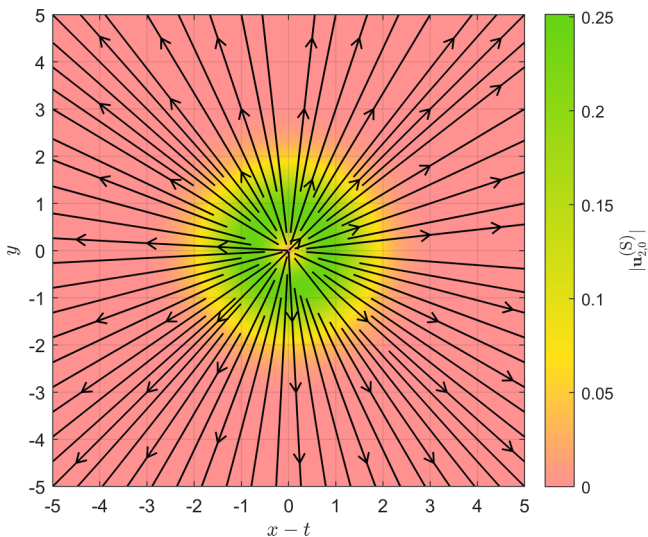
FIG. 17. Streamlines for the velocity field $\mathbf{u}_{2,0}^{(S)}(x-t, y)$ [as in Eq. (98) for the instantaneous flow at order α^2] associated with the time-variation of the heat-spot amplitude, for $-5 \leqslant x-t, y \leqslant 5$, with magnitude of the velocity field $|\mathbf{u}_{2,0}^{(S)}|$ indicated by color. The flow decays exponentially in the far field.

Recall the decomposition of the pressure $p_{2,0}$ at order α^2 into two contributions, given by Eq. (88). We already have the pressure field $p_{2,0}^{(S)}$ associated with the time-variation of the heat-spot amplitude in Eq. (95). From Eqs. (80) and (90), we can write down the pressure $p_{2,0}^{(T)}$ associated with the translation of the heat spot as

$$p_{2,0}^{(T)}(x-t, y) = (x-t)\left[\frac{1}{4r^2} + \frac{1}{2r^2}\exp(-r^2/2) - \frac{3}{4r^2}\exp(-r^2) - \frac{1}{4}E_1(r^2/2) + \frac{1}{4}E_1(r^2)\right].$$
(97)

4. Velocity field

The instantaneous flow at order α^2 may be written as

$$\mathbf{u}_{2,0}(x, y, t) = A(t)A'(t)\mathbf{u}_{2,0}^{(S)}(x-t, y) + A(t)^2\mathbf{u}_{2,0}^{(T)}(x-t, y),$$
(98)

by Eq. (92), reproduced here for convenience. By Eqs. (96) and (47), the velocity field $\mathbf{u}_{2,0}^{(S)}$ at order α^2 associated with the time-variation of the heat-spot amplitude is given by

$$\mathbf{u}_{2,0}^{(S)}(x-t, y) = \frac{(x-t)\exp(-r^2/2)[1 - \exp(-r^2/2)]}{r^2}\mathbf{e}_x + \frac{y\exp(-r^2/2)[1 - \exp(-r^2/2)]}{r^2}\mathbf{e}_y$$

$$\equiv \frac{\exp(-r^2/2)[1 - \exp(-r^2/2)]}{r}\mathbf{e}_r.$$
(99)

We plot the streamlines of this purely radial flow in Fig. 17. This is the leading-order sourcelike flow $\mathbf{u}_{1,0}^{(S)}$ modulated by the heat-spot shape function, so it decays exponentially, not algebraically, in the far field.
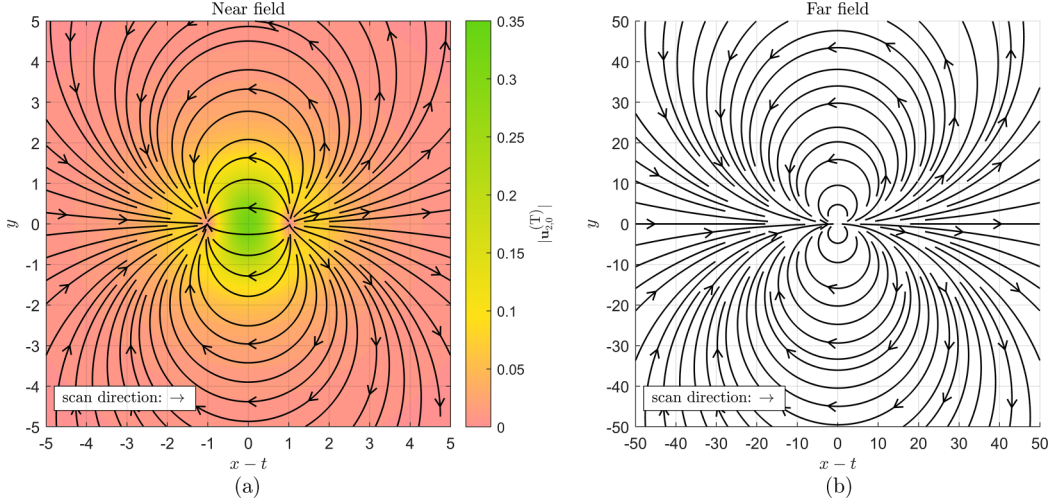
FIG. 18. Streamlines for the flow field $\mathbf{u}_{2,0}^{(T)}(x-t,y)$ [as in Eq. (92) for the instantaneous flow at order α^2] associated with translation of the heat spot in the positive x direction (scan direction). (a) Streamlines for $-5 \leqslant x-t, y \leqslant 5$, close to the heat spot (near field), with magnitude of the velocity field $|\mathbf{u}_{2,0}^{(T)}|$ indicated by color. (b) Streamlines for $-50 \leqslant x-t, y \leqslant 50$ to illustrate the far-field behavior.

By Eqs. (94) and (97), the velocity field $\mathbf{u}_{2,0}^{(T)}$ at order α^2 associated with the translation of the heat spot is given by

$$
\begin{aligned}
\mathbf{u}_{2,0}^{(T)}(x-t,y) = \mathbf{e}_x \Bigg\{ &-\frac{1}{4r^2} + \frac{(x-t)^2}{2r^4} + \left[-\frac{1}{2r^2} + \frac{(x-t)^2}{r^4} \right] \exp(-r^2/2) \\
&+ \left[\frac{3}{4r^2} - \frac{3(x-t)^2}{2r^4} - \frac{(x-t)^2}{r^2} \right] \exp(-r^2) + \frac{1}{4}\mathrm{E}_1(r^2/2) - \frac{1}{4}\mathrm{E}_1(r^2) \Bigg\} \\
+ \mathbf{e}_y \Bigg\{ &\frac{(x-t)y}{2r^4} + \frac{(x-t)y}{r^4}\exp(-r^2/2) + \left[-\frac{3(x-t)y}{2r^4} - \frac{(x-t)y}{r^2} \right] \exp(-r^2) \Bigg\}.
\end{aligned}
\tag{100}
$$

We plot in Fig. 18 the streamlines of the flow $\mathbf{u}_{2,0}^{(T)}$, with the near field illustrated in Fig. 18(a) and the far field in Fig. 18(b). The magnitude $|\mathbf{u}_{2,0}^{(T)}|$ as a function of radius r is shown in Fig. 19 on a log–log scale, along the radial lines $\theta = 0, \pi/8, \pi/4, 3\pi/8$, and $\pi/2$.

5. Far-field behaviour

The far-field behavior of the instantaneous flow $\mathbf{u}_{2,0}$ at order α^2 is given by

$$
\mathbf{u}_{2,0} \sim -\frac{1}{4}A(t)^2 \left\{ \mathbf{e}_x \left[\frac{1}{r^2} - \frac{2(x-t)^2}{r^4} \right] + \mathbf{e}_y \left[-\frac{2(x-t)y}{r^4} \right] \right\},
\tag{101}
$$

with magnitude decaying as $|\mathbf{u}_{2,0}| \sim A(t)^2/4r^2$. This is a source dipole, the same hydrodynamic singularity as at order $\alpha\beta$ but of opposite sign. It is provided solely by the contribution $A(t)^2\mathbf{u}_{2,0}^{(T)}(x-t,y)$ associated with heat-spot translation. This is because the contribution $A(t)A'(t)\mathbf{u}_{2,0}^{(S)}(x-t,y)$ associated with the time-variation of the heat-spot amplitude is highly localized to the heat spot, decaying exponentially. This is in contrast with the leading-order instantaneous flow (at order α), where the switching-on of the heat spot gives rise to the algebraic decay (source flow) that dominates in the far field.
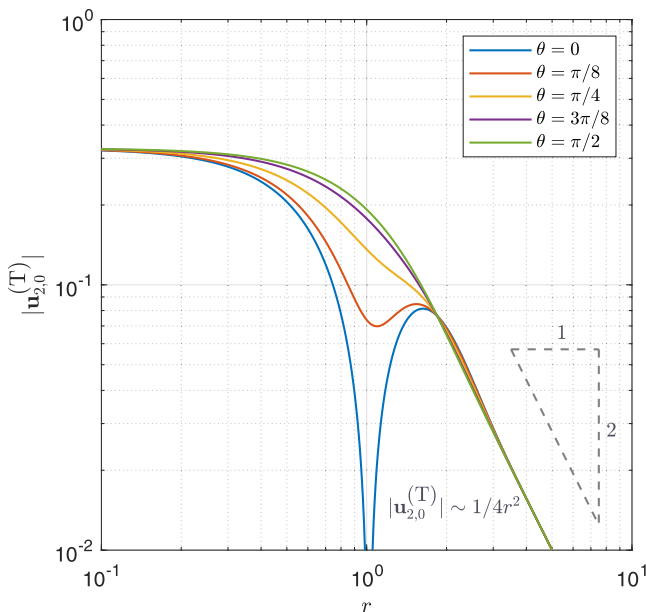
FIG. 19. Magnitude of the flow field at order α^2 associated with translation of the heat spot, $|\mathbf{u}_{2,0}^{(\mathrm{T})}|$, against the radial distance r to the center of the heat spot, plotted on a log–log scale, for $\theta = 0$, $\pi/8$, $\pi/4$, $3\pi/8$, and $\pi/2$. The far-field behavior is given by $|\mathbf{u}_{2,0}^{(\mathrm{T})}| \sim 1/4r^2$.

6. Physical mechanism

Now that we have solved analytically for the instantaneous flow at order α^2, we can interpret our results physically. We have already explained the contribution $A(t)A'(t)\mathbf{u}_{2,0}^{(\mathrm{S})}$ associated with the time-variation of the heat-spot amplitude in Sec. II H 2. The mechanism for the contribution $A(t)^2\mathbf{u}_{2,0}^{(\mathrm{T})}$ associated with heat-spot translation, which we address now, is similar to the mechanism at order $\alpha\beta$ in Sec. II G 6 but relates to density changes instead of viscosity changes, mirroring their mathematical similarities.

As discussed in Sec. II F 2 and recapped in Sec. II G 6, the instantaneous flow $A(t)\mathbf{u}_{1,0}^{(\mathrm{T})}$ at leading order (order α) associated with the translation of a heat spot is leftwards near the heat spot. The correction to the leading order captured at order α^2 is the following. Heating locally decreases the fluid density from the reference value. Therefore, to ensure that mass is conserved, the flow speed must increase locally, compensating for the fact that the density is lower than accounted for in the leading-order theory. Essentially, the potential flow at order α^2 reinforces the leading-order flow due to a heat spot.

Specifically, in the perturbation expansion, at order α, the density ρ in the term $\boldsymbol{\nabla} \cdot (\rho\mathbf{u})$ (the divergence of the mass flux) in the mass conservation equation is approximated as the reference value ρ_0. The potential flow correction at order α^2 is driven by the fact that, in the term $\boldsymbol{\nabla} \cdot (\rho\mathbf{u})$, the density ρ is slightly lower than ρ_0, due to heating. In contrast with this, at order α, thermal expansion only forces the flow via the rate of change of density $\partial\rho/\partial t$ in the mass conservation equation.

We can compare this with the mechanism at order $\alpha\beta$ (Sec. II G). In the flow at order $\alpha\beta$, a potential flow compensates for the compressibility of the leading-order flow modulated by the temperature profile. Here, instead, the flow at order α^2 is a potential flow that has the same divergence as the leading-order flow modulated by the temperature profile. The flow at order α^2 associated with heat-spot translation is a potential flow that has a source at the front of the heat spot and a sink at the back, just like the corresponding leading-order flow. It therefore
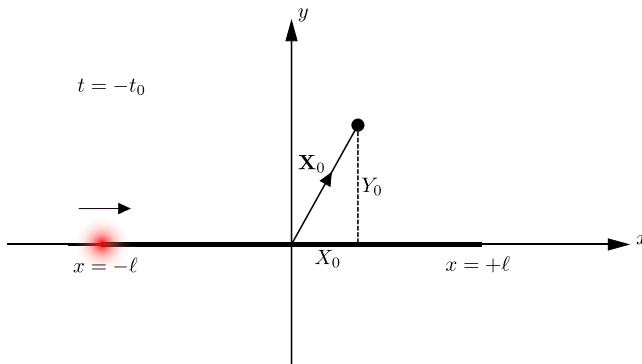
FIG. 20. Sketch of a material point initially at position $\mathbf{X}_0$ when the heat spot is at the start of the scan path $x = -\ell$ at time $t = -t_0$.

reinforces the source dipole in the far field of the leading-order flow $\mathbf{u}_{1,0}^{(\mathrm{T})}$ associated with heat-spot translation.

III. LEADING-ORDER TRAJECTORIES OF MATERIAL POINTS DURING ONE SCAN

In Sec. II, we solved for the instantaneous velocity field induced by a translating heat spot with arbitrary, time-varying amplitude, in the limit of small thermal expansion coefficient α and thermal viscosity coefficient β. This was an Eulerian perspective. In experiments, the heat spot scans repeatedly along a scan path and the resulting flow induces transport of various suspended bodies in the fluid, including proteins inside cells [28] or tracer beads in controlled experiments in a viscous fluid [30,34]. To understand this transport, we first analyze in this section the leading-order trajectories of material points during one scan, resulting from the leading-order instantaneous flow. This is a Lagrangian perspective. We show that at order α, the net displacement of any material point is exactly zero, so the leading-order net displacement, which we find in Sec. IV, occurs at higher order.

A. Equation of motion for a material point

We begin by solving for the trajectory of a material point during one scan, i.e., as the heat spot translates at dimensionless speed 1 along the scan path from $x = -\ell$ to $x = \ell$, as time progresses from $t = -t_0$ to $t = t_0$, where $t_0 = \ell$ (in dimensionless terms). Consider a material point that has initial position $\mathbf{X}_0 \equiv (X_0, Y_0)$ at time $t = -t_0$; this notation is illustrated in Fig. 20. At time t, its position vector relative to the origin is $\mathbf{X}(\mathbf{X}_0; t) \equiv (X(\mathbf{X}_0; t), Y(\mathbf{X}_0; t))$, which we write as $\mathbf{X}(t) \equiv (X(t), Y(t))$ for brevity. We aim to solve for this position vector as a function of time. In the absence of noise, the kinematics of the material point is governed by the ordinary differential equation

$$\frac{d\mathbf{X}}{dt} = \mathbf{u}(\mathbf{X}(t), t), \tag{102}$$

i.e., the material point is advected by the flow field $\mathbf{u}$ induced by the heat spot. Integrating both sides and using the initial condition, we find that the equivalent integral equation is given by

$$\mathbf{X}(t) - \mathbf{X}(-t_0) = \mathbf{X}(t) - \mathbf{X}_0 = \int_{-t_0}^{t} \mathbf{u}(\mathbf{X}(\tilde{t}), \tilde{t}) \, d\tilde{t}, \tag{103}$$

where the left-hand side is the displacement of the material point from its initial position at $t = -t_0$, when the heat spot is at the left endpoint, $x = -\ell$, of the scan path.

B. Perturbation expansion

The position vector $\mathbf{X}(t)$ appears on both sides of Eq. (103). To make further analytical progress, we pose a perturbation expansion for the displacement vector $\Delta\mathbf{X}(t) \equiv (\Delta X(t), \Delta Y(t)) \equiv \mathbf{X}(t) - \mathbf{X}_0$ as

$$\Delta\mathbf{X}(t) = \alpha\Delta\mathbf{X}_{1,0}(t) + \alpha^2\Delta\mathbf{X}_{2,0}(t) + \alpha\beta\Delta\mathbf{X}_{1,1}(t) + \text{cubic and higher-order terms}, \quad (104)$$

where $\Delta\mathbf{X}_{m,n}(t) \equiv (\Delta X_{m,n}(t), \Delta Y_{m,n}(t))$ is the displacement at order $\alpha^m\beta^n$ of the material point at time t from the position $\mathbf{X}_0$ at $t = -t_0$. Here we write $\Delta\mathbf{X}(t)$ to mean $\Delta\mathbf{X}(\mathbf{X}_0; t)$, omitting for simplicity the dependence on the initial position from the notation just as we did for the position vector $\mathbf{X}(t)$. In the above, we anticipate that the displacement will inherit the structure of the velocity field perturbation expansion, since displacement is the time-integral of velocity.

Using this, we may also expand the velocity field at the position $\mathbf{X}(t)$ of the material point, about the initial position $\mathbf{X}_0$, as

$$\begin{aligned}
\mathbf{u}(\mathbf{X}(t), t) = {}& \mathbf{u}(\mathbf{X}_0 + \alpha\Delta\mathbf{X}_{1,0}(t) + \text{h.o.t.}, t) \\
= {}& \alpha\mathbf{u}_{1,0}(\mathbf{X}_0 + \alpha\Delta\mathbf{X}_{1,0}(t) + \text{h.o.t.}, t) \\
& + \alpha^2\mathbf{u}_{2,0}(\mathbf{X}_0 + O(\alpha), t) + \alpha\beta\mathbf{u}_{1,1}(\mathbf{X}_0 + O(\alpha), t) + \text{cubic and higher-order terms} \\
= {}& \alpha\mathbf{u}_{1,0}(\mathbf{X}_0, t) + \alpha^2[\mathbf{u}_{2,0}(\mathbf{X}_0, t) + \Delta\mathbf{X}_{1,0}(t) \cdot \nabla\mathbf{u}_{1,0}(\mathbf{X}_0, t)] \\
& + \alpha\beta\mathbf{u}_{1,1}(\mathbf{X}_0, t) + \text{cubic and higher-order terms.}
\end{aligned} \quad (105)$$

Substituting this into Eq. (103), we obtain

$$\begin{aligned}
& \alpha\Delta\mathbf{X}_{1,0}(t) + \alpha^2\Delta\mathbf{X}_{2,0}(t) + \alpha\beta\Delta\mathbf{X}_{1,1}(t) + \text{cubic and higher-order terms} \\
& = \alpha\int_{-t_0}^t \mathbf{u}_{1,0}(\mathbf{X}_0, \tilde{t})\, d\tilde{t} + \alpha^2\int_{-t_0}^t [\mathbf{u}_{2,0}(\mathbf{X}_0, \tilde{t}) + \Delta\mathbf{X}_{1,0}(\tilde{t}) \cdot \nabla\mathbf{u}_{1,0}(\mathbf{X}_0, \tilde{t})]\, d\tilde{t} \\
& \quad + \alpha\beta\int_{-t_0}^t \mathbf{u}_{1,1}(\mathbf{X}_0, \tilde{t})\, d\tilde{t}.
\end{aligned} \quad (106)$$

We observe that at order α (leading order) and at order $\alpha\beta$, this displacement is simply the integral over time of the velocity field evaluated at the initial position of the material point. In contrast with this, at order α^2, there is an additional contribution, associated with the order-α displacement of the material point.

C. Order α

From Eq. (106), the displacement $\Delta\mathbf{X}_{1,0}(t)$ at order α of a material point is given by

$$\Delta\mathbf{X}_{1,0}(t) = \int_{-t_0}^t \mathbf{u}_{1,0}(\mathbf{X}_0, \tilde{t})\, d\tilde{t}, \quad (107)$$

where we recall that $\mathbf{u}_{1,0}$ is the instantaneous velocity field at order α. During one scan, the displacement $\Delta\mathbf{X}_{1,0}(t)$ at order α typically gives the leading-order displacement of a material point at time t. (In Sec. III D, we show that one full scan of a heat spot results in zero net displacement of the material point at order α.) To evaluate the integral in Eq. (107), recall from Eq. (35) that the velocity field $\mathbf{u}_{1,0}$ at order α is an exact time-derivative of a function proportional to the heat-spot amplitude, for the general heat spot in Eq. (30). Therefore, for a general heat spot, Eq. (107) becomes

$$\Delta\mathbf{X}_{1,0}(t) = \int_{-t_0}^t \frac{\partial}{\partial\tilde{t}}\big[A(\tilde{t})\mathbf{u}_{1,0}^{(S)}(X_0 - \tilde{t}, Y_0)\big]\, d\tilde{t} = A(t)\mathbf{u}_{1,0}^{(S)}(X_0 - t, Y_0) - A(-t_0)\mathbf{u}_{1,0}^{(S)}(X_0 + t_0, Y_0), \quad (108)$$

by the Fundamental Theorem of Calculus. If the scan path is finite as in experiments, then the heat-spot amplitude is zero at the ends of the scan path by definition, so the second term vanishes

$[A(-t_0) = 0]$. For an infinite scan path ($t_0 \to \infty$) as in related theoretical work [30], the second term vanishes regardless of the heat-spot amplitude because the velocity field $\mathbf{u}_{1,0}^{(S)}$ decays at infinity. In either case, the displacement at order α during one scan simplifies to

$$\Delta \mathbf{X}_{1,0}(t) = A(t) \mathbf{u}_{1,0}^{(S)}(X_0 - t, Y_0). \tag{109}$$

For the Gaussian heat spot [Eq. (18)], the relevant velocity field $\mathbf{u}_{1,0}^{(S)}$ is given by Eq. (47). The displacement of a material point $\Delta \mathbf{X}_{1,0}(t)$ at order α during one scan is therefore given by

$$\Delta \mathbf{X}_{1,0}(t) = A(t) \left\{ \frac{(x-t)[1 - \exp(-r^2/2)]}{r^2} \mathbf{e}_x + \frac{y[1 - \exp(-r^2/2)]}{r^2} \mathbf{e}_y \right\} \Bigg|_{\mathbf{X}_0}$$
$$\equiv A(t) \left[\frac{1 - \exp(-r^2/2)}{r} \mathbf{e}_r \right] \Bigg|_{\mathbf{X}_0}, \tag{110}$$

where we recall that the radius r and radial unit vector $\mathbf{e}_r$ are measured from the center of the (translating) heat spot.

1. Sinusoidal heat-spot amplitude and finite scan path

We illustrate in Fig. 21 the trajectories of material points during one scan. We choose the sinusoidal amplitude function from Eq. (55) and we choose the length of the scan path to be $2\ell = 2t_0 = 2.75$ to match experiments [34]. In Fig. 21, the initial positions of the material points are $\mathbf{X}_0 = (0, 0), (0,0.5), (0,1), (0,2), (0,3)$, and $(0,5)$. These lie on the y axis for simplicity. We plot the x component $\Delta X_{1,0}(t)$ of displacement and y component $\Delta Y_{1,0}(t)$ at order α as a function of time in Figs. 21(a) and 21(b), respectively. We plot in Fig. 21(c) the corresponding trajectories in space, $(\Delta X_{1,0}(t), \Delta Y_{1,0}(t))$ for $t = -t_0$ to $t = t_0$. These trajectories are "petal-shaped." [As an aside, if we instead have a constant-amplitude heat spot translating along an infinitely long scan path, then it can be shown analytically that the trajectory of a material point far from the x axis ($Y_0 \gg 1$) is a circle, due to the translating source-dipole flow far from the heat spot. The diameter of this circular trajectory scales as $1/Y_0$.] At order α, each material point in Fig. 21 appears to return precisely to its initial position after one full scan of the heat spot; we show in the following sections that this is a general result for all material points, not only those on the y axis.

D. Zero net displacement at order α for general heat spot

The result in Eq. (109) gives the displacement at order α of a material point at time t that has position $\mathbf{X}_0$ when the heat spot is at the start of the scan path ($t = -t_0$). We illustrated in the previous section examples of leading-order trajectories of material points during one scan and saw that material points return to their initial position after one full scan, correct to order α. Previous theoretical work [29] for a traveling temperature wave showed that this net displacement of a material point is zero at order α for material points on the scan path. Here, we extend the result that the net displacement is zero at order α to material points with any initial position, for a general heat spot.

Importantly, note that Eq. (109) is valid for the general heat spot in Eq. (30), with arbitrary amplitude function $A(t)$ and arbitrary shape specified by the function $\Theta(x - t, y)$. In this section, we show that for this general heat spot, the net displacement $\Delta \mathbf{X}_{1,0}(t_0)$ of any material point (i.e., the displacement due to one full scan of the heat spot) is exactly zero at order α, for finite and for infinite scan paths. Consequently, net displacements and hence trajectories of material points due to repeated scanning of the heat spot (Sec. IV) are due to quadratic effects, not linear. This is key for understanding experimentally observed trajectories of tracers [34] (Sec. V).
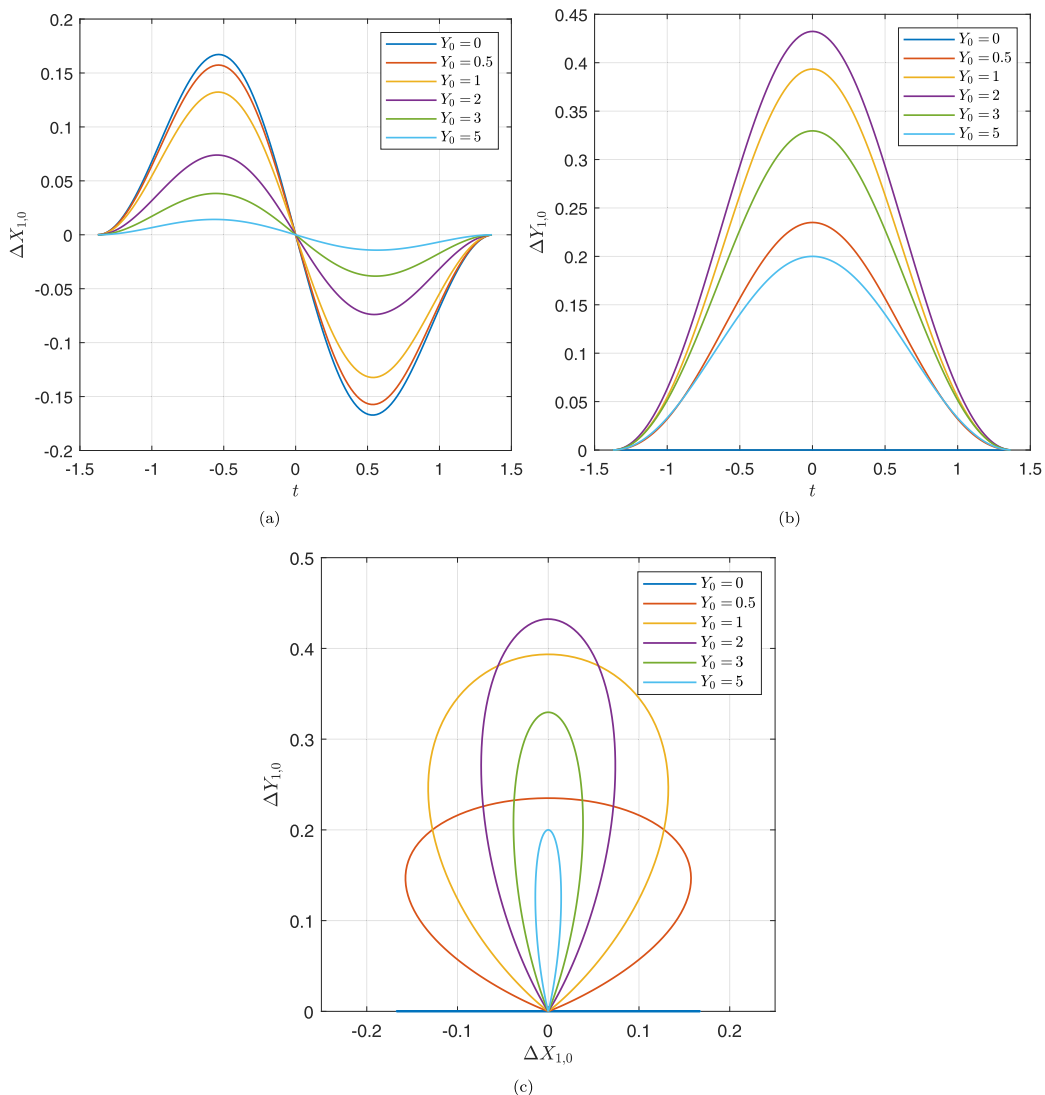
FIG. 21. Trajectories of material points during one scan at leading order, i.e., order α. The material points start at position $(0, Y_0)$, on the y axis, at time $t = -t_0$ when the heat spot begins the scan from $x = -\ell$, for selected values $Y_0 = 0, 0.5, 1, 2, 3$, and 5. (a) Plot of the x component $\Delta X_{1,0}$ of the displacement of the material point at order α as a function of time t, during one scan, i.e., $-t_0 \leqslant t \leqslant t_0$. (b) Same as panel (a) but for the y component $\Delta Y_{1,0}$ of the displacement of the material point at order α. (c) Plot of the same trajectories in the $(\Delta X_{1,0}, \Delta Y_{1,0})$ plane. The length of the scan path is chosen to be $2\ell \equiv 2t_0 = 2.75$, to match microfluidic experiments [34].

1. Finite scan path

First we consider a finite scan path. This is the relevant case for both biological (FLUCS) experiments [28] and microfluidic experiments [34]. By definition of a finite scan path, the amplitude of the heat spot is zero at the ends of the scan path, so we have $A(t_0) = 0$. By Eq. (109), the net displacement $\Delta \mathbf{X}_{1,0}(t_0)$ at order α, of any material point, is therefore given by

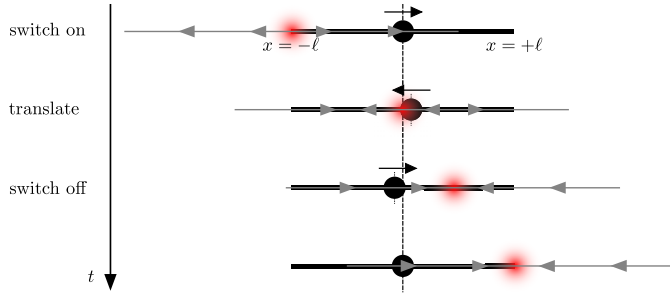$$\Delta \mathbf{X}_{1,0}(t_0) = \mathbf{0}, \tag{111}$$

FIG. 22. Cartoon summary of zero net displacement at order α of a material point, depicted as a black circle. A heat spot translating along a scan path from $x = -\ell$ to $x = \ell$ induces a velocity field experienced by the material point initially at position vector $\mathbf{X}_0$. (Here, the material point starts at the midpoint of the scan path, $\mathbf{X}_0 = \mathbf{0}$.) This results in a small displacement of the material point at time t. The rightward displacement of the material point due to the switching-on and switching-off of the heat spot at the ends of the scan path is canceled out by the leftward displacement due to the translation of the heat spot, correct to order α.

as claimed. Mathematically, this net displacement is zero because the velocity field at order α is an exact time-derivative of a function proportional to the heat-spot amplitude [Eq. (35)] and because the net displacement of a material point is the time-integrated fluid velocity evaluated at the initial position, at this order. The contribution to the net displacement due to the time-variation of the heat-spot amplitude [related to the velocity field contribution $A'(t)\mathbf{u}_{1,0}^{(S)}(x - t, y)$] precisely cancels that due to the translation of the heat spot [related to $A(t)\mathbf{u}_{1,0}^{(T)}(x - t, y)$], at order α. This demonstration generalizes earlier ideas [29] for the case of temperature profiles steady in the comoving frame.

The net displacement of any material point (due to a full scan of the heat spot) is thus always zero at order α. This holds for any heat-spot shape and amplitude function, not only for the idealized Gaussian profile we imposed to find explicit analytical solutions. In experiments, the heat spot may become elongated if its speed is sufficiently high, losing the circular symmetry it has for lower speeds. Crucially, symmetry of the heat spot is not necessary for the net displacement to be zero at order α, according to our theoretical model. Importantly, this means that the leading-order net displacement therefore scales at least quadratically, not linearly, with the heat-spot amplitude. This is consistent with experiments [28,30] in which a quadratic scaling with the temperature perturbation was measured.

To explain the trajectories of tracers in Fig. 21(c) in terms of the leading-order instantaneous flow (Fig. 10), we illustrate the displacement of a material point due to the heat spot during one scan in Fig. 22. For simplicity, the cartoon in Fig. 22 shows the special case where the material point starts at the midpoint of the scan path; it remains on the x axis for all time by symmetry. As the heat spot switches on, the resulting sourcelike flow pushes the material point at the origin rightwards, by a small (order-α) distance. Then, the flow induced by the translation of the heat spot overall pushes the material point leftwards. This is because the material point is near the heat spot, where the flow is more leftward than in the far field. Finally, the sinklike flow produced when the heat spot switches off at the end of the scan path pulls the material point rightwards, back to its initial position, correct to order α.

To provide intuition on the net displacement of material points in the far field, we observe that the far-field instantaneous flow induced by translation of a constant-amplitude heat spot is a source dipole. The average velocity of material points far from the scan path inherits the far-field source dipole from this flow at order α, corresponding to a source on the right and a sink on the left (for rightward translation). Over the course of a scan, this effect is precisely canceled out by the switching-on of the heat spot at the start of the scan path and the switching-off at the end of the scan path. For a finite scan path, the fact that the heat-spot amplitude varies with time is thus essential in
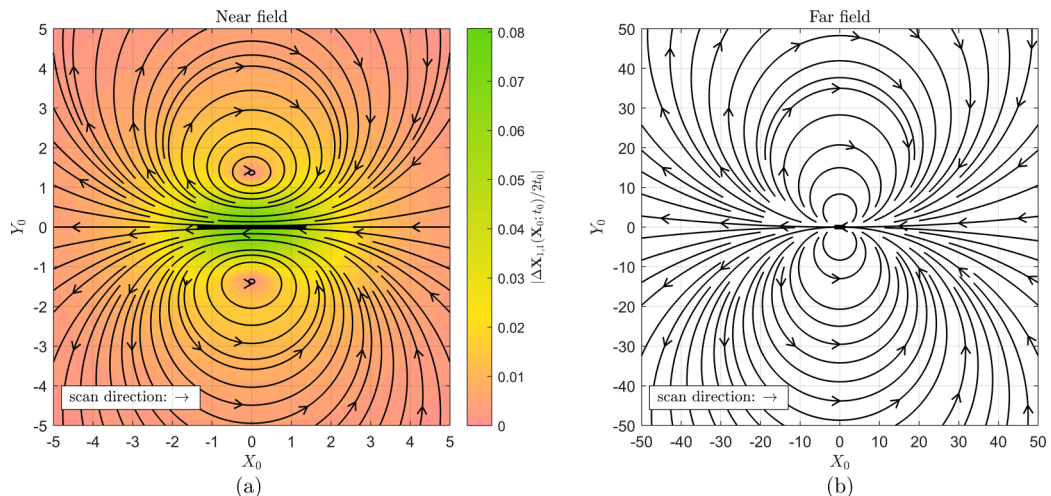
FIG. 23. Streamlines for the average velocity of a material point at order $\alpha\beta$ over a scan period, $\Delta\mathbf{X}_{1,1}(\mathbf{X}_0; t_0)/2t_0$. The heat spot translates in the positive x direction (scan direction). The scan path is indicated with a thick black line segment. (a) Streamlines for $-5 \leqslant X_0, Y_0 \leqslant 5$, close to the scan path (near field), with magnitude of the average velocity of material points $|\Delta\mathbf{X}_{1,1}(\mathbf{X}_0; t_0)/2t_0|$ indicated by color. (b) Streamlines for $-50 \leqslant X_0, Y_0 \leqslant 50$, which illustrate the far-field behavior.

our theory. Over one scan, the switching-on and switching-off give rise to a source dipole in the far field of the average velocity of tracers (average Lagrangian velocity), corresponding to a source on the left and a sink on the right at order α, i.e., the opposite of that due to translation of the heat spot.

2. Infinite scan path

To compare our theory with previous studies [29,30], we consider here the special case of the net displacement at order α of a material point, for an infinite scan path ($t_0 \to \infty$). In that case, the heat-spot amplitude $A(t)$ does not necessarily decay as $t \to \pm\infty$, e.g., $A(t) = $ const. However, for a temperature profile that decays at infinity, the velocity field $\mathbf{u}_{1,0}^{(S)}$ does decay at infinity. Using this and Eq. (109), for an infinite scan path, the net displacement $\Delta\mathbf{X}_{1,0}(\infty)$ at order α of any material point is given by

$$\Delta\mathbf{X}_{1,0}(\infty) = \mathbf{0}. \tag{112}$$

In particular, this holds for the case of constant amplitude $A(t) = A$, considered in earlier work [30]. The material point experiences the velocity field $\alpha A \mathbf{u}_{1,0}^{(T)}(x - t, y)$ and so moves rightwards by an order α displacement, then leftwards, and finally rightwards, back to its initial position (correct to order α).

IV. LEADING-ORDER NET DISPLACEMENT OF MATERIAL POINTS DUE TO ONE SCAN

We saw in Sec. III D that at linear order, the net displacement (due to one full scan of the heat spot) of a material point with any initial position is zero, for a heat spot with arbitrary time-dependent amplitude and arbitrary shape. We therefore expect the leading-order net displacement to be quadratic in the heat-spot amplitude, consistent with experiments [30]. The model of Ref. [30] used a constant-amplitude heat spot and examined net displacement of material points on an infinite scan path. Here we discuss the leading-order net displacement of material points at any position in the fluid, for a heat spot with arbitrary amplitude and for a scan path of arbitrary length. In particular, we illustrate in Figs. 23 and 25 the velocity of tracers averaged over one scan,

for a sinusoidal amplitude function, at order $\alpha\beta$ and order α^2, respectively. We will then apply this in Sec. V to recent experimental results on the trajectories and average velocity of tracers due to repeated scanning of the heat spot [34].

A. Net displacement at order $\alpha\beta$

Mathematically, the leading-order net displacement could be a linear combination of net displacements at order α^2, order $\alpha\beta$, and order β^2. However, we can eliminate order β^2, as the instantaneous flow at order β^2 is zero (Sec. II E). Hence, we now consider the net displacement at order $\alpha\beta$; we discuss the contribution at order α^2 in the next section.

By Eq. (106), the net displacement $\Delta\mathbf{X}_{1,1}(t_0)$ at order $\alpha\beta$ of a material point with any initial position $\mathbf{X}_0$ is given by

$$\Delta\mathbf{X}_{1,1}(t_0) = \int_{-t_0}^{t_0} \mathbf{u}_{1,1}(\mathbf{X}_0, t)\, dt, \tag{113}$$

where $\mathbf{u}_{1,1}$ is the instantaneous velocity field at order $\alpha\beta$. As at order α, this is simply the integral of the velocity field evaluated at the initial position of the material point, which approximates the true position of the material point. For a Gaussian heat spot, the velocity field $\mathbf{u}_{1,1}$ at order $\alpha\beta$ is given explicitly by Eqs. (81) and (82).

1. Sinusoidal heat-spot amplitude and finite scan path

The net displacement in Eq. (113) may then be evaluated numerically once we choose an amplitude function $A(t)$. To illustrate how the net displacement varies with initial position of the material point, we consider here a sinusoidal heat-spot amplitude function [Eq. (55) as before] and a finite scan path, which is the relevant setup for FLUCS experiments [28]. We plot the streamlines of the velocity $\Delta\mathbf{X}_{1,1}(\mathbf{X}_0; t_0)/2t_0$ of material points at order $\alpha\beta$, averaged over one scan period, in Fig. 23, with the near field in Fig. 23(a) and the far field in Fig. 23(b). To quantify spatial variation, we plot the magnitude of this average Lagrangian velocity, $|\Delta\mathbf{X}_{1,1}(\mathbf{X}_0; t_0)/2t_0|$, at order $\alpha\beta$ as a function of the initial distance $|\mathbf{X}_0|$ of the material point from the midpoint of the scan path, in Fig. 24. For this log–log plot, we write the initial position of the material point as $\mathbf{X}_0 = |\mathbf{X}_0|(\cos\phi, \sin\phi)$, i.e., using polar coordinates with origin at the midpoint of the scan path.

2. Far-field for general heat-spot amplitude and finite scan path

Recall from Eq. (84) that in the far field, the instantaneous flow $\mathbf{u}_{1,1}$ at order $\alpha\beta$ is a hydrodynamic source dipole. Specifically, this applies many heat-spot radii away from the center of the translating heat spot, $r \gg 1$. Substituting this into Eq. (113), the net displacement of a material point that remains many heat-spot radii from the heat spot throughout a scan is given by

$$\Delta\mathbf{X}_{1,1}(\mathbf{X}_0; t_0) \sim \frac{1}{4} \int_{-t_0}^{t_0} A(t)^2 \left\{ \mathbf{e}_x \left[\frac{1}{r^2} - \frac{2(x-t)^2}{r^4} \right] + \mathbf{e}_y \left[-\frac{2(x-t)y}{r^4} \right] \right\} \Bigg|_{\mathbf{X}_0} dt, \tag{114}$$

where we recall that $r^2 = (x-t)^2 + y^2$.

If, in addition to this, the material point is many scan-path lengths away from the heat spot (at all times), i.e., $r \gg \ell$, then we can also approximate the spatially varying factor in the integrand as its value at $t = 0$, to leading order. This gives

$$\Delta\mathbf{X}_{1,1}(\mathbf{X}_0; t_0) \sim \frac{1}{4} \int_{-t_0}^{t_0} A(t)^2\, dt \left[\mathbf{e}_x \left(\frac{1}{|\mathbf{X}_0|^2} - \frac{2X_0^2}{|\mathbf{X}_0|^4} \right) + \mathbf{e}_y \left(-\frac{2X_0 Y_0}{|\mathbf{X}_0|^4} \right) \right]. \tag{115}$$
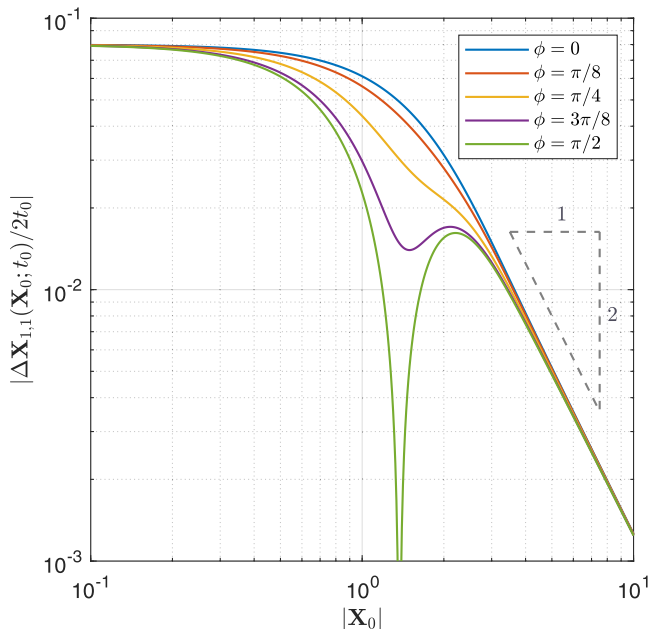
FIG. 24. Magnitude of the average Lagrangian velocity $|\Delta\mathbf{X}_{1,1}(\mathbf{X}_0;t_0)/2t_0|$ at order $\alpha\beta$ of material points against the distance $|\mathbf{X}_0|$, plotted on a log–log scale, for $\phi = 0$, $\pi/8$, $\pi/4$, $3\pi/8$, and $\pi/2$. Here, the initial position of a material point is written as $\mathbf{X}_0 = |\mathbf{X}_0|(\cos\phi, \sin\phi)$, i.e., in polar coordinates with origin at the midpoint of the scan path. In the far field, the magnitude $|\Delta\mathbf{X}_{1,1}(\mathbf{X}_0;t_0)/2t_0|$ follows an inverse square law $\sim 1/|\mathbf{X}_0|^2$.

Correspondingly, the velocity $\Delta\mathbf{X}_{1,1}(\mathbf{X}_0;t_0)/2t_0$ of the material point initially at $\mathbf{X}_0$, averaged over one scan, is given by

$$\frac{\Delta\mathbf{X}_{1,1}(\mathbf{X}_0;t_0)}{2t_0} \sim \frac{1}{8t_0} \int_{-t_0}^{t_0} A(t)^2 \, dt \left[\mathbf{e}_x\left(\frac{1}{|\mathbf{X}_0|^2} - \frac{2X_0^2}{|\mathbf{X}_0|^4} \right) + \mathbf{e}_y\left(-\frac{2X_0Y_0}{|\mathbf{X}_0|^4} \right) \right], \qquad (116)$$

if the material point is far from the scan path, i.e., both many heat-spot radii and many scan-path lengths away. We note that this is only possible for scan paths of finite length. This far-field average Lagrangian velocity field is a source dipole, with strength proportional to the time-average of the square of the heat-spot amplitude. The direction of circulation corresponds to a source on the left and a sink on the right, inherited from the instantaneous flow at order $\alpha\beta$ (see Sec. II G 6).

3. Net displacement of material points on the x axis for general heat-spot amplitude and general scan path length

We now examine the net displacement, or equivalently the average velocity, of material points on the x axis. For a Gaussian heat spot, the instantaneous velocity field $\mathbf{u}_{1,1}$ [Eq. (82), Figs. 12, and 13] is in the negative x direction everywhere on the x axis, i.e., in the opposite direction to the translation of the heat spot. As explained in Sec. II G 6, this is because of localized amplification of the leading-order flow due to heat-spot translation in the near field and a source-dipole flow enforcing incompressibility in the far field. Consequently, the net displacement in Eq. (113) is also in the negative x direction for any material point on the x axis and there is strong leftward transport near the scan path. This is illustrated for a sinusoidal amplitude function in Figs. 23 and 24.

4. Constant heat-spot amplitude and infinite scan path

Recall that earlier theoretical work [30] focused on the net displacement of material points lying on an infinite scan path, for a constant-amplitude heat spot. To begin comparing our mathematical model with this, we therefore first substitute the heat-spot amplitude $A(t) = A = \text{const}$ and take the limit of infinite scan-path length ($t_0 \to \infty$), but still allow the material point to have arbitrary initial position $\mathbf{X}_0$ (i.e., Y_0 is not necessarily zero). For this special case, the net displacement at order $\alpha\beta$ [Eq. (113)] may be evaluated analytically as

$$\Delta\mathbf{X}_{1,1}(\infty) = -A^2\mathbf{e}_x\{\sqrt{\pi}[\sqrt{2}\exp(-Y_0^2/2) - \exp(-Y_0^2)] - \pi Y_0[\text{erf}(Y_0) - \text{erf}(Y_0/\sqrt{2})]\}. \tag{117}$$

The above result [Eq. (117)] allows us to make important physical observations. First, the net displacement at order $\alpha\beta$ is in the negative x direction for all Y_0, i.e., for all material points, not only for material points on the scan path. This holds both for a heat spot ($A > 0$) and for a cool spot ($A < 0$), since the net displacement is quadratic in the heat-spot amplitude. There is no net displacement in the y direction, by symmetry of the instantaneous flow. Second, the net displacement at order $\alpha\beta$ is independent of X_0 (the horizontal component of the initial position of the material point). This is unsurprising, since all x are indistinguishable when the scan path is infinite.

Third, we observe that the net displacement at order $\alpha\beta$ arises purely from the amplification of the leading-order instantaneous flow, not from the potential flow at order $\alpha\beta$. Recall that the instantaneous flow at order $\alpha\beta$ is a sum of a potential flow $-\nabla p_{1,1}$ and the leading-order flow modulated by the temperature profile $\Delta T \mathbf{u}_{1,0}$ [Eq. (62)]. Since we are considering here the case where the time-derivative of the amplitude is zero, there is no contribution to either of these terms from the switching-on or switching-off of the heat spot, only from the translation of the heat spot. The instantaneous flow is therefore steady in the comoving frame. As a result, the x component of the potential flow is the exact time-derivative of the pressure (the potential), which decays at infinity. The integral of the potential flow over time is therefore zero; that is, the potential flow contributes no net displacement. A similar result holds for material points on the scan path of a traveling wave temperature profile [29], which has periodic boundary conditions in the x direction instead of decay.

Instead, the nonzero net displacement of the material point arises from the amplified leading-order velocity contribution $\Delta T \mathbf{u}_{1,0}$ in Eq. (62), not only for the Gaussian but for any temperature profile decaying at infinity. We recall from earlier discussion, summarized in Fig. 15, that this contribution is the intuitive effect of the heat spot, amplifying the leftward leading-order flow in the heat spot by decreasing the viscosity there, as described in Ref. [30]. This then results in net leftward displacement of the material point.

Therefore, we now see that each of the two terms in the instantaneous velocity field at order $\alpha\beta$, $\mathbf{u}_{1,1} = -\nabla p_{1,1} + \Delta T \mathbf{u}_{1,0}$, is responsible for a key physical feature. The potential flow, $-\nabla p_{1,1}$, is solely responsible for the hydrodynamic source dipole in the far field of the average Lagrangian velocity $\Delta\mathbf{X}_{1,1}(\mathbf{X}_0; t_0)/2t_0$, inherited from $\mathbf{u}_{1,1}$ (explained in Sec. II G). However, the amplified leading-order flow, $\Delta T \mathbf{u}_{1,0}$, is solely responsible for the leftwards leading-order net displacement of a material point for an infinitely long scan path, occurring at order $\alpha\beta$.

5. Comparison with earlier theoretical work

We can now compare our results so far on net displacement with earlier work [30]. The authors of Ref. [30] found that the net displacement of a material point on the infinitely long scan path, for a Gaussian heat spot with constant amplitude, is given by

$$\Delta\mathbf{X}(\mathbf{0}; \infty)_{[30]} = -\tfrac{1}{2}\sqrt{\pi}\alpha\beta\Delta T_0^2 A^2 a\mathbf{e}_x, \tag{118}$$

where we have converted to the notation of our theory (including using the z-averaged velocity instead of the midplane velocity). In our work, we found in Sec. III D that the net displacement at order α is zero, in agreement with Eq. (118). We also showed in Sec. II E that at order β^2 there is no instantaneous flow, so there is also no net displacement at this order. For water (used

in Ref. [30]), the value of the thermal expansion coefficient α is much smaller than the thermal viscosity coefficient β; the contribution to net displacement at order α^2 in our theory may therefore be neglected in favour of order $\alpha\beta$. Hence, within our perturbation-expansion framework, we have shown systematically that the leading-order net displacement of the material point occurs at order $\alpha\beta$, in agreement with Ref. [30] and Eq. (118).

We substitute the initial position $\mathbf{X}_0 = \mathbf{0}$ into Eq. (117), which we recall came from integrating our analytical expression for the instantaneous flow field. Our systematic theoretical approach therefore predicts the dimensional, leading-order net displacement of this material point to be

$$\Delta \mathbf{X}(\mathbf{0}; \infty) = -\sqrt{\pi}(\sqrt{2} - 1)\alpha\beta \Delta T_0^2 A^2 a \mathbf{e}_x + O(\alpha^2) + \text{cubic and higher-order terms.} \qquad (119)$$

This is quadratic in the peak temperature change $\Delta T_0 A$ and is always in the negative x direction, i.e., in the opposite direction to translation of the heat spot. Comparing Eq. (119) with Eq. (118), we see that our rigorous perturbation calculation results in an improved numerical factor ($\sqrt{2} - 1 \approx 0.41$ versus $1/2 = 0.5$); however, all scalings are in agreement.

B. Net displacement at order α^2

We now consider the net displacement at order α^2 of a material point. This depends only on thermal expansion, so would exist even if the fluid viscosity were constant. By Eq. (106), the net displacement $\Delta \mathbf{X}_{2,0}(t_0)$ at order α^2 is given by

$$\Delta \mathbf{X}_{2,0}(t_0) = \int_{-t_0}^{t_0} [\mathbf{u}_{2,0}(\mathbf{X}_0, t) + \Delta \mathbf{X}_{1,0}(t) \cdot \nabla \mathbf{u}_{1,0}(\mathbf{X}_0, t)] \, dt, \qquad (120)$$

where we recall that $\mathbf{u}_{2,0}$ is the instantaneous velocity field at order α^2 [Eqs. (98)–(100)], $\Delta \mathbf{X}_{1,0}(t)$ is the displacement at order α at time t of the material point [Eq. (110)], $\mathbf{u}_{1,0}$ is the instantaneous velocity field at order α [Eqs. (46)–(48)], and $\mathbf{X}_0$ is the position of the material point when the heat spot is at the start of the scan path ($t = -t_0$). The equation numbers correspond to our analytical results for the Gaussian heat spot.

We observe that there are two contributions to this due to the Taylor expansion in Eq. (106). The first is the integral of the velocity field at order α^2 evaluated at the initial position of the material point. This is similar to the net displacements at order α and order $\alpha\beta$. However, in contrast with order α and order $\alpha\beta$, there is a second contribution. This arises from the order-α displacement at time t of the material point from its initial position, when the material point is experiencing the order-α instantaneous flow induced by the heat spot.

1. Sinusoidal heat-spot amplitude and finite scan path

Here we illustrate how the velocity of material points at order α^2 averaged over one scan varies spatially, for the sinusoidal heat-spot amplitude function given by Eq. (55). We plot in Fig. 25 the streamlines of the average Lagrangian velocity $\Delta \mathbf{X}_{2,0}(\mathbf{X}_0; t_0)/2t_0$ at order α^2, with the near field in Fig. 25(a) and the far field in Fig. 25(b). In Fig. 26, we plot on a log–log scale the magnitude of the average Lagrangian velocity, $|\Delta \mathbf{X}_{2,0}(\mathbf{X}_0; t_0)/2t_0|$, at order α^2 as a function of the initial distance $|\mathbf{X}_0|$ of the material point from the midpoint of the scan path. As before, we write the initial position of the material point as $\mathbf{X}_0 = |\mathbf{X}_0|(\cos \phi, \sin \phi)$.

We observe that the streamlines of the average Lagrangian velocity field at order α^2 (Fig. 25) are qualitatively similar to those at order $\alpha\beta$ (Fig. 23), except the direction of circulation is reversed: at order α^2, near the scan path, the material points have average velocity in the same direction as the translation of the heat spot (rightwards), whereas far from the x axis, the net transport of tracers is instead leftwards and decays in strength. Thus, even if viscosity were constant ($\beta = 0$), we would predict order-α^2 net transport of tracers that varies spatially in a similar way to the net transport due to the interplay between thermal viscosity changes and thermal expansion, but with the opposite direction of circulation.
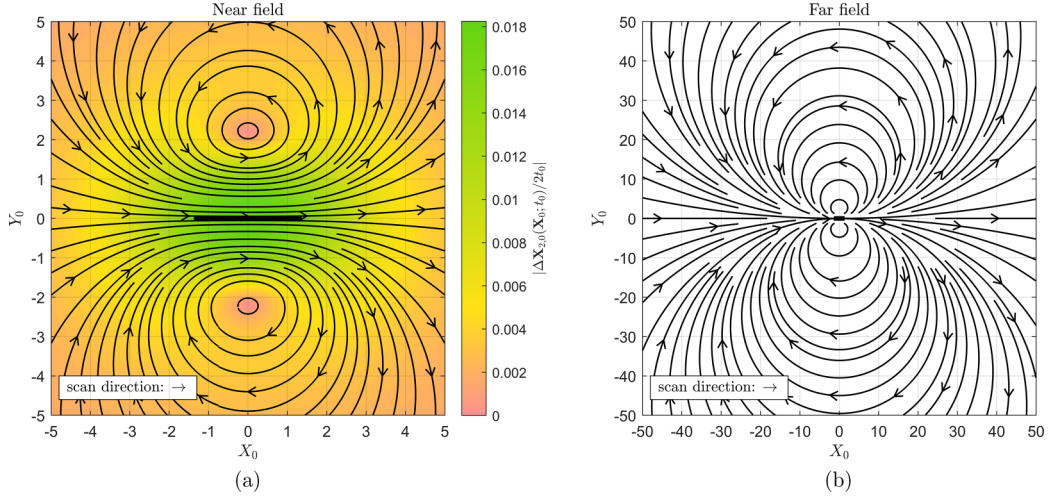
FIG. 25. Streamlines for the average velocity of a material point at order α^2 over a scan period, $\Delta\mathbf{X}_{2,0}(\mathbf{X}_0; t_0)/2t_0$. The heat spot translates in the positive x direction (scan direction). The scan path is indicated with a thick black line segment. (a) Streamlines for $-5 \leqslant X_0, Y_0 \leqslant 5$, close to the scan path, with magnitude of the average velocity of material points $|\Delta\mathbf{X}_{2,0}(\mathbf{X}_0; t_0)/2t_0|$ indicated by color. (b) Streamlines for $-50 \leqslant X_0, Y_0 \leqslant 50$ to indicate far-field behavior.
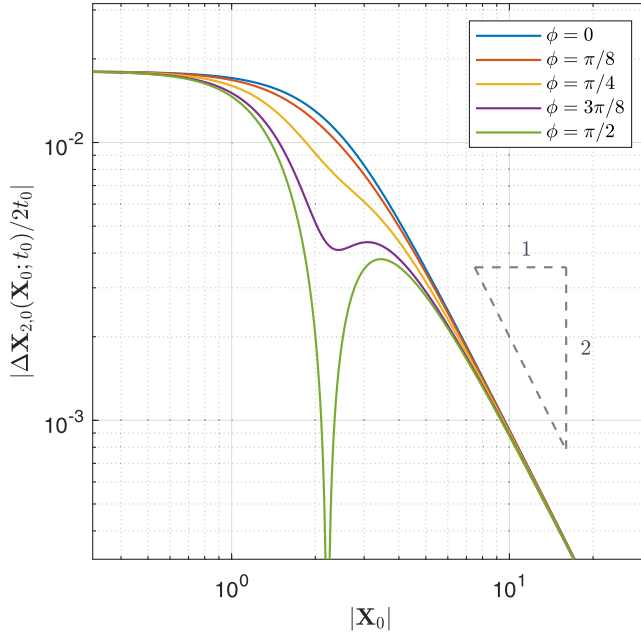

FIG. 26. Magnitude of the average velocity $|\Delta\mathbf{X}_{2,0}(\mathbf{X}_0; t_0)/2t_0|$ at order α^2 of material points against the distance $|\mathbf{X}_0|$, plotted on a log–log scale, for $\phi = 0$, $\pi/8$, $\pi/4$, $3\pi/8$, and $\pi/2$. As at order $\alpha\beta$, the initial position of a material point is written as $\mathbf{X}_0 = |\mathbf{X}_0|(\cos\phi, \sin\phi)$, i.e., in polar coordinates with origin at the midpoint of the scan path. In the far field, the magnitude $|\Delta\mathbf{X}_{2,0}(\mathbf{X}_0; t_0)/2t_0|$ follows an inverse square law $\sim 1/|\mathbf{X}_0|^2$.

2. Far-field behavior for general heat-spot amplitude and finite scan path

For a Gaussian heat spot with arbitrary amplitude, we may find the far-field velocity of material points at order α^2 averaged over one scan. First we note how terms in the integrand in Eq. (120) scale with distance r from the center of the heat spot, in the limit $r \gg 1$ (many heat-spot radii away). The instantaneous flow $\mathbf{u}_{2,0}$ at order α^2 is a hydrodynamic source dipole in the far field [Eq. (101)], scaling as $1/r^2$; this comes from the contribution $A(t)^2 \mathbf{u}_{2,0}^{(\mathrm{T})}$ associated with heat-spot translation. The displacement $\Delta \mathbf{X}_{1,0}(t)$ at order α scales as $1/r$. The flow $\mathbf{u}_{1,0}$ at order α scales as $1/r$, so its gradient, $\nabla \mathbf{u}_{1,0}$, scales as $1/r^2$. Therefore, in the far field, the flow $\mathbf{u}_{2,0}$ [specifically the contribution $A(t)^2 \mathbf{u}_{2,0}^{(\mathrm{T})}$] at order α^2 provides the dominant contribution to the integrand in Eq. (120).

Using this and Eq. (101) gives

$$\Delta \mathbf{X}_{2,0}(\mathbf{X}_0; t_0) \sim -\frac{1}{4} \int_{-t_0}^{t_0} A(t)^2 \left\{ \mathbf{e}_x \left[\frac{1}{r^2} - \frac{2(x-t)^2}{r^4} \right] + \mathbf{e}_y \left[-\frac{2(x-t)y}{r^4} \right] \right\} \Bigg|_{\mathbf{X}_0} dt, \qquad (121)$$

provided that $r \gg 1$ throughout the scan period.

If, additionally, the material point is many scan-path lengths away from the heat spot, i.e., $r \gg \ell$, then we may also approximate the spatially varying factor in the integrand with its value at $t = 0$. This is simply the leading-order Taylor-expansion in t. This gives

$$\Delta \mathbf{X}_{2,0}(\mathbf{X}_0; t_0) \sim -\frac{1}{4} \int_{-t_0}^{t_0} A(t)^2 \, dt \left[\mathbf{e}_x \left(\frac{1}{|\mathbf{X}_0|^2} - \frac{2X_0^2}{|\mathbf{X}_0|^4} \right) + \mathbf{e}_y \left(-\frac{2X_0 Y_0}{|\mathbf{X}_0|^4} \right) \right]. \qquad (122)$$

Correspondingly, the velocity $\Delta \mathbf{X}_{2,0}(t_0)/2t_0$ at order α^2 of the material point, averaged over one scan, is given by

$$\frac{\Delta \mathbf{X}_{2,0}(\mathbf{X}_0; t_0)}{2t_0} \sim -\frac{1}{8t_0} \int_{-t_0}^{t_0} A(t)^2 \, dt \left[\mathbf{e}_x \left(\frac{1}{|\mathbf{X}_0|^2} - \frac{2X_0^2}{|\mathbf{X}_0|^4} \right) + \mathbf{e}_y \left(-\frac{2X_0 Y_0}{|\mathbf{X}_0|^4} \right) \right], \qquad (123)$$

for material points far from the scan path (many heat-spot radii and many scan-path lengths away). Similarly to order $\alpha\beta$ (i.e., the other quadratic order), this far-field average Lagrangian velocity is a hydrodynamic source dipole, with strength proportional to the time-average of the square of the heat-spot amplitude. However, here at order α^2, the direction of far-field flow corresponds to a sink on the left and a source on the right. This is therefore opposite to order $\alpha\beta$, consistent with the physical mechanism for the instantaneous flow $A(t)^2 \mathbf{u}_{2,0}^{(\mathrm{T})}$ explained in Sec. II H 6.

C. Net displacement in the far field

We computed above the net displacement of a material point correct to quadratic order and derived analytical expressions for the net displacements at order $\alpha\beta$ and order α^2 of material points far from the scan path, for a Gaussian heat spot with arbitrary amplitude. Combining Eqs. (115) and (122), the dimensional net displacement of a material point far from the scan path is therefore given by

$$\Delta \mathbf{X}(\mathbf{X}_0; t_0) \sim \frac{1}{4} (\alpha\beta - \alpha^2) \Delta T_0^2 U \int_{-t_0}^{t_0} A(t)^2 \, dt \left[\mathbf{e}_x \left(\frac{a^2}{|\mathbf{X}_0|^2} - \frac{2a^2 X_0^2}{|\mathbf{X}_0|^4} \right) + \mathbf{e}_y \left(-\frac{2a^2 X_0 Y_0}{|\mathbf{X}_0|^4} \right) \right], \quad (124)$$

correct to quadratic order. The corresponding average velocity (over a scan period) of the material point with initial position $\mathbf{X}_0$ is given by

$$\frac{\Delta \mathbf{X}(\mathbf{X}_0; t_0)}{2t_0} \sim \frac{1}{8t_0} (\alpha\beta - \alpha^2) \Delta T_0^2 U \int_{-t_0}^{t_0} A(t)^2 \, dt \left[\mathbf{e}_x \left(\frac{a^2}{|\mathbf{X}_0|^2} - \frac{2a^2 X_0^2}{|\mathbf{X}_0|^4} \right) + \mathbf{e}_y \left(-\frac{2a^2 X_0 Y_0}{|\mathbf{X}_0|^4} \right) \right]. \tag{125}$$

This is a hydrodynamic source dipole, with strength quadratic in the heat-spot amplitude. We have thus shown that the exponentially decaying heat spot induces motion of tracers with average

velocity decaying algebraically in the far field (i.e., slower than the forcing). The direction of net displacement of material points in the far field depends critically on the relative size of the thermal expansion coefficient α and the thermal viscosity coefficient β, via the prefactor of $(\alpha\beta - \alpha^2)$. As a reminder, this prefactor is expected to be positive for water or glycerol-water solution, i.e., the order-$\alpha\beta$ behavior dominates.

V. COMPARISON WITH EXPERIMENTS

A. Trajectories of tracers over many scan periods

In Sec. II, we introduced our mathematical model for the microfluidic experiments reported in Ref. [34]. We solved explicitly for the instantaneous flow induced by a translating Gaussian heat spot with arbitrary amplitude and then examined in Sec. III the leading-order trajectories of material points during one scan period, occurring at order α. In particular, we showed that the net displacement of any material point after a full scan period is zero at order α. The leading-order net displacement instead occurs at higher order and is a quadratic effect (Sec. IV), which in fact holds for a general heat spot. In experiments [28,30,34], repeated scanning of the heat spot along a finite scan path, i.e., localized forcing, creates a large-scale fluid flow that transports material points over large distances, over the course of many scan periods. To understand this net transport due to repeated scanning, we use our results in Sec. IV on the net displacement and average velocity of material points, due to a full scan. In this section, we quantitatively compare these theoretical results with experimental data [34]. Specifically, we focus on Figs. 2(d) and 2(f) from Ref. [34].

In the controlled experiments in Ref. [34], the laser spot scanned at frequency 1–3 kHz and the scan path had length 11 µm. The laser spot heated the fluid locally, causing a maximum temperature perturbation of a few kelvins; the characteristic radius of the temperature perturbation was $a = 4$–4.5 µm. The resulting trajectories of tracer beads in the fluid were recorded over a period of 100 s. The flow recordings were made with an exposure time of at least 10 times the scan period. As a result, the trajectories show the displacement of tracers over many scan periods, instead of the displacement during a single scan period.

In experiments, the motion of the tracer beads was tracked in the midplane, i.e., halfway between the parallel plates, at $z = h/2$ in terms of notation in Fig. 2. Recall that in our theory, we dealt with the z-averaged velocity field $\overline{\mathbf{u}}_{\mathrm{H}}$, which we wrote as $\mathbf{u}$ to simplify notation. To convert to the midplane velocity field, we recall that within the lubrication approximation, the velocity in the midplane $z = h/2$ is given by

$$\mathbf{u}_{\mathrm{H}}|_{z=h/2} = \tfrac{3}{2}\overline{\mathbf{u}}_{\mathrm{H}}, \qquad (126)$$

since the flow has quadratic dependence on z between the two no-slip surfaces. We model the tracer beads as material points for simplicity and discuss this assumption later.

To produce our theoretical plots, we choose the sinusoidal heat-spot amplitude given by Eq. (55), based on earlier experiments and modeling [28]. We use parameter values within the experimental range: characteristic heat-spot radius $a = 4$ µm, scan-path length $2\ell = 11$ µm, scan frequency $f = 3.2$ kHz, and characteristic temperature change $\Delta T_0 = 8$ K. The fluid in the experiment was 50% v/v glycerol-water solution. For this, we estimate the dimensional thermal expansion coefficient as $\alpha = 5 \times 10^{-4}$ K^{-1} and the thermal viscosity coefficient as $\beta = 4 \times 10^{-2}$ K^{-1} [39]. The dimensionless values are then $\alpha = 4 \times 10^{-3}$ and $\beta = 0.32$. Since we have $\beta \gg \alpha$, we may neglect order α^2 contributions in our theory relative to order $\alpha\beta$. We begin with a qualitative comparison of the experimental and theoretical trajectories of tracer beads over many scans. In Fig. 2(d) of Ref. [34], the experimentally found trajectories of individual tracer beads are plotted. We compare in Fig. 27 these experimental data [Fig. 27(a)] with our dimensionalized theory [Fig. 27(b)]. Recall that our theory is valid in the limit of small (dimensionless) thermal expansion coefficient α and thermal viscosity coefficient β, with the leading-order trajectories of material points over many scans given by the streamlines of the leading-order average velocity of the material points (order $\alpha\beta$). We plot these streamlines in Fig. 27(b); this is a dimensionalized version of Fig. 23.
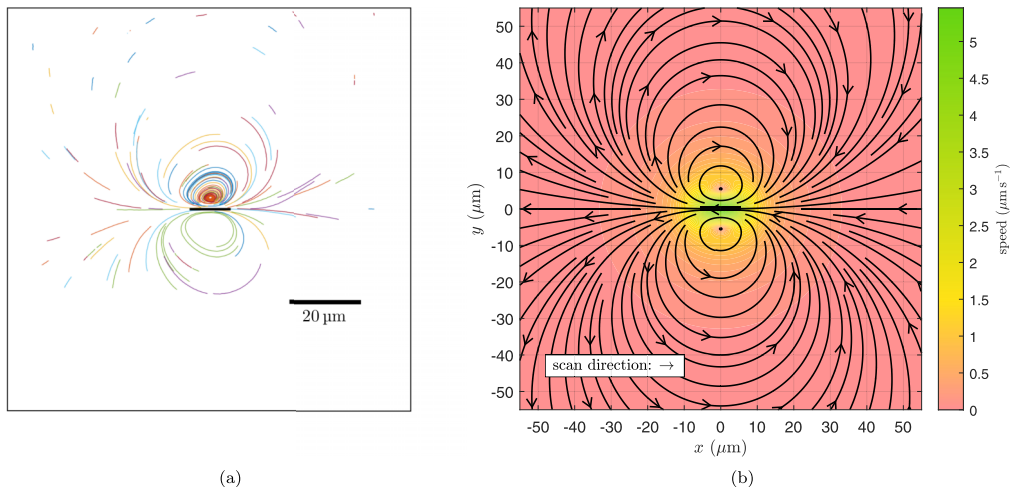
FIG. 27. Comparison between experimental and theoretical results for trajectories of tracer beads over many scans of the heat spot. (a) Experimentally found trajectories of tracer beads in the midplane (halfway between the parallel plates), from data gathered over a time period of 100 s, adapted with permission from Fig. 2(d) of Ref. [34] (The Optical Society). (b) Theoretical leading-order trajectories of material points in the midplane ($z = h/2$) over many scans, with fully dimensional units; the average speed of material points is indicated with color. During each scan, the heat spot translates in the positive x direction in our theory (scan direction). In both panels, the scan path is indicated with a thick black line segment.

Next, to compare theory with experiment quantitatively, we illustrate in Fig. 28 how the speed of tracer beads varies spatially. In Fig. 28(a), we replot the data in Fig. 2(f) from Ref. [34]. This is a log–log scatter plot of the speed of tracer beads in the midplane, averaged over 0.5 s, against the distance of the bead from the midpoint of the scan path (the origin in our theoretical model). We display in Fig. 28(b) an equivalent theoretical scatter plot for material points, with initial positions lying on a square grid with spacing of 0.3 μm. Finally, in Fig. 28(c), we plot the leading-order speed of a material point in the midplane, averaged over one scan, against the distance of the material point from the origin (log–log scale), at fixed angles $\phi = 0, \pi/8, \pi/4, 3\pi/8$, and $\pi/2$ to the x axis. This will allow us to better understand the first two, directly comparable plots, in Figs. 28(a) and 28(b).

B. Predictions of theoretical model

From Figs. 27 and 28, we see that our theoretical model can produce qualitative and quantitative predictions in agreement with the experimental data, from the near field to the far field.

First, our theory accurately predicts the far-field decay of the average speed of tracers as the inverse squared distance. Crucially, we showed rigorously that in the far field, even though the leading-order instantaneous velocity field is a source flow (decaying as $1/r$), the leading-order average velocity of tracers is a source dipole (decaying as $1/r^2$) because the leading-order instantaneous flow always averages to zero over one scan period. As a result, the leading-order average velocity of tracers inherits the $1/r^2$ decay from higher-order contributions to the instantaneous flow induced by the heat spot.

Second, our theory rigorously shows that the average velocity of tracers throughout space scales as $\alpha\beta\Delta T_0^2 U$ at leading order, for a general heat spot and finite scan path, for a fluid with $\beta \gg \alpha$. This again follows from our result that the net displacement of a material point is zero at order α; the leading-order average velocity is therefore quadratic in the heat-spot amplitude. The linear scaling with α is consistent with experiments in which α is negative (for water below 4°C) [30] instead
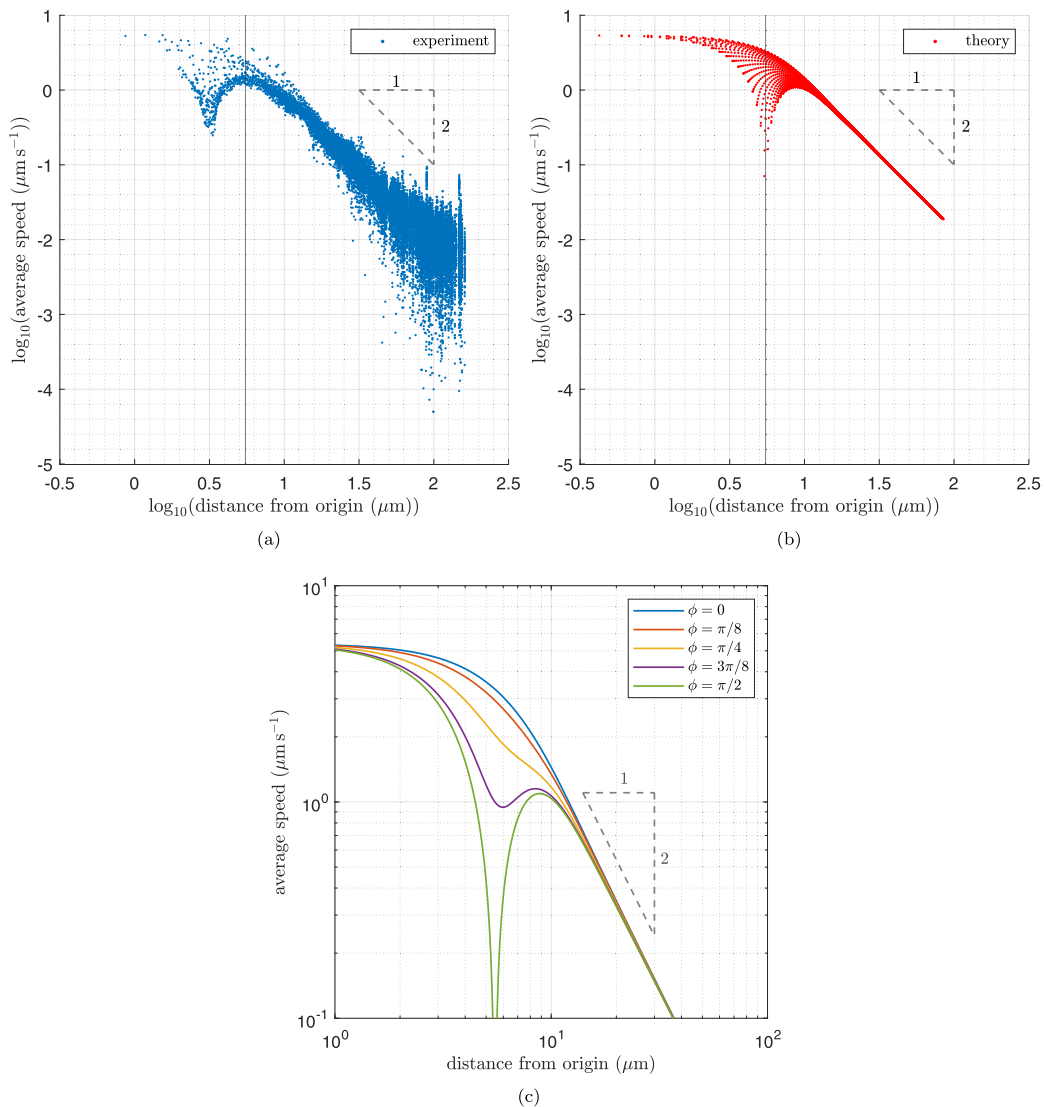
(a)

(b)

(c)

FIG. 28. Comparison between experimental data and theory for average speed of tracer beads. (a) Experimental data [34]. Log–log scatter plot of speed of tracer beads in the midplane averaged over 0.5 s vs distance of tracer bead from the origin (the midpoint of the scan path). Data from Fig. 2(f) in Ref. [34] replotted. (b) Theoretical leading-order prediction for panel (a), now dimensional. To generate the data points, the tracers are placed at initial positions lying on a square grid with spacing of 0.3 μm. In panels (a) and (b), the black vertical line marks the distance from the origin corresponding to the end of the scan path, i.e., $\ell = 5.5$ μm. (c) Theoretical prediction. Log–log plot of leading-order speed of a material point averaged over one scan vs distance of the material point from the origin, along radial lines at fixed angles $\phi = 0$, $\pi/8$, $\pi/4$, $3\pi/8$, and $\pi/2$ to the x axis. Parameters are the same as for panel (b).

of positive; the observed net transport of tracers reversed in direction. The quadratic scaling with heat-spot amplitude is also supported by experimental data [28,30] and earlier theory for tracers lying on the scan path [30].

Third, our hydrodynamic theory successfully reproduces the closed-loop trajectories of tracers over many scans seen in experiments and approximately predicts the position of the middle of the

closed loops, where the average speed of tracer beads dips. The direction of circulation of tracers, relative to the scan direction, matches that reported in experiments [30]. Importantly, from Eq. (125) for the far-field average Lagrangian velocity, this direction is set by the relative sizes of the thermal expansion coefficient α and the thermal viscosity coefficient β. Here, we have $\beta \gg \alpha$ for glycerol-water solution; consistent with this, our theory correctly predicts that on the scan path, the average velocity of tracers is in the opposite direction to the translation of the heat spot.

Exploring this near-field behavior further, on the y axis at the middle of a closed loop, the average speed of a material point over one scan is zero, as we see in Fig. 28(c). In contrast with this, in the experimental data [Fig. 28(a)] and the theoretical equivalent [Fig. 28(b)], data points do not reach zero average speed in the near field. By comparing the two theoretical plots in Figs. 28(b) and 28(c), we see that this can be accounted for by the nonzero spacing between the tracer beads in experiments. In our fully deterministic, hydrodynamic theory, spacing between material points that contribute to the scatter plots can ensure that none of them have average speed of precisely zero.

C. Scaling arguments for neglected physical effects

Recall that in our model, we neglected both gravity and inertia, due to the small length scales involved. We now verify using scaling arguments that this is justified, *a posteriori*.

As a reminder on the effect of gravity, the horizontal density gradients produce horizontal gradients in hydrostatic pressure, driving a gravity current [36,43]. From the momentum equations, this gravity-driven flow scales as $\rho_0 \alpha g h^3 \Delta T_0 / 2\eta_0 a$. However, the flow driven by thermal expansion, which we focus on in our article, scales as $\alpha \Delta T_0 U$. The ratio of the gravity-driven flow to the thermal-expansion-driven flow therefore scales as $\rho_0 g h^3 / 2\eta_0 a U$, which is approximately 0.03 for the experiments in Ref. [34]. This is indeed small, so gravity can be neglected.

Similarly, we can check the size of inertial terms relative to viscous terms in the momentum equation, based on our solution to the inertialess problem. The inertial term scales as

$$\rho \frac{\partial \mathbf{u}_H}{\partial t} \sim \rho_0 \alpha \Delta T_0 \left\{ 2af^2, Uf, \frac{U^2}{2a} \right\}, \tag{127}$$

where the three options exist due to the two contributions to the flow (switching on and translation), i.e., due to the two different timescales in the problem (scan period and advective timescale). The viscous term scales as

$$\eta \frac{\partial^2 \mathbf{u}_H}{\partial z^2} \sim \frac{\eta_0 \alpha \Delta T_0}{h^2} \{2af, U\}. \tag{128}$$

Then the ratio of the inertial term to the viscous term scales as (using $U = 2\ell f$)

$$\frac{\text{inertial term}}{\text{viscous term}} \sim \frac{\rho_0 h^2 f}{\eta_0} \left\{ 1, \frac{a}{\ell}, \frac{\ell}{a}, \frac{\ell^2}{a^2} \right\}. \tag{129}$$

The maximum value of this is approximately 0.1 for the experiments in Ref. [34], which is indeed small.

D. Limitations of theoretical model

We observe in Figs. 27 and 28 two key differences between the experimental and theoretical results, which we now discuss. First, in the experimental data [Fig. 28(a)], the dip in the average speed of tracer beads is a distance of less than half the scan-path length (i.e., less than ℓ) from the midpoint of the scan path, whereas this dip is slightly further away in the theoretical equivalent [Fig. 28(b)]. Second, in the far field, the experimental data shows a much greater range of speeds at any given distance from the origin than the theoretical model predicts.

1. Lubrication limit

What are the limitations in our model that could contribute to these discrepancies? First, we used the lubrication limit to simplify the momentum equations. This corresponds to the limit where the characteristic horizontal length scale is much larger than the vertical; specifically, where the heat-spot diameter is much larger than the separation of the parallel plates. However, in the experiments in which the spatial decay of average speed of tracers was quantified [34], the characteristic heat-spot diameter was $2a = 8$–9 μm and the separation of the parallel plates was $h = 15$ μm, i.e., the characteristic heat-spot diameter and plate separation were comparable. In the near field, this order-1 aspect ratio (instead of a thin-film geometry) is expected to become important, which could therefore help explain the slight difference between the predicted and experimentally found position of the dip in the average speed of tracers.

2. Diffusion of tracer beads

Second, our theoretical model is fully deterministic; we have not included any noise. We modeled the tracer beads as material points, simply advected by the flow induced by the heat spot. In the experiments [34], the tracer beads had a radius of $b = 0.25$ μm, which is much smaller than the length scale on which the flow field varies, the characteristic radius of the heat spot $a = 4$ μm. What is the contribution of thermal noise in comparison with the average (deterministic) velocity of the tracers? A diffusive scaling for the speed of a tracer is given by D/b, where D is the diffusion constant associated with the tracer bead. By the Stokes–Einstein relationship, this diffusion constant scales as

$$D \approx \frac{k_{\mathrm{B}} T_0}{6\pi \eta_0 b}, \tag{130}$$

where k_B is Boltzmann's constant, T_0 is the reference temperature, and η_0 is the reference viscosity of the fluid. The diffusive scaling for speed is therefore

$$\frac{D}{b} \approx \frac{k_{\mathrm{B}} T_0}{6\pi \eta_0 b^2}. \tag{131}$$

Using $k_{\mathrm{B}} \approx 10^{-23}$ J K^{-1}, $T_0 \approx 300$ K, and $\eta_0 \approx 10^{-2}$ Pa s, we find that D/b is on the order of 0.1 μm s^{-1}.

How does this compare with the deterministic results? The average velocity of tracers varies spatially, as we saw in Fig. 28(a). In the near field, the average speed of a tracer is on the order of 1 μm s^{-1}, which is much greater than the diffusive speed. We may therefore typically neglect the effect of noise in the near field. As a result, in the near field, our deterministic theory successfully predicts the shape of the envelope in the log–log plot of speed versus radius in Fig. 28.

At the middle of the closed-loop trajectories [Fig. 27(b)], our deterministic theory predicts that the average speed of tracers is zero [Fig. 28(c)]. However, the experimental and theoretical scatter plots [Figs. 28(a) and 28(b), respectively] both only show a dip in the average speed. As explained earlier, the spacing between the tracer beads that contribute to the scatter plots can account for this in our deterministic theory; noise can also contribute to this feature.

In the far field, our deterministic theory predicts that the average speed of tracers decays, following an inverse-square law. Noise therefore becomes important for tracers far from the scan path. This may help explain the scatter seen in the far field for the experimental log–log plot of speed versus radius [Fig. 28(a)], which is not seen in the deterministic hydrodynamic theory [Fig. 28(b)]. Notably, this scatter is prominent where the average speed is smaller than around 0.1 μm s^{-1}, precisely the diffusive scale for the average speed of the tracer bead predicted here. In Ref. [34], the transport induced by the repeatedly scanning heat spot was used to manipulate beads and a feedback loop was needed to deal with the stochasticity of the particle positions. Our hydrodynamic theory predicts quantitatively where this stochasticity becomes important in comparison with the deterministic flow.

3. Temperature profile

In our hydrodynamic theory, the two-dimensional, Gaussian temperature profile we impose to solve our equations analytically is an idealization. It is possible that the temperature perturbation in the microfluidic experiments [34] did not have circular symmetry, depending on the scan frequency used. The sinusoidal amplitude function is also idealized, chosen based on earlier numerical work [28]. Importantly, however, our theoretical result that the average velocity of material points is quadratic in the temperature perturbation holds for a heat spot of any shape with arbitrary time-dependent amplitude.

Note also that our theory dealt with temperature profiles independent of z, as we assumed that the separation of the parallel plates is small compared with the heat-spot diameter. In experiments, the temperature profile was three-dimensional, while the horizontal and vertical length scales were of similar magnitude. A laser beam has a waist; the width of the laser beam varies in the z direction, though this variation is indeed slower than the exponential decay in the horizontal directions. The temperature perturbation correspondingly also has a waist, which is not included in our theory.

4. Energy balance

Finally, in our theory, we prescribe the temperature field and then solve the momentum and mass equations. In reality, the temperature profile satisfies an energy balance equation [36], where the fluid is heated due to the laser spot, and the heat diffuses through the fluid and is advected by the flow, which in turn depends on the temperature field. This couples the heat and fluid-flow problems. Scaling suggests that advection of heat ($\mathbf{u} \cdot \nabla T$) is a much smaller effect than the rate of change of temperature at a fixed position due to scanning ($\partial T / \partial t$). However, comparing this rate of change of temperature with diffusion of heat gives a thermal Péclet number scaling as

$$\mathrm{Pe}_{\mathrm{thermal}} \sim \frac{\rho c_p \frac{\partial T}{\partial t}}{\nabla \cdot (k \nabla T)} \sim \frac{(2a)^2 \rho_0 c_p f}{k} \left\{ 1, \frac{\ell}{a} \right\}, \tag{132}$$

where c_p is the specific heat capacity and k is the thermal conductivity of the fluid; again, the two possible scalings arise from the two timescales appearing in the temperature profile. This Péclet number is small provided the scan frequency is sufficiently small, but could be approximately 1 for some of the experiments in Ref. [34]. Hence, future theoretical models could therefore solve for the temperature via its transport equation instead of prescribing the temperature field.

VI. SUMMARY AND PERSPECTIVE

In summary, motivated by recent experimental advances in artificial cytoplasmic streaming, we presented in this article an analytical, theoretical model for both the fluid flow and the transport induced by a scanning heat spot. In Sec. II, we solved analytically for the instantaneous flow field of viscous fluid between two parallel plates, driven by small, prescribed temperature changes, i.e., in the limit of small dimensionless thermal expansion coefficient α and thermal viscosity coefficient β. Our model allows the heat spot to have time-varying amplitude and the scan path to be of arbitrary length. We showed mathematically that the flow is driven by thermal expansion. The leading-order instantaneous flow field is a potential flow solely due to thermal expansion of the fluid and is independent of the thermal viscosity coefficient, in agreement with earlier studies [29]. Specifically, it is proportional to the characteristic temperature change and occurs at order α. We demonstrated that provided the heat-spot amplitude varies with time, the far-field instantaneous flow is a source (or sink) flow, due to the switching-on (or switching-off) of the heat spot. This generically dominates over the hydrodynamic source dipole in the far field due to the translation of the heat spot. However, the flow associated with the translation of the heat spot forms the basis of our explanations of net transport due to thermoviscous flow.

We next solved for the instantaneous flow at quadratic order, i.e., at order $\alpha\beta$ and order α^2, as this in fact gives rise to the leading-order net displacement of material points. These are both quadratic in the characteristic temperature perturbation. The first correction to the leading-order flow due to thermal viscosity changes, at order $\alpha\beta$, is made up of two contributions, the leading-order flow associated with translation of the heat spot, modulated by the temperature profile, and another potential flow. The leading-order flow modulated by the temperature profile is the intuitive effect of thermal viscosity changes, as described previously [29,30]. We then saw mathematically that the potential flow enforces incompressibility of the flow at order $\alpha\beta$ and is solely responsible for the far field of the flow at order $\alpha\beta$, which is a hydrodynamic source dipole.

The other flow at quadratic order, i.e., at order α^2, is compressible. In the far field, this flow is also a hydrodynamic source dipole, in the opposite direction to that at order $\alpha\beta$.

We next took a Lagrangian perspective in Sec. III and examined the trajectories of material points during one scan. We solved analytically for the leading-order trajectory of an individual material point as a function of time. The displacement of a material point typically occurs at order α. In experiments [34], the heat spot scans repeatedly along a finite scan path and the transport induced is visualized using tracers. Because the exposure time of recordings is much longer than a scan period, we see the net displacement of these tracers. However, we showed that the net displacement of a material point (due to a full scan) at order α is zero, for any heat-spot amplitude and shape and for any scan path length, generalizing earlier work [29].

We then discussed the net displacement of material points at higher order in Sec. IV. The leading-order net displacement of a material point occurs at quadratic order and so is quadratic in the heat-spot amplitude. This can be at order $\alpha\beta$ or at order α^2, but for the fluid used in experiments [30,34], the order-$\alpha\beta$ contribution dominates. At order $\alpha\beta$, the net displacement results from amplification of flow due to reduced viscosity in the locally heated fluid. This gives rise to strong leftward transport near the scan path, as explained in Ref. [30]. Using our analytical solutions, we further showed that the far-field average velocity of the tracers is a source dipole, with rightward transport far from the x axis, inherited from the instantaneous flow at the same order. For other fluids, the contribution at order α^2 to the average Lagrangian velocity may also be important; this is also a source dipole in the far field.

In Sec. V, we revisited the net displacement of material points, to compare with the trajectories of material points over many scans from experiments [34]. In particular, our analytical expression for the flow field allowed us to understand the net displacement of material points throughout space, not only those on the scan path. We found that our model could provide quantitative agreement with the experimental results for realistic parameter values, explaining the experimentally found $1/r^2$ far-field spatial decay of the average speed of tracers as a source dipole.

We also discussed limitations of our model in the context of the particular experiments of Ref. [34], most significantly, the role of thermal noise, the lubrication approximation, and the prescribed temperature profile. These simplifications could of course be revisited in future work, allowing us to obtain further insight into thermoviscous fluid flows.

Our analysis also suggests potential future experiments to validate the model. For example, existing imaging has focused on the net transport induced by repeated scanning of the laser, but new experiments with a lower laser scanning frequency may allow the instantaneous fluid flow to be visualized and compared with the theory. The choice of properties of the laser scanning, such as amplitude function or the shape of the heat spot, could also be investigated and optimized for specific applications.

In addition to the fundamental understanding of the experiments in Ref. [34], our work provides a rigorous theoretical platform that will facilitate design of future FLUCS experiments at lower computational expense. Indeed, in this study we derived not only how all transport quantities scale with the parameters of the problem but also all mathematical prefactors. Our approach can therefore predict the detailed nature of the thermoviscous fluid flows in both space and time.

Even in the geometrical setup considered in this article, our work may be extended and adapted to the case where the laser scan paths follow arbitrary two-dimensional curves, instead of the straight line segments assumed here. We could also consider a localized heating that involves the simultaneous scanning of multiple heat spots along multiple scan paths, enabling the generation of new patterns of fluid flow and transport. This may in turn allow finer control of particles at the micrometer scale, with potential applications in thermal trapping, microrobotics and medicine [31,44–46]. Beyond the parallel-plate setup addressed here, future theoretical modeling could examine the nature of similarly generated thermoviscous flow in different geometries, and probe in particular the role of confinement in flow generation.

Furthermore, while we assumed that the flow of glycerol-water solution had a Newtonian behavior in our model of microfluidic experiments [34], we expect that in FLUCS experiments in cell biology [28], the flow of cytoplasm would instead have complex rheological behavior. In particular, given that the forcing from the laser is periodic in time, qualitatively different flows to the Newtonian case could be induced provided that scanning occurs at a rate faster than the relevant relaxation for the fluid. The typical scanning rate used in FLUCS experiments is on the order of 1 kHz, whereas typical relaxation times in cellular flows can be on the order of tenths of seconds [47], so viscoelasticity is expected to play a role in many applications of FLUCS.

APPENDIX A: SCALING ARGUMENT TO DERIVE THE MOMENTUM EQUATIONS IN THE LUBRICATION LIMIT

We present in this Appendix the derivation of the momentum equations in the lubrication limit, Eqs. (7)–(9), via a scaling argument, as referred to in Sec. II A. Recall that in Sec. II A, we introduced the two assumptions that the vertical separation of the plates is much less than the characteristic heat-spot diameter, $h \ll 2a$, and that the temperature profile is independent of z, $\frac{\partial \Delta T}{\partial z} = 0$. The horizontal coordinates x and y scale as the characteristic heat-spot radius a (omitting numerical factors); the vertical coordinate z scales as the plate separation h. Partial derivatives with respect to horizontal coordinates thus scale as $\partial/\partial x$, $\partial/\partial y \sim 1/a$, whereas the partial derivative with respect to z scales as $\partial/\partial z \sim 1/h$. We write u for the horizontal velocity scale and w for the vertical velocity scale. The shear viscosity, bulk viscosity, and density of the fluid scale as their reference values η_0, κ_0, and ρ_0, respectively, at the reference temperature T_0.

To deduce the relative scalings of the horizontal and vertical fluid velocities, we first consider the mass conservation equation. This may be written as

$$\frac{\partial \rho}{\partial t} + \nabla_{\mathrm{H}} \cdot (\rho \mathbf{u}_{\mathrm{H}}) + \frac{\partial (\rho w)}{\partial z} = 0, \tag{A1}$$

where $\mathbf{u}_{\mathrm{H}} \equiv (u, v)$ is the horizontal velocity field and the horizontal gradient is $\nabla_{\mathrm{H}} \equiv (\partial/\partial x, \partial/\partial y)$. Focusing on the relative scalings of the second and third terms in this equation, there are three cases to consider: (i) $u/a \sim w/h$, (ii) $u/a \gg w/h$, and (iii) $u/a \ll w/h$. It can be shown that both case (ii) and case (iii) are inconsistent, leading to contradictions. In case (ii), the term $\frac{\partial (\rho w)}{\partial z}$ in Eq. (A1) is neglected in favour of the other two terms. Although a scaling argument yields the same momentum equations in case (ii) as in case (i), the resulting parabolic horizontal velocity profile cannot satisfy the leading-order mass conservation equation under the assumption of case (ii). In

case (iii), the horizontal contribution, $\boldsymbol{\nabla}_H \cdot (\rho \mathbf{u}_H)$, is neglected in Eq. (A1) in favour of the other two terms. The mass conservation equation in this case therefore may be directly integrated with respect to z (noting that the density field is independent of z) to find the vertical velocity field, but the result then cannot satisfy the no-slip boundary condition on both of the parallel plates; thus, this case is also inconsistent. The only consistent scaling, relating the horizontal and vertical velocities, is therefore given by

$$\frac{u}{a} \sim \frac{w}{h}. \tag{A2}$$

In this paper, we solve for the horizontal velocity field. From this, the vertical velocity field w can be computed by integrating the mass conservation equation with respect to z; the scaling above may therefore be verified to be consistent.

We next consider the momentum equation. As commented below Eqs. (7)–(9) in Sec. II A, we neglect inertia and gravity due to the small length scales and thin-film geometry involved; we verify this *a posteriori* in Sec. V C with a scaling argument. From Eqs. (5) and (6), the momentum equation, in suffix notation ($i = 1, 2, 3$), therefore simplifies to

$$-\frac{\partial p}{\partial x_i} + \kappa \frac{\partial}{\partial x_i}\frac{\partial u_j}{\partial x_j} + \frac{\partial \kappa}{\partial x_i}\frac{\partial u_j}{\partial x_j} + \eta \frac{\partial}{\partial x_j}\frac{\partial u_i}{\partial x_j} + \frac{1}{3}\eta\frac{\partial}{\partial x_i}\frac{\partial u_j}{\partial x_j} + \frac{\partial \eta}{\partial x_j}\left(\frac{\partial u_i}{\partial x_j} + \frac{\partial u_j}{\partial x_i}\right) - \frac{2}{3}\frac{\partial \eta}{\partial x_i}\frac{\partial u_j}{\partial x_j} = 0. \tag{A3}$$

We observe that since the temperature profile is assumed to be independent of z and the bulk and shear viscosities are functions of temperature, the bulk and shear viscosities are also independent of z; their z-derivatives, $\frac{\partial \kappa}{\partial z}$ and $\frac{\partial \eta}{\partial z}$, respectively, are therefore zero. We now write down the scalings of all the terms in the horizontal momentum equation ($i = 1, 2$) as

$$\frac{\partial p}{\partial x_i} \sim \frac{p}{a}; \tag{A4}$$

$$\kappa \frac{\partial}{\partial x_i}\frac{\partial u_j}{\partial x_j}, \frac{\partial \kappa}{\partial x_i}\frac{\partial u_j}{\partial x_j} \sim \frac{\kappa_0}{a}\max\left\{\frac{u}{a}, \frac{w}{h}\right\} \sim \frac{\kappa_0 u}{a^2}, \quad \text{using } \frac{u}{a} \sim \frac{w}{h}; \tag{A5}$$

$$\eta \frac{\partial}{\partial x_j}\frac{\partial u_i}{\partial x_j} \sim \eta_0 u \max\left\{\frac{1}{a^2}, \frac{1}{h^2}\right\} \sim \eta\frac{\partial^2 u_i}{\partial z^2} \sim \frac{\eta_0 u}{h^2}, \quad \text{using } h \ll a; \tag{A6}$$

$$\eta \frac{\partial}{\partial x_i}\frac{\partial u_j}{\partial x_j}, \frac{\partial \eta}{\partial x_i}\frac{\partial u_j}{\partial x_j} \sim \frac{\eta_0}{a}\max\left\{\frac{u}{a}, \frac{w}{h}\right\} \sim \frac{\eta_0 u}{a^2}, \quad \text{using } \frac{u}{a} \sim \frac{w}{h}; \tag{A7}$$

$$\frac{\partial \eta}{\partial x_j}\frac{\partial u_i}{\partial x_j}, \frac{\partial \eta}{\partial x_j}\frac{\partial u_j}{\partial x_i} \sim \frac{\eta_0 u}{a^2}, \quad \text{using } \frac{\partial \eta}{\partial z} = 0. \tag{A8}$$

Comparing these scalings, we have $\frac{\eta_0 u}{a^2} \ll \frac{\eta_0 u}{h^2}$, since $h \ll a$. We also assume that κ_0 and η_0 are of similar magnitude, so we have $\frac{\kappa_0 u}{a^2} \ll \frac{\eta_0 u}{h^2}$. In the lubrication limit, the leading-order balance in the horizontal momentum equation, in terms of scalings, is thus given by

$$\frac{p}{a} \sim \frac{\eta_0 u}{h^2}, \tag{A9}$$

from which we deduce the pressure scale, identical to that for the classical, incompressible case.

Next, we write down the scalings of all the terms in the vertical momentum equation as

$$\frac{\partial p}{\partial z} \sim \frac{p}{h} \sim \frac{\eta_0 a u}{h^3}, \quad \text{using Eq. (A9)}; \tag{A10}$$

$$\kappa \frac{\partial}{\partial z}\frac{\partial u_j}{\partial x_j} \sim \frac{\kappa_0}{h}\max\left\{\frac{u}{a}, \frac{w}{h}\right\} \sim \frac{\kappa_0 u}{ah}, \quad \text{using } \frac{u}{a} \sim \frac{w}{h}; \tag{A11}$$

$$\frac{\partial \kappa}{\partial z}\frac{\partial u_j}{\partial x_j} \sim 0, \quad \text{using } \frac{\partial \kappa}{\partial z} = 0; \tag{A12}$$

$$\eta \frac{\partial}{\partial x_j} \frac{\partial w}{\partial x_j} \sim \eta_0 w \max \left\{ \frac{1}{a^2}, \frac{1}{h^2} \right\} \sim \eta \frac{\partial^2 w}{\partial z^2} \sim \frac{\eta_0 w}{h^2} \sim \frac{\eta_0 u}{ah}, \quad \text{using } h \ll a \text{ and } \frac{u}{a} \sim \frac{w}{h}; \quad \text{(A13)}$$

$$\eta \frac{\partial}{\partial z} \frac{\partial u_j}{\partial x_j} \sim \frac{\eta_0}{h} \max \left\{ \frac{u}{a}, \frac{w}{h} \right\} \sim \frac{\eta_0 u}{ah}, \quad \text{using } \frac{u}{a} \sim \frac{w}{h}; \quad \text{(A14)}$$

$$\frac{\partial \eta}{\partial x_j} \frac{\partial w}{\partial x_j} \sim \frac{\eta_0 w}{a^2} \sim \frac{\eta_0 u h}{a^3}, \quad \text{using } \frac{\partial \eta}{\partial z} = 0 \text{ and } \frac{u}{a} \sim \frac{w}{h}; \quad \text{(A15)}$$

$$\frac{\partial \eta}{\partial x_j} \frac{\partial u_j}{\partial z} \sim \frac{\eta_0 u}{ah}, \quad \text{using } \frac{\partial \eta}{\partial z} = 0; \quad \text{(A16)}$$

$$\frac{\partial \eta}{\partial z} \frac{\partial u_j}{\partial x_j} \sim 0, \quad \text{using } \frac{\partial \eta}{\partial z} = 0. \quad \text{(A17)}$$

We see that the scaling for the vertical pressure gradient is at least a factor of $a^2/h^2 \gg 1$ times as large as the scalings of the other terms in the vertical momentum equation; the vertical pressure gradient is unbalanced, the same as in standard lubrication theory for incompressible flow. The momentum equations in the lubrication limit are therefore finally given by

$$-\frac{\partial p}{\partial x} + \eta \frac{\partial^2 u}{\partial z^2} = 0, \quad \text{(A18)}$$

$$-\frac{\partial p}{\partial y} + \eta \frac{\partial^2 v}{\partial z^2} = 0, \quad \text{(A19)}$$

$$\frac{\partial p}{\partial z} = 0, \quad \text{(A20)}$$

as stated in Eqs. (7)–(9).

APPENDIX B: DERIVATION OF SOLUTION FOR THE INSTANTANEOUS FLOW AT ORDER β^n

In this Appendix, we derive the result, stated in Sec. II E, that there is no flow at order β^n for all $n \geqslant 0$, for any prescribed temperature profile ΔT that decays at infinity. We proceed by induction.

For the base case, at order β^0 of Eq. (25) we simply have Laplace's equation

$$\nabla^2 p_{0,0} = 0, \quad \text{(B1)}$$

for the pressure $p_{0,0}$, with the boundary condition that the pressure gradient decays at infinity. The solution to this is unique, up to an additive constant that we choose to be zero without loss of generality, and given by

$$p_{0,0} = 0. \quad \text{(B2)}$$

From the velocity perturbation expansion Eq. (24), we have the corresponding flow field

$$\mathbf{u}_{0,0} = -\nabla p_{0,0} = \mathbf{0}. \quad \text{(B3)}$$

That is, at order 1, there is no flow. This is to be expected physically since in the limit of small thermal expansion coefficient α and thermal viscosity coefficient β, the coupling of the fluid flow to the temperature change is weak, so volume changes and flows driven by the heating are also weak.

For the inductive step, we assume that $p_{0,n-k} = 0$ for all k such that $1 \leqslant k \leqslant n$, where $n \geqslant 1$. We will show that this implies that $p_{0,n} = 0$ (where we again choose the arbitrary constant to be zero without loss of generality), which completes the proof by induction. Order β^n of Eq. (25) reads

$$\nabla^2 p_{0,n} + \nabla \cdot \left[\sum_{k=1}^{n} (\Delta T)^k \nabla p_{0,n-k} \right] = 0. \quad \text{(B4)}$$

By the induction hypothesis, the Poisson equation becomes Laplace's equation,

$$\nabla^2 p_{0,n} = 0, \tag{B5}$$

so, again using the boundary conditions at infinity, the solution at order β^n is

$$p_{0,n} = 0, \tag{B6}$$

as claimed. This result completes the proof by induction and corresponds to the velocity field given by

$$\mathbf{u}_{0,n} = -\sum_{k=0}^{n} (\Delta T)^k \nabla p_{0,n-k} = \mathbf{0}, \tag{B7}$$

i.e., no flow at order β^n.

---

[1] S. Vogel, *Life in Moving Fluids: The Physical Biology of Flow—Revised and Expanded Second Edition* (Princeton University Press, Princeton, NJ, 2020).

[2] G. K. Batchelor, H. K. Moffatt, and M. G. Worster, *Perspectives in Fluid Dynamics: A Collective Introduction to Current Research* (Cambridge University Press, Cambridge, UK, 2003).

[3] R. Ferrari and C. Wunsch, Ocean circulation kinetic energy: Reservoirs, sources, and sinks, Annu. Rev. Fluid Mech. **41**, 253 (2009).

[4] B. M. Hickey, R. M. Kudela, J. Nash, K. W. Bruland, W. T. Peterson, P. MacCready, E. J. Lessard, D. A. Jay, N. S. Banas, A. M. Baptista, E. P. Dever, P. M. Kosro, L. K. Kilcher, A. R. Horner-Devine, E. D. Zaron, R. M. McCabe, J. O. Peterson, P. M. Orton, J. Pan, and M. C. Lohan, River influences on shelf ecosystems: Introduction and synthesis, J. Geophys. Res. **115**, C00B17 (2010).

[5] A. R. Horner-Devine, R. D. Hetland, and D. G. MacDonald, Mixing and transport in coastal river plumes, Annu. Rev. Fluid Mech. **47**, 569 (2015).

[6] E. de Langre, Effects of wind on plants, Annu. Rev. Fluid Mech. **40**, 141 (2008).

[7] J. B. Grotberg, Respiratory fluid mechanics and transport processes, Annu. Rev. Biomed. Eng. **3**, 421 (2001).

[8] O. E. Jensen and I. L. Chernyavsky, Blood flow and transport in the human placenta, Annu. Rev. Fluid Mech. **51**, 25 (2019).

[9] T. W. Secomb, Blood flow in the microcirculation, Annu. Rev. Fluid Mech. **49**, 443 (2017).

[10] S. Nonaka, S. Yoshiba, D. Watanabe, S. Ikeuchi, T. Goto, W. F. Marshall, and H. Hamada, De novo formation of left–right asymmetry by posterior tilt of nodal cilia, PLoS Biol. **3**, e268 (2005).

[11] E. Lauga, *The Fluid Dynamics of Cell Motility* (Cambridge University Press, Cambridge, UK, 2020).

[12] A. Mogilner and A. Manhart, Intracellular fluid mechanics: Coupling cytoplasmic flow with active cytoskeletal gel, Annu. Rev. Fluid Mech. **50**, 347 (2018).

[13] B. Corti, *Osservazioni Microscopiche Sulla Tremella e Sulla Circolazione del Fluido in una Pianta Acquajuola* (Rocchi, Lucca, Italy, 1774).

[14] N. S. Allen and R. D. Allen, Cytoplasmic streaming in green plants, Annu. Rev. Biophys. Bioeng. **7**, 497 (1978).

[15] N. Kamiya, Physical and chemical basis of cytoplasmic streaming, Annu. Rev. Plant Physiol. **32**, 205 (1981).

[16] P. K. Hepler, L. Vidali, and A. Y. Cheung, Polarized cell growth in higher plants, Annu. Rev. Cell Dev. Biol. **17**, 159 (2001).

[17] J.-W. van de Meent, A. J. Sederman, L. F. Gladden, and R. E. Goldstein, Measurement of cytoplasmic streaming in single plant cells by magnetic resonance velocimetry, J. Fluid Mech. **642**, 5 (2010).

[18] S. Ganguly, L. S. Williams, I. M. Palacios, and R. E. Goldstein, Cytoplasmic streaming in *Drosophila* oocytes varies with kinesin activity and correlates with the microtubule cytoskeleton architecture, Proc. Natl. Acad. Sci. USA **109**, 15109 (2012).

[19] R. E. Goldstein and J.-W. van de Meent, A physical perspective on cytoplasmic streaming, Interface Focus **5**, 20150030 (2015).

[20] N. W. Goehring, P. K. Trong, J. S. Bois, D. Chowdhury, E. M. Nicola, A. A. Hyman, and S. W. Grill, Polarization of PAR proteins by advective triggering of a pattern-forming system, Science **334**, 1137 (2011).

[21] W. F. Pickard, Hydrodynamic aspects of protoplasmic streaming in *Chara braunii*, Protoplasma **82**, 321 (1974).

[22] R. J. Ellis, Macromolecular crowding: Obvious but underappreciated, Trends Biochem. Sci. **26**, 597 (2001).

[23] P. Hochachka, The metabolic implications of intracellular circulation, Proc. Natl. Acad. Sci. USA **96**, 12233 (1999).

[24] R. E. Goldstein, I. Tuval, and J.-W. van de Meent, Microfluidics of cytoplasmic streaming and its implications for intracellular transport, Proc. Natl. Acad. Sci. USA **105**, 3663 (2008).

[25] J.-W. van de Meent, I. Tuval, and R. E. Goldstein, Nature's Microfluidic Transporter: Rotational Cytoplasmic Streaming at High Péclet Numbers, Phys. Rev. Lett. **101**, 178102 (2008).

[26] T. Shinar, M. Mana, F. Piano, and M. J. Shelley, A model of cytoplasmically driven microtubule-based motion in the single-celled *Caenorhabditis elegans* embryo, Proc. Natl. Acad. Sci. USA **108**, 10508 (2011).

[27] K. Yi, J. R. Unruh, M. Deng, B. D. Slaughter, B. Rubinstein, and R. Li, Dynamic maintenance of asymmetric meiotic spindle position through Arp2/3-complex-driven cytoplasmic streaming in mouse oocytes, Nat. Cell Biol. **13**, 1252 (2011).

[28] M. Mittasch, P. Gross, M. Nestler, A. W. Fritsch, C. Iserman, M. Kar, M. Munder, A. Voigt, S. Alberti, S. W. Grill, and M. Kreysing, Noninvasive perturbations of intracellular flow reveal physical principles of cell organization, Nat. Cell Biol. **20**, 344 (2018).

[29] F. M. Weinert, J. A. Kraus, T. Franosch, and D. Braun, Microscale Fluid Flow Induced by Thermoviscous Expansion Along a Traveling Wave, Phys. Rev. Lett. **100**, 164501 (2008).

[30] F. M. Weinert and D. Braun, Optically driven fluid flow along arbitrary microscale patterns using thermoviscous expansion, J. Appl. Phys. **104**, 104701 (2008).

[31] M. Kreysing, Probing the functional role of physical motion in development, Dev. Cell **51**, 135 (2019).

[32] N. T. Chartier, A. Mukherjee, J. Pfanzelter, S. Fürthauer, B. T. Larson, A. W. Fritsch, R. Amini, M. Kreysing, F. Jülicher, and S. W. Grill, A hydraulic instability drives the cell death decision in the nematode germline, Nat. Phys. **17**, 920 (2021).

[33] M. Mittasch, V. M. Tran, M. U. Rios, A. W. Fritsch, S. J. Enos, B. Ferreira Gomes, A. Bond, M. Kreysing, and J. B. Woodruff, Regulated changes in material properties underlie centrosome disassembly during mitotic exit, J. Cell Biol. **219** (2020).

[34] E. Erben, B. Seelbinder, I. D. Stoev, S. Klykov, N. Maghelli, and M. Kreysing, Feedback-based positioning and diffusion suppression of particles via optical control of thermoviscous flows, Opt. Express **29**, 30272 (2021).

[35] I. D. Stoev, B. Seelbinder, E. Erben, N. Maghelli, and M. Kreysing, Highly sensitive force measurements in an optically generated, harmonic hydrodynamic trap, eLight **1**, 7 (2021).

[36] E. Yariv and H. Brenner, Flow animation by unsteady temperature fields, Phys. Fluids **16**, L95 (2004).

[37] Y. Hayashi, Fluid-dynamical study of protoplasmic streaming in a plant cell, J. Theor. Biol. **85**, 451 (1980).

[38] I. G. Donaldson, The estimation of the motive force for protoplasmic streaming in *Nitella*, Protoplasma **74**, 329 (1972).

[39] J. Rumble, *CRC Handbook of Chemistry and Physics* (CRC Press, Boca Raton, FL, 2017).

[40] J. Happel and H. Brenner, *Low Reynolds Number Hydrodynamics* (Prentice Hall, Englewood Cliffs, NJ, 1965).

[41] W. M. Slie, A. R. Donfor Jr., and T. A. Litovitz, Ultrasonic shear and longitudinal measurements in aqueous glycerol, J. Chem. Phys. **44**, 3712 (1966).

[42] L. G. Leal, *Advanced Transport Phenomena: Fluid Mechanics and Convective Transport Processes* (Cambridge University Press, Cambridge, UK, 2007).

[43] J. Simpson, Gravity currents in the laboratory, atmosphere, and ocean, Annu. Rev. Fluid Mech. **14**, 213 (1982).

[44] C. B. Mast, S. Schink, U. Gerland, and D. Braun, Escalation of polymerization in a thermal gradient, Proc. Natl. Acad. Sci. USA **110**, 8030 (2013).

[45] N. Osterman and D. Braun, Thermooptical molecule sieve on the microscale, Appl. Phys. Lett. **106**, 073508 (2015).

[46] M. Morasch, D. Braun, and C. B. Mast, Heat-flow-driven oligonucleotide gelation separates single-base differences, Angew. Chem. Int. Ed. **128**, 6788 (2016).

[47] A. R. Bausch, W. Möller, and E. Sackmann, Measurement of local viscoelasticity and forces in living cells by magnetic tweezers, Biophys. J. **76**, 573 (1999).